

LOAN COPY: R  
AFWL TECHNII  
WIRTZLAND AFB  
0067743



# Water-Tunnel and Analytical Investigation of the Effect of Strake Design Variables on Strake Vortex Breakdown Characteristics

Neal T. Frink and John E. Lamar

AUGUST 1980

NASA



0067743

NASA Technical Paper 1676

# Water-Tunnel and Analytical Investigation of the Effect of Strake Design Variables on Strake Vortex Breakdown Characteristics

Neal T. Frink and John E. Lamar  
*Langley Research Center*  
*Hampton, Virginia*



National Aeronautics  
and Space Administration

**Scientific and Technical  
Information Branch**

1980

## SUMMARY

A systematic water tunnel study was made to determine the vortex breakdown characteristics of 43 strakes, more than half of which were generated from a new analytical strake design method. The strakes were mounted on a 1/2-scale model of a Langley Research Center general research fighter fuselage model with a  $44^{\circ}$  leading-edge-sweep trapezoidal wing.

This study develops, in conjunction with a common wing-body, a parametric set of strake data for use in establishing and verifying a new strake design procedure. To develop this parametric data base, several series of isolated strakes were designed on the basis of a simplified approach which relates prescribed suction and pressure distributions in a simplified flow field to planform shapes.

The resulting planform shapes provided examples of the effects of the primary design parameters of size, span, and slenderness on the vortex breakdown characteristics. These effects are analyzed in relation to the respective strake leading-edge suction distributions. Included are examples of the effects of detailed strake planform shaping for strakes with the same general size and slenderness. It was concluded that, consistent with the design criterion, those with leading-edge suction distributions which increase more rapidly near, and have a higher value at, the spanwise tip of the strake produce a more stable vortex.

## INTRODUCTION

During the development of the F-16 (fig. 1) and F/A-18 lightweight fighters, certain strake-wing combinations were found to be of interest because of the following features: (1) the ability to generate large amounts of lift during transonic-maneuver conditions, and (2) the achievement of this benefit with low gust response, relatively low structural weight, and negligible impact on cruise aerodynamics. The first feature results from the benefit of separation-induced vortex flow on the strake as well as the development of a favorable interference effect on the wing through the interaction of the strake vortex with the wing flow field. The second group of features is associated with the low aspect ratio and relatively small size of the strake. The need for a strake or other flow controlling device on wings in the sweep range of these aircraft is well known (ref. 1) and is illustrated by a typical separated flow field over a wing-body at an angle of attack of  $20^{\circ}$ , which is shown in figure 2.

While these lightweight fighters were being developed, few, if any, theoretical or empirical procedures were available to assist in designing strakes that provided both high maneuver lift potential and satisfactory stability

characteristics. This situation is illustrated by the fact that over 100 strake configurations were wind-tunnel tested by each company before final selections were made.

One of the limitations encountered in strake performance during maneuver is associated with vortex breakdown. Recently, a simple analytical method has been developed which appears to offer some guidance for this aspect of the design problem. A description of this method and an initial application to strake design is reported in reference 2; for completeness, the development of the method is repeated in appendix A. To more completely evaluate this method, an extensive design and evaluation study was undertaken and is reported in this paper.

There are other conditions associated with aircraft stability and asymmetric flow which can have profound effects on the capability of an aircraft to completely utilize the generated strake maneuver lift. The present study, however, is limited to symmetric flow and uncambered lifting surfaces.

To keep the project manageable, a simple economical way was sought to select a limited series of strakes from a large number of possible designs for further detailed wind-tunnel studies. This series was selected on the assumption that those strakes which attained high angles of attack before vortex breakdown at the wing trailing edge would offer good performance in the wind tunnel. The most convenient way appeared to be the use of a water tunnel to study the change in vortex breakdown patterns with angle of attack for both strakes and wings.

A large systematic series of strakes was designed by the method of reference 2 to provide both stable and unstable vortex systems through use of a wide range of overall geometric considerations. Because of their mutual interest, the Northrop Corporation/Aircraft Division agreed to support these tests by building a 1/2-scale model of a general research fighter wing-body, building 43 of the designed strakes, and providing the water-tunnel facility and operating personnel to assist the authors during the test.

Use of trade names or names of manufacturers in this report does not constitute an official endorsement of such products or manufacturers, either expressed or implied, by the National Aeronautics and Space Administration.

This paper reviews the design procedure of reference 2 and presents the results of the water tunnel studies.

#### SYMBOLS AND ABBREVIATIONS

Dimensional quantities are given in both SI Units and U.S. Customary Units. Measurements and calculations were made in U.S. Customary Units.

AD analytically designed

a<sub>1</sub> constant

$\bar{a}$	constant, $a_1/c_1^2$
BD	breakdown
b	span, cm (in.)
$b_1$	constant
$\bar{b}$	constant, $b_1/c_1^2$
C	constant $\Delta C_p$ specification
$C_L$	lift coefficient, $\text{Lift}/q_\infty S_{\text{ref}}$
$C_p$	local pressure coefficient
$\Delta C_p(\theta, \eta)$	lifting pressure coefficient at $\theta, \eta$
$C_0$	constant
$C_1$	constant
$C_S$	total leading-edge suction coefficient, $\frac{\text{Suction}}{q_\infty S_{\text{ref}}}$
$C_T$	total leading-edge thrust coefficient, $\frac{\text{Leading-edge thrust}}{q_\infty S_{\text{ref}}}$
$C_Y$	twice total side-edge suction-force coefficient of one wing panel, $\frac{2(\text{Side force along side edge on one wing panel})}{q_\infty S_{\text{ref}}}$
c	local chord, cm (in.)
$\bar{c}$	mean aerodynamic chord, 11.66 cm (4.59 in.)
$c_r$	root chord along side of fuselage, cm (in.)
$c_{sc}$	= Local suction force/ $q_\infty$ , cm (in.)
$c_t$	tip chord of strake, cm (in.)
$c_y(b/2)_{sl}$	= $\frac{\text{Local side force}}{q_\infty}$ , cm (in.)
ED	empirically designed
e	distance along strake contour, cm (in.)
$e_c$	total contour length of strake, cm (in.)
$F_Y$	side-edge force, N (lb)

g	ratio of change in strake area to change in $\Delta\alpha_{BD-TE}$
h	ratio of change in $K_v$ to change in $\Delta\alpha_{BD-TE}$
$K_v$	leading-edge vortex lift factor
LE	leading edge
$\ell$	exposed longitudinal length of strake, cm (in.)
M	Mach number
N	number of chordwise control points
P	polynomial or 3-D $\Delta C_p$ specification
$q_o(\eta)$	coefficient of $\cot(\theta/2)$ lifting pressure function, N/m (lb/ft)
$q_j(\eta)$	coefficient of $\sin(j\theta)$ lifting pressure function, where $j = 1$ to $N - 1$ , N/m (lb/ft)
$q_\infty$	free-stream dynamic pressure, N/m <sup>2</sup> (lb/ft <sup>2</sup> )
$R_a$	ratio of exposed strake area to wing reference area, $S_s/S_{ref}$
$R_b$	exposed semispan ratio, $[(b/2)_s/(b/2)_w]_{exp}$
$R_c$	$=(c_r)_w/(c_r)_w$
R.F.	related flow
$R_s$	slenderness ratio of exposed strake, $\ell/(b/2)_{exp}$
r	radius of curvature, cm (in.)
S	leading-edge suction force, N (lb)
$S_{ref}$	wing reference area, m <sup>2</sup> (in <sup>2</sup> )
$S_s$	exposed strake area, m <sup>2</sup> (in <sup>2</sup> )
s	$= \frac{c_s c}{\alpha^2 (b/2)_s}$
$\bar{s}$	$= \frac{d(c_s/2)}{de} \frac{S_{ref}}{\alpha^2 (b/2)_s}$
T	leading-edge thrust force, N (lb)
U	free-stream velocity, m/sec (ft/sec)

VLM                    vortex lattice method  
 x                    longitudinal distance from wing trailing-edge root chord to vortex breakdown, cm (in.)  
 x'                    distance aft of local leading edge, cm (in.)  
 x/(c<sub>r</sub>)<sub>w</sub>    nondimensionalized chordwise vortex breakdown position  
 α                    angle of attack, deg  
 β                    =  $\sqrt{1 - M^2}$   
 η                    spanwise coordinate of strake in fraction of exposed strake semispan  
 η\*                    η value where s versus η changes slope (see table II)  
 θ                     $\arccos(1 - 2(x'/c))$ , 0 at local leading edge; π at local trailing edge  
 Λ<sub>ℓ</sub>(η), Λ<sub>ℓ</sub>(y)    leading-edge sweep angle functions, deg  
 Λ<sub>t</sub>                    constant trailing-edge sweep angle, deg  
 3-D                    three-dimensional

Subscripts:

BD                    breakdown  
 exp                    exposed  
 l                    lower surface  
 max                    maximum  
 s                    strake  
 sl                    local strake  
 t                    value at the leading-edge tip  
 TE                    trailing edge  
 u                    upper surface  
 w                    wing  
 ws                    wing-strake

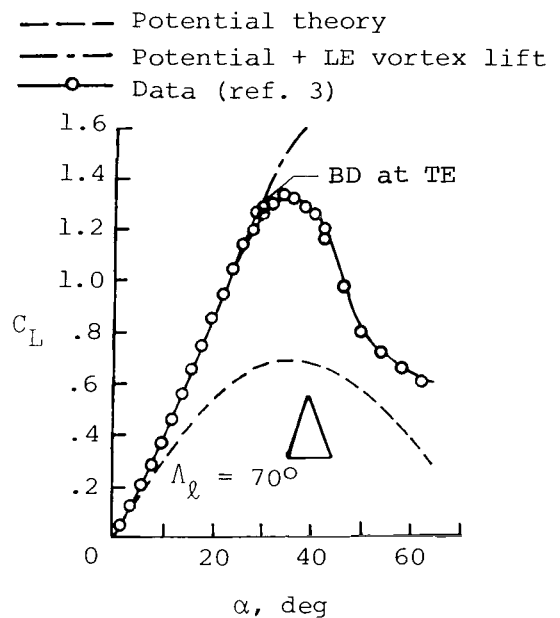
## DISCUSSION OF STRAKE DESIGN PROCEDURE

### General Considerations

Slender lifting surfaces have reasonably good vortex flow characteristics and reach large angles of attack and lift coefficients before breakdown occurs ahead of the trailing edge, as demonstrated by the highly swept delta wing (ref. 3). However, there is considerable evidence to suggest that for a given slenderness ratio  $R_s = l/(b/2)_{exp}$ , detailed shaping of the planform can provide additional angle-of-attack capability. It is the purpose of this section of the paper to outline the present approach to this design problem.

The onset of vortex breakdown ahead of the trailing edge has been found to be directly related to the angle of attack at which  $C_{L,max}$  is developed for many wings. As shown in sketch (a) for a  $70^\circ$  delta wing, vortex breakdown generally occurs in the vicinity of the trailing edge at angles of attack where the lift coefficients begin to depart from the vortex lift theory. This correlation is further documented in reference 3 for other slender delta wings having  $\Lambda_l > 70^\circ$ .

It is recognized, of course, that "isolated" strake characteristics do not necessarily define the relative effectiveness of a strake-wing combination. Nevertheless, in order to make this initial design study more amenable to a theoretical approach, only isolated strakes were considered. It was assumed that if the vortex breakdown could be delayed on the isolated strake, then it might also be delayed for the strake-wing combination. Therefore, once a series of strakes has been designed and tested in combination with a wing, the experimental data can be analyzed with the aid of a strake-wing analysis theory, such as the VLM code (refs. 4 and 5), to provide additional information which may be used for further refinement of the design process.



Sketch (a)

### Strake Design Criterion

This section describes one criterion used in an attempt to design better strake shapes. The criterion is based on an observation that those delta wings which develop leading-edge suction distributions in three-dimensional attached flow, which are more triangular, and which reach a higher peak near the tip, tend to maintain vortex stability to higher angles of attack.

Reference 6 first cited these characteristics, and sketch (b) shows the effect of increasing sweep on both suction peak and  $\alpha_{BD-TE}$ . Similar effects were noted for cropped planforms in reference 7.

The manner in which the criterion is to be used in determining these better strake shapes follows.

#### Description of Method

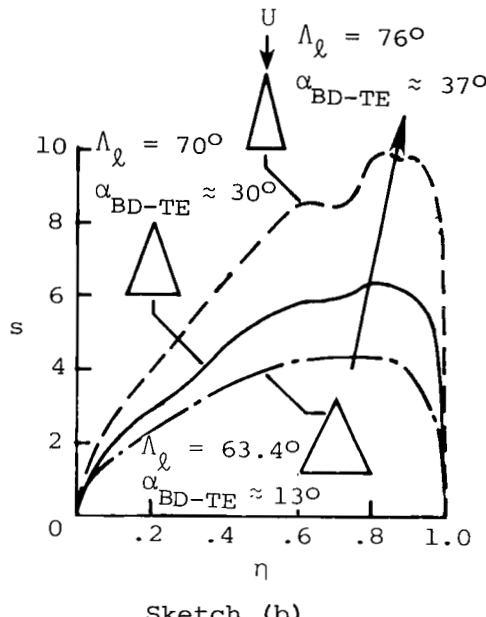
##### Other Assumptions

If it is assumed that the preceding observations with regard to the possible relationships between the attached flow leading-edge suction distribution and vortex stability are valid and can be extended to strake-wing combinations, then it may be possible to use the breakdown criterion in a strake design method. The primary purpose of this study is to develop, in conjunction with a common wing-body, a parametric set of strake data which would be useful in establishing and verifying a design procedure based on the suction distribution concept. To develop this parametric data base, several series of isolated strakes were designed on the basis of a simplified approach which provided an analytical method of defining planform shapes. This method (developed in ref. 2 and described in appendix A) relates planform shapes to prescribed suction distributions in a simplified flow field that is related to three-dimensional (3-D) flow through certain assumptions listed in figure 3 and is called related flow (R.F.).

##### Variables

A FORTRAN coded version of the design method is used to generate strake planform geometries by solving an initial value problem, where the local leading-edge sweep angles are determined iteratively from equation (A2). Iterations are made over the entire span until a root chord is determined which satisfies the tip chord specified value. (It was determined later that the solution could be made from the tip inboard with no iteration.) The designer must prescribe a leading-edge suction distribution; a spanwise  $\Delta C_p$  distribution, which in essence specifies the kind of flow; a semispan  $\frac{b}{2}$ , a tip chord  $c_t$ ; a trailing-edge sweep angle  $\Lambda_t$ ; and a subcritical Mach number  $M$ .

The design code can be executed using either a constant or a polynomial spanwise  $\Delta C_p$  distribution description, as discussed in a subsequent section. Each is specified to occur at either a constant  $x'/c$  or a constant  $\Delta x'$  from the leading edge. (The examples employed in this study use only a constant  $x'/c$  specification.) The leading-edge suction distribution can be



Sketch (b)

defined either by two linear segments or by a more generalized three-dimensional distribution.

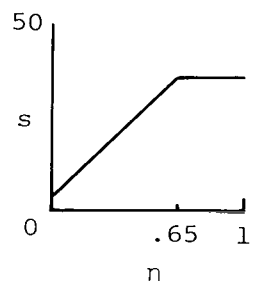
For this investigation the prescribed suction distributions were carefully selected to yield an appropriate range of three-dimensional flow possibilities. Although the method used does not accurately establish the actual three-dimensional suction distribution, it does provide a convenient method of establishing strake shapes which form a parametric data base that is related, within the assumptions made, to the generating suction distributions. Comparisons are also made with the prescribed and three-dimensional suction distributions to check the validity of this method.

It is interesting to note, as shown in figure 4, how the prescribed  $s-\eta$  distribution in the related flow is reasonably well reproduced by  $s-\eta$  for the strake-wing-body configuration in three-dimensional flow over the inboard region of the strake. Outboard on the strake, the wing upwash due to the strake-wing juncture leads to suction levels which exceed the prescribed level. However, the preceding discussion does tend to substantiate one of the assumptions employed in this method.

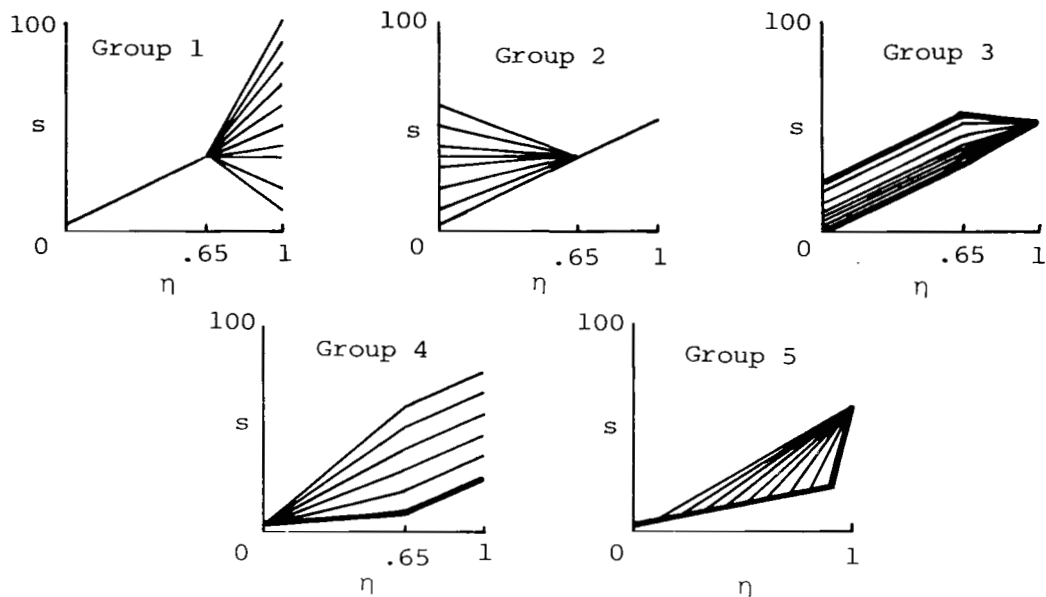
Prescribed  $s-\eta$  distribution.— As previously described, the prescribed suction distribution has an effect on the resulting strake shape. For example, in reference 2 the  $s-\eta$  distribution for the  $76^\circ$  delta wing in a three-dimensional flow, when used in the design procedure based on related flow, leads to a gothic shape (shown in fig. 4). This difference in shape is not surprising when the consequences of the flow and loading assumptions are considered (i.e., three dimensional as opposed to a constant  $\Delta C_p$  distribution). Wind-tunnel tests of the gothic strake in combination with a wing-body showed it to reach a high angle of attack before vortex breakdown occurred.

The successful test, however, raised a question concerning this strake and the strake design criterion: Was the stable condition of the strake vortex up to high angles of attack due to the particular suction distribution chosen, and if so, was it the high inboard slope or the high tip suction peak that was more beneficial? The answer to this question is but one of several which are interrelated, tied up in the strake geometry, and addressed herein. In this study, the original suction distribution (sketch (c)) was perturbed to gain an understanding of which spanwise region, inboard or outboard, is more important. In addition, other  $s-\eta$  variations were prescribed including some that tended to violate the criterion set forth. In all, some 13 groups of suction distributions were prescribed and are shown in the sketches (d) to (f). Each sketch is followed by a brief description of the salient features of the group portrayed. (The heavy lines indicate selected strake design distributions.)

In sketch (d), the outboard part of the prescribed group 1 suction distribution is varied while the inboard part remains fixed. In group 2, the inboard part is varied while



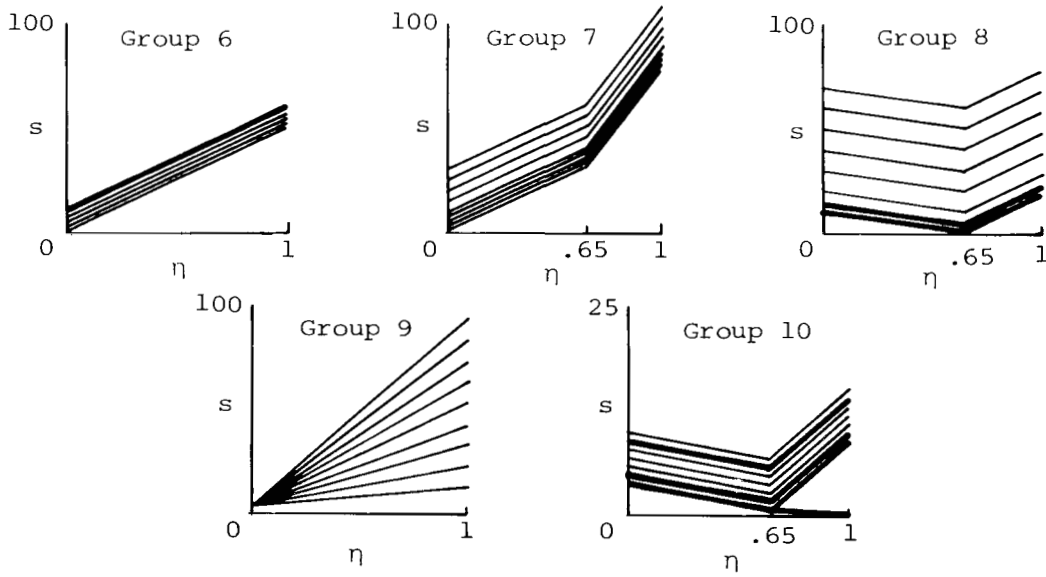
Sketch (c)



Sketch (d)

the outboard part is held fixed. In group 3, the inner part is translated vertically, and the outer slope is varied to keep the suction continuous. In group 4, the outer part is translated vertically, and the inner slope is varied to keep the suction distribution continuous. In group 5, the segment break-point is varied while holding the two extremal values and the slope of the initial distribution constant.

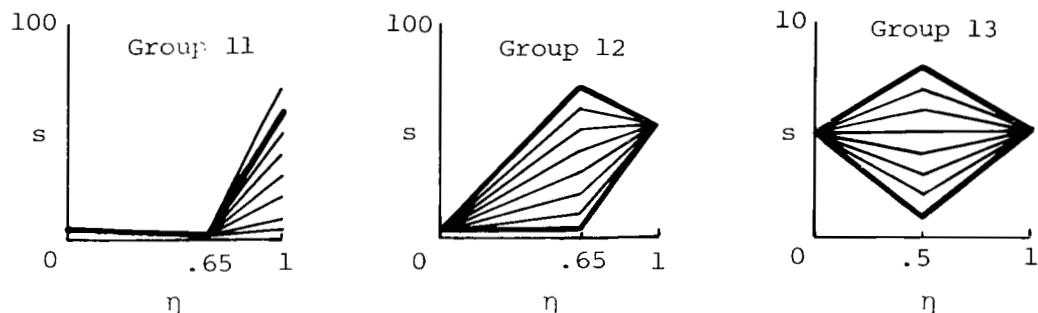
Groups 6, 7, and 8 use simple vertical translations from an initial distribution, as illustrated in sketch (e). In group 6, a single segmented curve



Sketch (e)

is employed with positive slope. In group 7, a two-segmented curve is used with both parts having a positive slope. In group 8, a two-segmented curve is utilized with the inboard and outboard parts having negative and positive slopes, respectively. In group 9, the slope of a single segment curve is varied while holding the inboard extremal value constant. Group 10 is similar to group 8, but the magnitudes of the slopes are decreased. As a limiting case, the lowest curve in group 10 is allowed to reach zero at the tip  $\eta = 1$ .

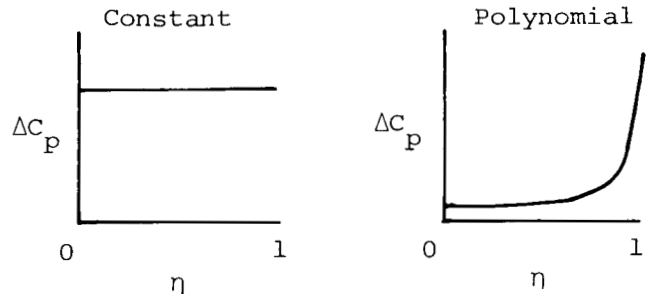
Sketch (f) shows the remaining suction groups that were considered. In group 11, the outboard part is varied while fixing the inboard part with a negative slope. In group 12, the two extremal values are held constant, the outer being larger than the inner, while the path between the two points is varied. In group 13, the two extremal values are held equal at a constant value while the path of the curves between them is varied.



Sketch (f)

$\Delta C_p$  specification.— The chordwise  $\Delta C_p$  distribution is assumed to behave in a  $\cot(\theta/2)$  manner aft of the local leading edge. This assumption leaves only the spanwise variation for treatment. In reference 2,  $\Delta C_p$  is specified to be constant along constant values of  $x'/c$  near the leading edge. Even for the first application made using this variation of  $\Delta C_p$ , it was noted (ref. 2) that other  $\Delta C_p$  forms near the leading edge could be used (sketch (g)); a three-dimensional or polynomial form was specifically noted. The idea was that if a more representative  $\Delta C_p$  variation was used, then the resulting strake shape would have more of the three-dimensional flow features in its solution and perhaps be a better strake. The first attempt to verify this idea employed the three-dimensional  $\Delta C_p$  distribution for a  $76^\circ$  delta wing near the leading edge which had the form

$$\Delta C_p = 0.20817 \left( 1 + \frac{1}{1.01 - \eta} \right)$$



Sketch (g)

and its corresponding  $s-\eta$  distribution. This  $\Delta C_p$  form is called polynomial herein. Both the  $s-\eta$  and  $\Delta C_p$  distributions were obtained from the VLM (refs. 4 and 5). The resulting shape was close to that of the  $76^\circ$  delta wing used as input to the VLM (sketch (h)) and served to validate the idea.

Both the constant and polynomial pressure distributions were used to generate the strake shapes which are discussed in a subsequent section of the paper.

### Characteristics of the Solution

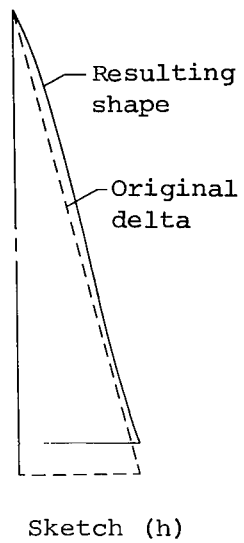
It would be advantageous to know why certain strake shapes are generated by the design procedure for certain  $s-\eta$  and  $\Delta C_p$  distributions. In particular, the designer should have some feeling for the type of strake shape to expect from the procedure for those  $s-\eta$  distributions which meet the design criterion stated in a previous section. Therefore, an analytical study of the basic strake design equation was performed to provide some understanding of the nature of the solution. Reference 8 presents an analytical solution to the design equation for which a constant  $\Delta C_p$  distribution is assumed. Also included is an order-of-magnitude analysis of the solution which is useful in isolating the dominant terms.

The order-of-magnitude analysis reveals that the leading-edge sweep angle tends to increase logarithmically in the spanwise direction for those  $s-\eta$  distributions which meet the design criterion. Therefore, in terms of the preceding specifications, the designer can anticipate a gothic-shaped strake to result from the design procedure.

## STRAKE SHAPES STUDIED

### Basis for Selection

From the method just described, over 200 strake shapes were analytically designed (AD), and 24 of these were of sufficient interest or were unique enough to warrant testing. Of the 24 studied, 12 (AD 1 to AD 12) had reflexive leading edges, and 12 (AD 13 to AD 24) were gothic (shown in figs. 5(a) and 5(b)). The ones selected for study were those which could help the designer answer questions relative to (1) the importance of the initial leading-edge sweep angle (values of  $46.2^\circ$  to  $83.8^\circ$  were chosen), (2) the effect of slenderness ratio  $R_s$  (values from 3.0 to 10.7 were selected), (3) the ratio of exposed strake area to wing reference area  $R_a$ , and (4) the versatility and usability of the design code. Furthermore, 18 empirically designed strakes (ED), variations of the basic AD 24 strake, were tested (shown in fig. 5(c)). These strakes were studied to answer questions related to obtaining levels of performance comparable with those of the large analytically designed strakes, but with a smaller chord. Some of the chord alterations were obtained by



Sketch (h)

scaling (ED 12 and ED 13) and some by adding trailing-edge area (ED 16 to ED 18); others were obtained by cutting along the inboard edge (ED 9 to ED 11), the apex region (ED 1 to ED 4), and the trailing-edge region (ED 5 to ED 8). Snags (ED 14 and ED 15) were even added to the smallest scaled strake (ED 13) to change its chord variation and perhaps its effectiveness. In this paper, the prescribed strake designations refer to their respective strake-wing configurations.

#### Analytically Designed Strakes (AD Series)

Pertinent geometric properties for the analytically designed strakes previously mentioned are listed in table I; the input design parameters are given in table II.

The original gothic strake of reference 2 is designated the AD 24. Strakes AD 22 and AD 23 (shown in fig. 5(b)) are scaled down from the AD 24 to have the same value of  $R_a$  as Strake I and Strake II of reference 9, respectively. The remaining strakes were designed to have the same semispan as the midsized AD 23 strake with the exception of the AD 9 strake, which was designed to have a smaller semispan because of its excessive length.

#### Empirically Designed Strakes (ED Series)

Additional details of the aforementioned empirically designed strakes are given in the following subsections. Table III is used to summarize their pertinent geometric properties.

##### Apex Cuts

Strakes ED 1 to ED 4 (shown in fig. 5(c)) are formed by cutting the AD 24 in the chordwise direction at regular intervals from the apex. The  $60^\circ$  initial sweep corresponds to  $\Lambda_\ell(\eta=0)$  of the AD 24. Strakes ED 2 and ED 4 have the same values of  $R_s$  as the ED 12 and ED 13, respectively.

##### Trailing-Edge Cuts

Strakes ED 5 to ED 8 (shown in fig. 5(c)) are formed by cutting the AD 24 parallel to, and at regular intervals from, the trailing edge. Strake ED 6 has approximately the same value of  $R_s$  as the ED 12.

##### Spanwise Cuts

Strakes ED 9 and ED 11 (shown in fig. 5(c)) are formed by cutting the AD 24 parallel to the inboard edge. Cuts were made at 15 percent, 30 percent, and 45 percent of the original semispan, respectively, from the inboard edge.

### Chordwise Scaling

Strakes ED 12 and ED 13 (shown in fig. 5(c)) were derived by scaling the AD 24 strake 70 percent and 30 percent, respectively, in the chordwise direction while holding the semispan constant. Strake ED 12 has the same slenderness ratio as Strake III of reference 9, which is shown in figure 6. Strake ED 13 is an extreme case of small slenderness and provides an additional data point for the dependency of vortex breakdown on chordwise scaling.

### Snagged Strakes

It was anticipated that the ED 13 would exhibit poor vortex breakdown characteristics. In an attempt to improve the performance of a strake with small slenderness ratio, a snag was added to the ED 13. The snag was produced by altering the chord distribution over the inboard and outboard regions of the strake. Over the inboard region, the chord was reduced linearly from the root to the snag location. Over the outboard region, the chord was increased linearly from the tip to the snag location.

The idea was to use the snag to increase the local leading-edge sweep across the span and thereby enable the strake to generate a stronger vortex. However, it was anticipated that the counterrotating snag side-edge vortex could impede the improved strake vortex and be detrimental to the overall performance gains.

Two snagged strakes (shown in fig. 5(c)) were tested. The snag on strake ED 14 has a spanwise position of 1/3 semispan and a length of 1/8 semispan. The snag on strake ED 15 has a spanwise position of 2/3 semispan and a length of 1/4 semispan.

### Side-Edge Extension

In another attempt to improve the ED 13 performance, a side-edge extension approximately the length of the strake was added, and this strake was designated the ED 16. The side edge was progressively shortened, and the resulting series of strakes (shown in fig. 5(c)) are identified as ED 17 and ED 18.

### Strake III

Strake III of reference 9 (shown in fig. 6) was selected for water-tunnel testing to provide additional data on the influence of geometric parameters, such as area, slenderness ratio, and shape, on the vortex breakdown phenomenon. For example, strakes ED 12, ED 2, and ED 6 were designed to have the same slenderness ratio as Strake III so that comparisons could be made for different strake shapes having the same value of  $R_s$ .

## BASIC WING-BODY DESCRIPTION

The basic wing-body used was approximately a 1/2-scale model of the general research fighter model tested extensively in the Langley High-Speed 7-By 10-Foot Tunnel. A drawing of the water-tunnel configuration along with pertinent dimensions is given in figure 7. The  $44^{\circ}$  swept wing has a reference aspect ratio, a taper ratio, and an area of 2.5, 0.2, and  $0.0258 \text{ m}^2$  ( $40 \text{ in}^2$ ), respectively. All the preceding features are based on the reference wing, which includes the area between the leading and trailing edges projected to the model center line. The wing was tested in both fore and aft positions depending on the length of the strake.

## TEST FACILITY AND PROCEDURE

The test facility used was the Northrop 16- by 24-inch Diagnostic Water Tunnel (shown in fig. 8). It features a closed return with both horizontal and downward-flow vertical test sections; the vertical test section was used in this study. Figure 8 shows a model mounted in this position. The test conditions were a velocity of approximately  $0.15 \text{ m/sec}$  ( $0.50 \text{ ft/sec}$ ), a Reynolds number, based on  $\bar{c}$ , of approximately  $1.76 \times 10^4$ , and angle-of-attack variations from  $0^{\circ}$  to  $50^{\circ}$ . Reference 1 has shown that for sharp-edge delta wings, the Reynolds number effects were not significant for values up to  $1 \times 10^6$ , and therefore, the results reported in the present study should also be applicable up to this Reynolds number. Sideslip could also be varied but was set to zero for these results.

The test procedure was to align the model so that at both high and low angles of attack it produced symmetrical strake vortex breakdown. Breakdown was determined by noting the behavior of the dye injected into the strake vortex core. When the dye trumpeted or exhibited reversal of direction, breakdown was said to have occurred. After symmetry was established,  $\alpha$  was increased from  $10^{\circ}$  in  $2^{\circ}$  increments until breakdown occurred near the trailing edge; thereafter, it was increased in  $1^{\circ}$  increments. After strake vortex breakdown occurred ahead of the wing trailing edge, the increment in  $\alpha$  was increased to  $2^{\circ}$ . At each  $5^{\circ}$  increment after  $10^{\circ}$ , photographs were taken in both plan view and side view (with one exception) to record the vortex patterns. With the help of scribed lines on the wing and strake surfaces, estimates were made of vortex breakdown position. The results of the photography and breakdown estimation are given in the next section.

## RESULTS AND ANALYSIS

### General Comments

It must be kept in mind that the following analysis deals only with the vortex breakdown characteristics, whereas the actual aerodynamic performance can be determined only after wind-tunnel force tests have been performed. In figures 9 to 23, both the strake vortex breakdown data for each configuration and sample top and side view photographs at  $\alpha = 20^{\circ}$  are presented. The

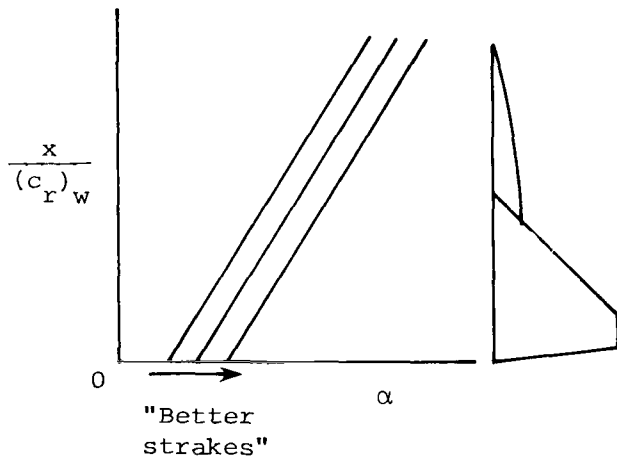
results are organized according to (1) the various  $s-\eta$  groups (figs. 9 to 16) and (2) those obtained through empirical variations of the original gothic strake of reference 2 (figs. 17 to 22). Table II lists the strake designations for the analytically designed shapes with their respective data figure numbers and a description of the corresponding prescribed suction distributions.

#### Data Format and Performance Assessment

The breakdown plots illustrate the progression of the nondimensional, chordwise strake vortex breakdown location  $x/(c_r)_w$  with angle of attack  $\alpha$ . Since the wing is the main lifting surface, the interaction of the strake vortex flow field with the wing pressure field is of primary interest. Therefore, the chordwise vortex breakdown position  $x$  is nondimensionalized by  $(c_r)_w$  to make the results directly comparable over the wing. Vortex breakdown over the strake is not directly comparable between configurations, but its absolute location can be observed in relation to the generating strake shape shown at the right of the (b) part of figures 9 to 23. The line codes used to define the strake shapes in the planform sketches are the same as those used to connect the corresponding data points.

The corresponding photographs on the facing pages, the (a) part of figures 9 to 23, reveal the influence of the wing pressure field on the path of the vortex. The strake vortex core is visible as a long heavy line emanating from the strake apex. The wing vortices are generally visible outboard of the strake vortices. In several of the top view photographs, the wing vortices have been enhanced by a grease pencil to increase their visibility. Efforts to photograph the top view of the model perpendicularly were not always successful.

Judgment of strake performance is based on (1) the angle of attack at which the strake vortex breakdown crosses the wing trailing edge  $\alpha_{BD-TE}$ , (2) the rate at which the breakdown progresses forward over the wing once breakdown has occurred, and/or (3) the efficiency of the strake area. As shown in sketch (i), "Better strakes" are those which have the higher values of  $\alpha_{BD-TE}$ . This feature is important because the occurrence of vortex breakdown over the wing is realized as a subsequent loss in lift. Sketch (j) illustrates that once vortex breakdown crosses the wing trailing edge, a low rate of forward breakdown progression with increasing  $\alpha$  is preferable. This low rate is desirable because a more gradual loss in wing lift



Sketch (i)

promotes milder stall characteristics. Sketch (k) illustrates that if the design approach proposed can produce reductions in strake area while maintaining the same angle of attack for vortex breakdown, then a more efficient strake would result.

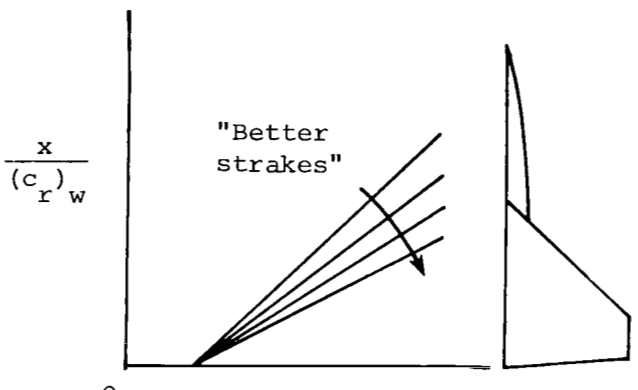
#### Effect of Major Parameters

Although the strake design problem is one of many variables, the major geometric parameters are area, slenderness, semispan, and planform shaping. The effects of these variables as well as their relationships to one another are illustrated in the following sections.

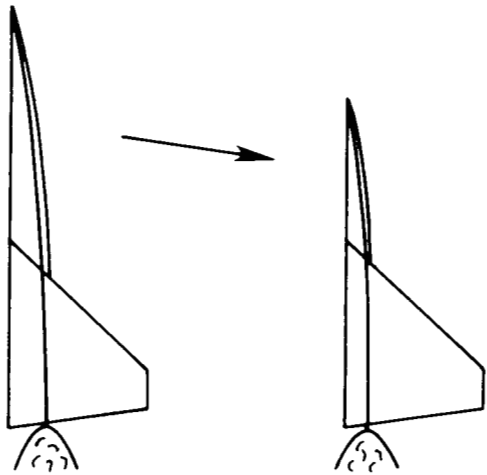
#### Area/Semispan

As pointed out previously, the design process used to develop the generic families of strakes considered only the isolated strake. However, when these strakes are combined with the wing, the ability of the strake vortex to penetrate the wing flow field is, of course, a strong function of the size of the strake relative to the wing.

Figure 24 presents the measured angle of attack corresponding to vortex breakdown at the wing trailing edge  $\alpha_{BD-TE}$  as a function of the ratio of exposed strake area to wing reference area  $R_a$  for many gothic and reflexive strake-wing combinations. Three values of gothic-strake semispan are represented in figure 24(a) and are identified by the shaded bands for two sets and by the single point, AD 22, for the third. The effect of area on  $\alpha_{BD-TE}$  is seen to be an expected one of increasing  $\alpha_{BD-TE}$  with increasing  $R_a$ . This figure establishes a further relationship for strakes of different semispan. In particular, the data for strakes with  $R_b = 0.212$  lie within a band which is above and has a higher slope than a similar band bounding the data for strakes with  $R_b = 0.297$ . As the two bands indicate the effect of increasing  $R_b$  at a fixed value of  $R_a$  is to reduce  $\alpha_{BD-TE}$ . This can be better understood when it is put in terms of the change in slenderness ratio; i.e., increasing  $R_b$  for fixed  $R_a$  generally results in a less



Sketch (j)



Sketch (k)

slender strake. This earlier vortex breakdown associated with reduced slenderness is not surprising since such a trend has been well established for isolated planforms by previous researchers (ref. 3).

Figure 24(b) shows the  $\alpha_{BD-TE}$  versus  $R_a$  data for the reflexive strakes at  $R_b = 0.212$ . Just as noted for the gothic strakes, the reflexive strakes show the powerful effect of area and the expected trend of increasing  $\alpha_{BD-TE}$  with  $R_a$ . The data tend to fall in a band and are therefore presented in that manner.

The general trend of  $\alpha_{BD-TE}$  due to area and slenderness changes has been illustrated in figure 24; detailed results of breakdown progression are presented in the next three sections. The first deals with area scaling, the second with slenderness variations, and the third with leading-edge shaping.

#### Area/Leading-Edge Shaping

Figures 16, 25, and 26 are used to examine the relationship between area and leading-edge shaping by assessing their impact on  $\alpha_{BD-TE}$  for a fixed shape, a variable shape, and a shape with  $R_s$  kept at a constant value.

Shape fixed.— Figure 16 presents the vortex breakdown characteristics as well as the prescribed and three-dimensional suction distributions for the AD 24, AD 23, and AD 22 strakes, which are of fixed shape but scaled in size. Regarding breakdown, the vortex for a smaller strake must persist over a greater relative distance to the wing trailing edge and must penetrate through a stronger adverse wing pressure gradient relative to its vortex strength than that for a larger strake. Hence, it is anticipated that  $\alpha_{BD-TE}$  will decrease as a strake is scaled down in area; this is confirmed by the data.

Another interesting characteristic of these scaled strakes is the manner in which the breakdown data cross  $x/(c_r)_w = 1$  at  $\alpha = 32^\circ$ . This characteristic is related to the identical but scaled shaping of the strake. It is expected that each of these strakes would have the same vortex breakdown characteristics if tested alone (without a wing-body). Hence, even in the presence of a wing-body, the strakes behave somewhat as they would when tested alone, with the differences in breakdown progression being more related to the differences in ratio of strake chord to wing chord. This feature is further evidenced by noting that at  $\alpha = 40^\circ$ , the vortex breakdowns occur at approximately  $\frac{1}{3}(c_r)_s$  from the apex of each respective strake.

The leading-edge suction distributions  $s-\eta$  for the strakes in the two assumed flow fields are shown by the insert in figure 16(b). The two-segmented trapezoidal curve is the prescribed distribution from which the strake was designed, whereas the other curve is the three-dimensional potential flow distribution determined by applying an analysis method to the designed strake in the presence of the wing and body. An extended version of the VLM of

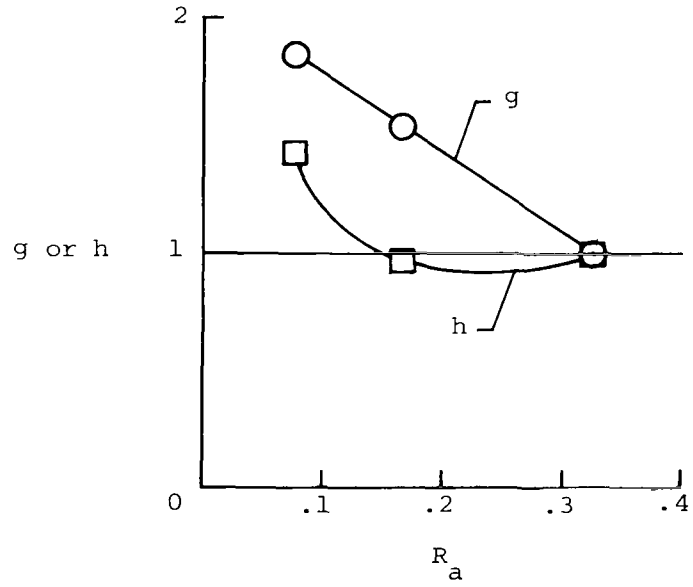
reference 5<sup>1</sup> was used to calculate the better distributions for the complete configurations. These are more representative of the actual distributions developed on the strakes and are used as an aid in the analysis.

These three sets of curves show that in addition to  $\alpha_{BD-TE}$  decreasing with  $R_a$ , the leading-edge suction values at the tip  $s_t$  also decrease with strake area. Furthermore, the area under the  $s-\eta$  curves - proportional to  $K_v$  - decreases with strake area. Interestingly though, each three-dimensional suction distribution across the inboard spanwise region is in good agreement with its respective prescribed curve.

The decrease in  $\alpha_{BD-TE}$  and  $K_v$  with  $R_a$  can be examined in another way if area efficiency is to be considered. Assume that with  $R_a = 0$ ,  $\alpha_{BD-TE}$  for the strake vortex is the same as for the wing leading-edge vortex breakdown, which is approximately  $8^\circ$ . With the strake in place,  $\alpha_{BD-TE}$  is significantly increased. Hence, the improvement in  $\alpha_{BD-TE}$  associated with increasing  $R_a$  will be measured relative to  $\alpha = 8^\circ$ . With the preceding in mind, a parameter  $g$  is defined which relates the ratio of change in strake area to the change in  $\Delta\alpha_{BD-TE}$  results. Explicitly,

$$g \equiv \frac{\Delta\alpha_{BD-TE}}{\left(\Delta\alpha_{BD-TE}\right)_{AD\ 24}} \frac{\left(\frac{R_a}{R_a}\right)_{AD\ 24}}{R_a} = \frac{\Delta\alpha_{BD-TE}}{R_a} \left(\frac{R_a}{\Delta\alpha_{BD-TE}}\right)_{AD\ 24}$$

The larger strake was chosen as a basis because it performed well. If  $R_a$  is reduced, it is possible to determine whether  $\Delta\alpha_{BD-TE}$  varies at the same or a different rate and thereby establish a most efficient size. Sketch (l) shows that  $\Delta\alpha_{BD-TE}$  not only changes at a rate different than  $R_a$  - if they were the same  $g$  would equal 1 - but changes at a much slower rate so as to yield  $g > 1$ . This feature points up that the largest changes in  $\Delta\alpha_{BD-TE}$  occur when the smallest strake is added to the unstraked wing. Hence, not only does  $\Delta\alpha_{BD-TE}$  not decrease at the rate of  $R_a$  reduction, but it actually decreases more slowly.



Sketch (l)

<sup>1</sup>This version utilized the side-force calculation to extract the leading-edge suction as a means of alleviating a problem associated with the leading-edge thrust computations.

Assuming that the vortex strength is related to  $K_v$ , then the impact of  $R_a$  on vortex strength may be determined by examining the impact of  $R_a$  on  $K_v$  (second curve in sketch (l)). The curve labeled  $h$  is defined similarly to  $g$  in that

$$h \equiv \frac{K_v}{(K_v)_{AD\ 24}} \frac{(R_a)_{AD\ 24}}{R_a} = \frac{K_v}{R_a} \left( \frac{R_a}{K_v} \right)_{AD\ 24}$$

This curve shows that with  $R_a$  decreasing from the value associated with the AD 24 strake, the  $K_v$  ratio first decreases at about the same rate, yielding  $h \approx 1$ , while for  $R_a < 0.15$ , the  $K_v$  ratio decreases more slowly, leading to  $h > 1$ . Hence, just as for  $\Delta\alpha_{BD-TE}$ , largest changes in vortex strength occur with the addition of the smallest strake to the unstraked wing.

Thus, taken together or separately,  $\Delta\alpha_{BD-TE}$  and  $K_v$  - although  $R_a$  dependent - do not generally decrease at the same rate as  $R_a$  for a fixed strake shape. Or conversely, once a strake vortex is established on a small strake, increasing  $R_a$  by a factor of 2 or 4 will not produce a corresponding increase in the vortex strength or in  $\Delta\alpha_{BD-TE}$ .

Efforts to find the most efficient strake area with which to develop a high value of  $\alpha_{BD-TE}$  must acknowledge a practical limit to the strake size. This limitation can be better understood when it is realized that larger areas generally mean more strake length, and that strake length is a physically constraining parameter which must be taken into account. If the strake contour and semispan change with variations in strake length, then naturally the slenderness ratio will also vary.

Figures 25 and 26 show what happens to  $\alpha_{BD-TE}$  for controlled values of slenderness ratio  $R_s$ , and for variations in the area and shape.

Effect of shape. - Slenderness ratio effects on  $\alpha_{BD-TE}$  are shown in figure 25 for strake shapes characterized by reflexive and gothic contours. All strakes have an exposed semispan ratio  $R_b$  of 0.212. The data are faired and even though there is some scatter, for  $R_s > 5$  the gothic shaped strakes reach larger angles of attack than the reflexive strakes before breakdown occurs at the wing trailing edge.

$R_s$  fixed. - Figure 26 shows the effect of strake geometry on the vortex breakdown position for a fixed value of  $R_s$ . For very small  $R_s$  values (shown in fig. 26(a)), the gothic shape gives better vortex breakdown properties than the smallest apex-cut strake. Note further that the  $s_t$  value of the gothic strake ED 13 is higher than that for the ED 4 although its  $R_a$  value is smaller.

It should be pointed out that  $\alpha_{BD-TE}$  values of approximately  $10^\circ$  or less are difficult to obtain accurately in the water tunnel because of the wing laminar flow separation and the subsequent displacement of the strake vortex occurring at these low values of  $\alpha$ .

Figure 26(b) shows the effect of  $R_a$  and shaping for two gothic shapes with a more moderate value of  $R_s$ . These strakes, ED 6 and ED 12, which were designed through different empirical means and thereby have shapes which differ, do emphasize the importance of  $R_a$  and  $s_t$  on  $\alpha_{BD-TE}$ . This figure also shows that increases in one variable lead to increases in the others for certain groups of strakes. This relationship was determined not to be true for all strake shapes; this matter is discussed further in appendix B for these strakes and others having  $R_s \approx 5.20$ . Slenderness and its coupling with leading-edge shaping are taken up next.

#### Slenderness Variation/Leading-Edge Shaping

Figures 20, 27, and 28 are used to examine the relationship between slenderness variation and leading-edge shaping and how they impact  $\alpha_{BD-TE}$  for  $R_b$  fixed,  $R_a$  fixed, and as a function of initial strake sweep.

$R_b$  fixed. - In the design of fighter configurations, the strake span may be fixed because of other design constraints. With a fixed strake span, variations in strake area required to generate the desired vortex lift result in variations in slenderness ratio. A parametric series illustrating this condition is shown in figure 20, where the vortex breakdown data and corresponding  $s-\eta$  curves for three gothic strakes of varying area and slenderness ratio are displayed. Once again,  $\alpha_{BD-TE}$  as well as  $s_t$  and the area under the  $s-\eta$  curves decrease with strake area. However, these decreases may not be attributed entirely to area effect, since  $R_s$  is also changing.

To better demonstrate the  $R_s$  dependence, a performance comparison is made between the ED 13 and AD 22 strakes. Note how  $\alpha_{BD-TE}$  for the ED 13 strake of figure 20 is less than that for the AD 22 strake shown in figure 16, although the ED 13 strake has a larger area. Similar results are also shown in the same two figures for the ED 12 and AD 23 strakes. Furthermore,  $\alpha_{BD}$  decreases at  $x/(c_r)_w = 1$  for the three strakes of figure 20, whereas breakdown at  $x/(c_r)_w = 1$  for the AD 22, AD 23, and AD 24 strakes in figure 16 occurs at the same value of  $\alpha$ . Hence, slenderness ratio is shown to be an important parameter affecting strake performance - the higher value being better.

Figures 27 and 28 show other aspects of the effects of  $R_s$  on  $\alpha_{BD-TE}$  as related to fixed values of  $R_a$  and initial strake sweep angle, respectively. In these figures,  $R_b$  and leading-edge shaping may also be variables.

$R_a$  fixed. - Figures 27(a) and 27(b) present the effects of  $R_s$  and shaping for strakes having  $R_a$  values of 0.166 (AD 23, ED 18) and 0.325 (AD 24, ED 16), respectively. These figures show that the gothic strakes AD 23 and AD 24 are obviously superior to the empirically designed strakes used for comparison. This serves to emphasize that the strake shape is an important parameter.

The  $s-\eta$  insets in figures 27(a) and 27(b) show that the suction distributions reach higher values of  $s_t$  and are more triangular for the analytically designed gothic strakes than the empirically designed ones. It would

be expected, therefore, from the original correlations (ref. 2) that the gothic strakes would promote vortex stability to higher angles of attack and that the larger gothic would be a better strake, as the water tunnel has shown and as has been noted in this paper. While the gothic strakes are clearly better performers than their empirically designed counterparts, the differences in  $s-\eta$  and  $\alpha_{BD-TE}$  may be larger than might be expected because the ED 18 and ED 16 strakes are gothic in the forward region followed by what should be a vortex-stabilizing side edge.

If the more general method of presenting suction distribution is used, i.e., the one that includes its distribution along the side edge (see appendix C), then a different result emerges as seen from the  $\bar{s}$ - $e/e_c$  set of inserts.

That is, for the  $\bar{s} = \frac{d(c_s/2)}{de} \frac{s_{ref}}{\alpha^2(b/2)_s}$  distribution determined for the empir-

ically designed strakes, both sets reach higher values at the strake-wing juncture and are often higher nearer the apex than the analytically designed strakes. Furthermore, even though the addition of the side edge is designed to strengthen the vortex, and perhaps alter the potential flow suction, the suction distributions  $\bar{s}$  versus  $e/e_c$  for the two empirically designed strakes appear to be about the same. This result is in marked contrast to the vortex breakdown results, which show that the ED 16 strake (the longer one) has a value of  $\alpha_{BD-TE}$  about  $4^\circ$  higher than the ED 18 strake. Hence, the only reliable measure of vortex stability from potential flow suction force appears to be  $s-\eta$  and  $s_t$ .

Initial strake sweep effect.— Figure 28 addresses the relationship between initial strake sweep angle and the strake vortex breakdown performance of gothic strakes with the same semispan. An examination of the results shows that the data themselves provide little in the way of a consistent relationship beyond that already known: those strakes with higher values of  $R_s$  have higher values of  $\alpha_{BD-TE}$ . Since all the strakes in figure 28 are analytically designed, are gothic in shape, and have the same  $R_b$  value, it is reasonable to assume that there would be a discernible pattern of  $\alpha_{BD-TE}$  associated with constant values of  $R_s$ . Such a pattern was inferred on the basis of the data points and is shown in the figure. The individual lines of the group are drawn according to their most likely location and are labeled "Possible Variation" lines. These lines provide a means of establishing a band around the possible  $(\alpha_{BD-TE})_{max}$  values. This band indicates that for this value of  $R_b$ , the initial sweep of the strake should decrease with increasing  $R_s$  to achieve a value of  $\alpha_{BD-TE}$  near its maximum.

Thus far, the major effects of area and slenderness coupled with the inherent leading-edge shape changes have been studied. On the basis of the preceding and in particular figure 27(b), one may ask if strakes can be designed to have an even higher value of  $\alpha_{BD-TE}$ , and if so, can such a design be accomplished with less area. This question is addressed in the next section along with other aspects of leading-edge shaping.

## Leading-Edge Shaping

This section uses figures 29 and 30 to highlight the impact of leading-edge shaping on  $\alpha_{BD-TE}$  for both major and minor shape changes.

Major changes.— Although much of the preceding discussion centered on the AD 24 strake, this section considers four different strake designs which realize comparable or better levels of performance than the AD 24 with about one-half to two-thirds its area. Their vortex breakdown characteristics and  $s-\eta$  distributions are presented in figure 29. Each of these strakes has a value of  $\alpha_{BD-TE}$  that satisfies  $20^\circ \leq \alpha_{BD-TE} \leq 22^\circ$ . As expected, the trend of increasing  $\alpha_{BD-TE}$  is consistent with the increase in strake area. Although two of the accompanying prescribed  $s-\eta$  distributions are not specifically triangular, all four have high inboard slopes and reach high levels of suction near the tip. Furthermore, the three-dimensional  $s-\eta$  curves are very similar to one another, varying slightly in overall level and  $s_t$  value. It should be noted that even for the small  $2^\circ$  variation in  $\alpha_{BD-TE}$  between the four strakes, the increase in  $s_t$  is in agreement with the increase in  $\alpha_{BD-TE}$  and  $R_a$ . This consistent relationship can be seen more clearly by examining the  $s_t$  values in figure 29. Thus,  $s_t$  appears to be a useful feature in the design process.

One may possibly reason that the relative performance gains between these four strakes are a result of significant increases in area and slenderness ratio, these features only being reflected in the  $s-\eta$  distributions. Thus, whether the vortex breakdown performance is sensitive to small perturbations in strake contour shaping has yet to be determined. If it is, then are the changes reflected in the  $s-\eta$  distribution and, in particular, are they consistent with the design criterion described earlier?

Minor changes.— In an attempt to answer these questions, a comparison is made in figure 30 which illustrates the effect of small contour changes. The vortex breakdown data and associated  $s-\eta$  distributions are presented for strakes AD 14 and AD 23, which have the same values of  $R_s$  and  $R_b$  but exhibit a small variation in contour. The angles of attack for vortex breakdown  $\alpha_{BD-TE}$  for the two strakes differ by  $2.5^\circ$ , although  $R_s$  and  $R_b$  are fixed and the areas differ by less than 4 percent.

The variation in contour between the two strakes is the result of the differences in the prescribed suction distributions used in the design procedure; the triangular distribution of AD 14 is expected to result in a more stable vortex than that for the truncated distribution of AD 23. It will be noted that the three-dimensional suction distributions are consistent with the prescribed distributions in that the distribution for the AD 14 increases more rapidly near the tip and reaches a higher value than for the AD 23. The experimental breakdown results are also consistent in that strake AD 14 displayed a higher angle of attack for vortex breakdown. Hence, this figure demonstrates that the vortex breakdown performance of a strake can be improved by making small refinements to its shape which lead to a higher value of  $s_t$ .

## Other Factors Affecting $\alpha_{BD-TE}$

### $\Delta C_p$ Specification

Strakes AD 19 and AD 9 in figure 31 demonstrate the effects of modeling the spanwise  $\Delta C_p$  distribution. The polynomial form of  $\Delta C_p$  for the AD 9 results in a reduction of  $\alpha_{BD-TE}$  but adds stability to the vortex system by lowering the rate of breakdown progression over the wing. By contrast, the constant  $\Delta C_p$  distribution leads to a higher  $\alpha_{BD-TE}$  than that of the polynomial form. It should be noted that the analytical strakes which performed best have the constant  $\Delta C_p$  specification.

### Empirical Modifications

This section uses figures 32 and 21 to examine the impact of major and minor empirical modifications of a strake on the  $\alpha_{BD}$  characteristics.

Major changes.— Figure 32(a) presents the vortex breakdown characteristics across the wing trailing edge for those strakes which are chordwise variations of the AD 24. The spanwise cut series, ED 9 to ED 11, yields an improvement in performance over the original AD 24, although the benefits are limited to small chord reductions. However, these small chord changes do lead to area reductions which are sizable (fig. 32(b)). Overall, the trailing-edge cut series shown, ED 5 to ED 7, offers a more favorable technique for reducing the chord of an existing gothic strake while maximizing the vortex breakdown angle at the wing trailing edge.

Minor changes.— Figure 21 presents  $\alpha_{BD-TE}$  for the snagged strakes. These variations of the smallest chordwise scaled strake show that using a snag in the leading edge leads to a  $2^\circ$  to  $3^\circ$  improvement in  $\alpha_{BD-TE}$ . Ahead of the trailing edge, the ED 15 shows only a slight improvement, whereas the ED 14 shows a reduction in strake performance in comparison to the ED 13. This indicates that if a snag is to be added to a strake, the more outboard locations are preferable.

### CONCLUDING REMARKS

This paper has described a water-tunnel study of the vortex breakdown characteristics of 43 analytically and empirically designed vortex strakes tested in combination with a moderate-aspect-ratio trapezoidal wing-body. The analytic strake designs were based on a series of prescribed leading-edge suction distributions used in combination with a simplified flow which is related to three-dimensional potential flow through certain simplifying assumptions. These prescribed suction distributions considered the general observation made in an earlier delta-wing study, in that a relationship was shown to exist between increasing suction toward the tip and improved vortex stability. This relationship was the design criterion, and the designed strakes employed here were hypothesized to exhibit a similar behavior.

A wide range of strake sizes and slenderness ratios were investigated, and this study presents an extensive data base which may be of assistance in the preliminary phase of maneuvering-aircraft strake design. The effects of the major design parameters, i.e., size, span, slenderness, and leading-edge shaping, on the vortex breakdown characteristics are documented and analyzed in relation to the leading-edge suction distributions. The ensuing analysis not only confirms that increasing area and slenderness are important ways to increase the vortex breakdown angle, but that with proper leading-edge gothic shaping it is possible to obtain the same, or an even higher breakdown angle using about one-half to two-thirds the area of a larger gothic strake. In addition, it was noted that, consistent with the design criterion, those strakes with leading-edge suction distributions which increase more rapidly near the tip to a higher value generally produce a more stable vortex.

Langley Research Center  
National Aeronautics and Space Administration  
Hampton, VA 23665  
May 22, 1980

## APPENDIX A

### BASIC EQUATIONS USED IN STRAKE SHAPE DEVELOPMENT

Starting with an attached-flow pressure distribution given by

$$\frac{\Delta C_p(\theta, \eta)}{\alpha} = \frac{2q_o(\eta)}{\alpha q_\infty c} \cot \frac{\theta}{2} + \sum_{j=1}^{N-1} \frac{2q_j(\eta)}{\alpha q_\infty c} \sin j\theta$$

the local-suction distribution is shown (ref. 10) to be

$$\frac{c_s c}{\alpha^2} = \frac{\sqrt{\beta^2 + \tan^2 \Lambda_\ell(\eta)}}{2\pi \cos \Lambda_\ell(\eta)} \left[ \frac{2q_o(\eta)}{\alpha q_\infty c} \right]^2 c$$

This equation relates suction distribution to the coefficient of the  $\cot(\frac{\theta}{2})$  term, and from this relationship, the local leading-edge sweep angle  $\Lambda_\ell(\eta)$ , and the chord  $c$  can be expressed in terms of each other. Another equation in which  $\Lambda_\ell(\eta)$  and  $c$  appear together is the simple geometrical relationship

$$c = c_r - \frac{b}{2} \int_0^\eta (\tan \Lambda_\ell(\bar{\eta}) - \tan \Lambda_t) d\bar{\eta}$$

However, to obtain a solution, some assumptions will be needed with regard to  $\frac{c_s c}{\alpha^2}$  and  $\frac{\Delta C_p(\theta, \eta)}{\alpha}$ . For example, the correlation between suction distributions which peak toward the tip and the resulting large values of  $\alpha_{BD-TE}$  could be used. This can be done by assuming that

$$\frac{c_s c}{\alpha^2} = (a_1 + b_1 \eta) \frac{b}{2}$$

and

$$s = \frac{c_s c}{\alpha^2 \frac{b}{2}} = a_1 + b_1 \eta$$

The second assumption would be that since the planar strakes are designed to produce separated flow with reattachment - i.e., vortex flow - the associated leading-edge pressures must conceptually, as well as in reality, exceed an unspecified local limiting value beginning at some small angle of attack. This means that for the attached-flow pressure distribution, the region of

## APPENDIX A

interest is near the leading edge, i.e., where  $\theta$  and  $x'/c$  are small. Hence, one approximation is to set

$$\frac{\Delta C_p(\theta, \eta)}{\alpha} \approx \frac{2q_\infty(\eta)}{\alpha q_\infty c} \cot\left(\frac{\theta}{2}\right)$$

with the assumption that  $\frac{C_{p,l}}{\alpha} = -\frac{C_{p,u}}{\alpha} = \frac{\Delta C_p}{2\alpha} > \left(\frac{C_p}{\alpha}\right)$  limit

If an additional assumption<sup>2</sup> is made that across the span (see fig. 3)

$$\frac{\Delta C_p(\theta, \eta)}{\alpha} = \text{Constant} = C_0$$

at constant  $\theta$  or  $x'/c$ , which means that the sectional lift contribution from the  $\cot(\theta/2)$  term is constant, then

$$\frac{2q_\infty(\eta)}{\alpha q_\infty c} \approx \text{Constant} = C_1$$

The preceding discussion implies that if the flow separates anywhere, it separates everywhere simultaneously. These assumptions given previously and those summarized in figure 3 are used to go from a three-dimensional potential flow to a related flow, on a planar surface, in which the solution is to be made. This is done in order to determine the analytic relationship between the suction prescription and the resulting geometry.

Putting all the assumptions together yields

$$(a_1 + b_1\eta) \frac{b}{2} = \frac{\sqrt{\beta^2 + \tan^2 \Lambda_\ell(\eta)}}{2\pi \cos \Lambda_\ell(\eta)} c_1^2 c$$

$$(\bar{a} + \bar{b}\eta) \frac{b}{2} = \frac{\sqrt{\beta^2 + \tan^2 \Lambda_\ell(\eta)}}{2\pi \cos \Lambda_\ell(\eta)} \left\{ c_r - \frac{b}{2} \int_0^\eta [\tan \Lambda_\ell(\tilde{\eta}) - \tan \Lambda_t] d\tilde{\eta} \right\}$$

where

$$\bar{a} = \frac{a_1}{c_1^2} \quad \text{and} \quad \bar{b} = \frac{b_1}{c_1^2}$$

---

<sup>2</sup>Other assumptions concerning  $\Delta C_p(\theta, \eta)/\alpha$  and  $\theta$  could be made. For example,  $\Delta C_p(\theta, \eta)/\alpha$  could take on a three-dimensional variation at constant  $\theta$ .

## APPENDIX A

At  $\eta = 0$ , the initial sweep of the strake can be determined by

$$\Lambda_\ell(\eta=0) = \sin^{-1} \left[ \left( \frac{c_r^2 M^2}{2\pi^2 \bar{a}^2 b^2} + 1 - \frac{\sqrt{M^4 c_r^4 + 4\pi^2 \bar{a}^2 b^2 c_r^2}}{2\pi^2 \bar{a}^2 b^2} \right)^{1/2} \right] \quad (A1)$$

For  $\eta > 0$ ,  $\Lambda_\ell(\eta)$  can be solved by iteration from the following initial value problem:

$$c_r - \frac{(\bar{a} + \bar{b}\eta)(b/2) 2\pi}{\sqrt{\beta^2 \sec^2 \Lambda_\ell(\eta) + \sin^2 \Lambda_\ell(\eta) \sec^4 \Lambda_\ell(\eta)}} = \frac{b}{2} \int_0^\eta [\tan \Lambda_\ell(\bar{\eta}) - \tan \Lambda_t] d\bar{\eta} \quad (A2)$$

This solution has been coded for the Control Data 6000 series digital computer and typically executes in less than 2 seconds for a single set of parameters. It should be noted that  $\bar{a}$  has, in general, to satisfy the inequality

$$\bar{a} \geq \frac{c_r}{\pi b} \geq 0$$

in order for  $\Lambda_\ell(\eta=0)$  to be determinable. (See eq. (A1).)

## APPENDIX B

### ANOMALIES IN RELATING $\alpha_{BD-TE}$ TO $s_t$

This appendix presents two specific anomalies of the  $\alpha_{BD-TE}$  data and its relationship with  $s_t$  as determined from an examination of the data.

Figure 33 repeats vortex breakdown characteristics of the ED 6 and ED 12 strakes shown in figure 26(b) and adds the corresponding data for the ED 2 and Strake III configurations. It will be noted that the only geometric quantity the four strakes have in common is  $R_s$ , which is approximately 5.2. Comparison of the ED 2 and ED 12 data in figure 33 indicates that the ED 12 gothic strake is a better performer with a smaller area, just as noted in the discussion of figure 26(a). However, unlike the strakes of figure 26(a), these two strakes do not demonstrate increasing  $s_t$  with  $\alpha_{BD-TE}$ , but just the opposite.

The first anomaly seems to point out that not only  $s_t$  is important but also the distribution. To explore this anomaly further, consider using  $K_v$  as a weighted value of  $s-\eta$ . Since the ED 2 strake is a part of the apex-cut family, a graph has been prepared (fig. 34) which shows  $K_v$ ,  $\alpha_{BD-TE}$ , and  $s_t$  as a function of  $R_a$ . These same parameters are also shown on a companion chart for the trailing-edge cut family because they demonstrated the usual relationship between  $\alpha_{BD-TE}$  and  $s_t$ . The difference between the two types is striking in that for the trailing-edge cut family all three parameters basically decrease with  $R_a$ , whereas only  $K_v$  and  $\alpha_{BD-TE}$  decrease over much of the  $R_a$  range for the apex-cut series. This says that what happens at the tip is important, but if the leading-edge suction is low inboard and kept low because the inboard sweep is held constant, then the overall performance  $\alpha_{BD-TE}$  of the strake will be reduced.

The second anomaly is noted by comparing the data of Strake III to those of the others; although it has one of the lowest  $s_t$  values, Strake III has a relatively high value of  $K_v$  and its  $\alpha_{BD-TE}$  is the highest of the strakes tested. Further note that its area is not the largest of those tested either, though its semispan is. Apart from these geometrical distinctions the most obvious one is its leading-edge shape. Since many of the strakes tested were gothic or empirical deviations from a gothic, additional study is needed for strakes having shapes associated with Strake III because of its good performance, efficient area usage, and the  $\alpha_{BD-TE}$  versus  $s_t$  anomaly it possesses with respect to the gothic strakes.

## APPENDIX C

### SUCTION DISTRIBUTIONS

The suction distributions that have been presented in past studies have

been of the form  $\frac{c_s c}{\alpha^2 (b/2)_s}$  which is entirely adequate for strakes without streamwise edges. However, for  $\Lambda_\ell = 90^\circ$ , the preceding suction parameter is no longer appropriate; the more general one might be used. To develop this more general parameter, it is necessary to examine the thrust force along the edge. For example, along the leading edge of the strake

$$C_T q_\infty s_{ref} = 2 \int_0^{(b/2)_s} c_s c q_\infty \cos \Lambda_\ell(y) dy$$

and so

$$dC_T s_{ref} = 2c_s c \cos \Lambda_\ell(y) dy$$

or

$$\frac{dC_T}{dy} \frac{s_{ref}}{\alpha^2 (b/2)_s} = \frac{c_s c \cos \Lambda_\ell(y)}{\alpha^2 (b/2)_s}$$

From reference 10

$$\frac{d(T/2)}{dy} = \frac{d(C_T q_\infty s_{ref}/2)}{dy} = \frac{d(S/2)}{de} = \frac{d(C_s q_\infty s_{ref}/2)}{de}$$

or

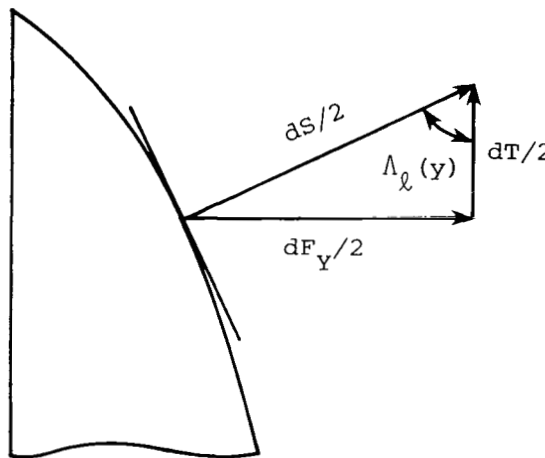
$$\frac{dC_T}{dy} = \frac{dC_s}{de}$$

and

$$\frac{d(C_s/2)}{de} \frac{s_{ref}}{\alpha^2 (b/2)_s} = \frac{c_s c \cos \Lambda_\ell(y)}{\alpha^2 (b/2)_s}$$

## APPENDIX C

Note that from sketch (m),  $\frac{1}{2} dC_Y q_\infty s_{ref} = \frac{1}{2} dC_S q_\infty s_{ref} \sin \Lambda_\ell(y)$



Sketch (m)

From sketch (n) it is determined that

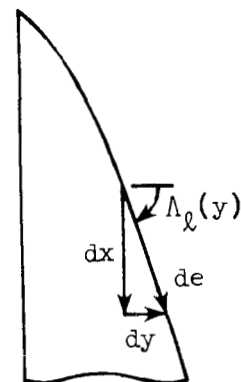
$$\frac{dy}{de} \equiv \cos \Lambda_\ell(y)$$

and

$$\frac{dx}{de} \equiv \sin \Lambda_\ell(y)$$

Therefore, combining the preceding yields

$$\frac{dC_S}{de} = \frac{dC_T}{dy} = \frac{dC_Y}{dx}$$



Sketch (n)

Thus, a more general form that is applicable for  $\Lambda_\ell(y) \leq 90^\circ$  is just

$$\frac{d(C_S/2)}{de} \frac{s_{ref}}{\alpha^2 (b/2)_s} = \frac{d(C_Y/2)}{dx} \frac{s_{ref}}{\alpha^2 (b/2)_s} = \frac{C_Y (b/2) s_l}{\alpha^2 (b/2)_s} \equiv \frac{1}{s}$$

This form is utilized in the inserts in figures 27(a) and 27(b).

#### REFERENCES

1. Headley, Jack W.: Analysis of Wind Tunnel Data Pertaining to High Angle of Attack Aerodynamics. Volume I - Technical Discussion and Analysis of Results. AFFDL-TR-78-94, U.S. Air Force, July 1978. (Available from DTIC as AD A069 646.)
2. Lamar, John E.: Analysis and Design of Strake-Wing Configurations. *J. Aircr.*, vol. 17, no. 1, Jan. 1980, pp. 20-27.
3. Wentz, William H., Jr.; and Kohlman, David L.: Wind Tunnel Investigations of Vortex Breakdown on Slender Sharp-Edged Wings. NASA CR-98737, 1968.
4. Margason, Richard J.; and Lamar, John E.: Vortex-Lattice FORTRAN Program for Estimating Subsonic Aerodynamic Characteristics of Complex Planforms. NASA TN D-6142, 1971.
5. Lamar, John E.; and Gloss, Blair B.: Subsonic Aerodynamic Characteristics of Interacting Lifting Surfaces With Separated Flow Around Sharp Edges Predicted by a Vortex-Lattice Method. NASA TN D-7921, 1975.
6. Lamar, J. E.: Some Recent Applications of the Suction Analogy to Vortex-Lift Estimates. *Aerodynamic Analyses Requiring Advanced Computers, Part II*, NASA SP-347, 1975, pp. 985-1011.
7. Lamar, John E.: Recent Studies of Subsonic Vortex Lift Including Parameters Affecting Stable Leading-Edge Vortex Flow. *J. Aircr.*, vol. 14, no. 12, Dec. 1977, pp. 1205-1211.
8. Frink, Neal T.: Water Tunnel and Analytical Investigation of the Effect of Strake Design Variables on Strake Vortex Breakdown Characteristics in the Presence of Wing-Body. M.S. Thesis, North Carolina State Univ., 1979.
9. Luckring, James M.: Aerodynamics of Strake-Wing Interactions. *J. Aircr.*, vol. 16, no. 11, Nov. 1979, pp. 756-762.
10. Wagner, Siegfried: On the Singularity Method of Subsonic Lifting-Surface Theory. AIAA Paper No. 69-37, Jan. 1969.



TABLE I.- PERTINENT GEOMETRIC PROPERTIES OF ANALYTICALLY  
DESIGNED STRAKES

Strake designation	$\Lambda_\ell(\eta=0)$ , deg	$R_s$	$R_b$	$R_a$
AD 1	76.76	4.92	0.212	0.100
AD 2	83.55	6.51	.212	.100
AD 3	77.14	5.33	.212	.110
AD 4	83.75	7.04	.212	.112
AD 5	72.06	3.94	.212	.079
AD 6	71.29	3.55	.212	.070
AD 7	69.01	4.99	.212	.126
AD 8	80.70	5.76	.212	.108
AD 9	75.10	10.65	.197	.183
AD 10	79.41	5.91	.212	.112
AD 11	73.29	3.56	.212	.066
AD 12	73.43	3.01	.212	.038
AD 13	77.19	8.69	.212	.199
AD 14	46.18	6.99	.212	.172
AD 15	63.65	5.92	.212	.140
AD 16	65.52	5.29	.212	.123
AD 17	70.78	7.77	.212	.185
AD 18	74.54	4.98	.212	.103
AD 19	56.80	8.50	.212	.205
AD 20	66.14	5.07	.212	.127
AD 21	69.97	4.65	.212	.092
AD 22	60.65	7.00	.144	.077
AD 23	60.65	7.00	.212	.166
AD 24	60.65	7.00	.297	.325

TABLE II.- BASIC DATA PRESENTATION AND PERTINENT SUCTION AND  
PRESSURE CHARACTERISTICS

Basic data		Suction distribution prescriptions							Pressure specification
Fig.	Strake designation	s- $\eta$ group	Initial value, $a_1$	Initial slope, $b_1$	Suction break, $\eta^*$ , fraction of $b/2$	Outboard slope	Tip value, $s_t$	Fig.	
9	AD 1	8	12	-15	0.65	48	19.05	5(a)	Constant
9	AD 2	8	12	-15	.65	48	19.05	5(a)	Polynomial
9	AD 3	8	14	-15	.65	48	21.05	5(a)	Constant
9	AD 4	8	14	-15	.65	48	21.05	5(a)	Polynomial
10	AD 5	10	5	-5	.65	23.6	10	5(a)	Constant
10	AD 6	10	4	-5	.65	23.6	9	5(a)	Polynomial
11	AD 7	11	5	-5	.65	166	60	5(a)	Constant
11	AD 8	11	5	-5	.65	166	60	5(a)	Polynomial
12	AD 9	12	4	101	.65	-51	52	5(a)	Constant
12	AD 10	12	4	0	.65	137	52	5(a)	Polynomial
13	AD 11	13	5	-8	.50	8	5	5(a)	Constant
10	AD 12	10	4	-5	.65	-2.1	0.0	5(a)	Polynomial
14	AD 13	3	25	48	.65	-12	52	5(b)	Constant
14	AD 14	3	2	48	.65	53.7	52	5(b)	Polynomial
15	AD 15	5	4	20	.90	380	60	5(b)	Constant
15	AD 16	4	4	9.23	.65	48	26.8	5(b)	Polynomial
15	AD 17	6	10	48	1.00	-----	58	5(b)	Constant
10	AD 18	10	9	-5	.65	23.6	14	5(b)	Polynomial
12	AD 19	12	4	101	.65	-51	52	5(b)	Constant
12	AD 20	12	4	0	.65	137	52	5(b)	Polynomial
13	AD 21	13	5	6	.50	-6	5	5(b)	Constant
16	AD 22	1	4	48	.65	0	35.2	5(b)	Polynomial
16	AD 23	1	4	48	.65	0	35.2	5(b)	Constant
16	AD 24	1	4	48	.65	0	35.2	5(b)	Polynomial

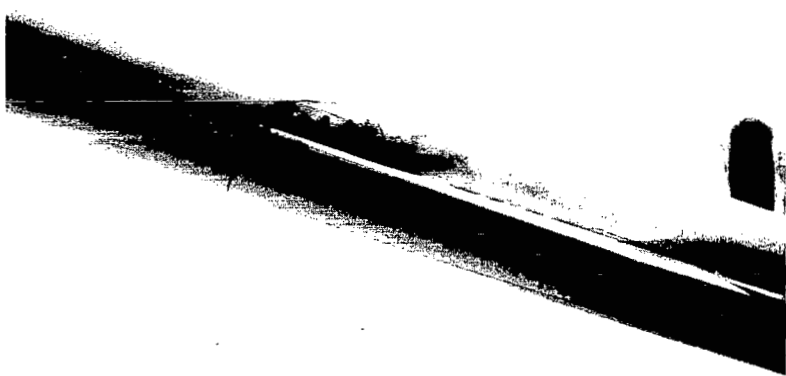
TABLE III.- PERTINENT GEOMETRIC PROPERTIES OF EMPIRICALLY DESIGNED STRAKES

Strake designation	$\Lambda_\ell (\eta=0)$ , deg	$R_s$	$R_b$	$R_a$	Chord modification
AD 24	60.65	7.00	0.297	0.325	(a)
ED 1	60.00	6.10	0.297	0.305	Removal of apex region
ED 2	60.00	5.19	.297	.266	
ED 3	60.00	3.98	.297	.195	
ED 4	60.00	2.77	.297	.114	
ED 5	60.65	5.83	0.262	0.188	Removal of trailing-edge region
ED 6	60.65	5.22	.226	.124	
ED 7	60.65	4.53	.181	.065	
ED 8	60.65	3.65	.119	.021	
ED 9	73.32	7.79	0.253	0.259	Removal of inboard edge region
ED 10	77.57	8.62	.208	.192	
ED 11	80.12	9.59	.163	.131	
ED 12	56.89	5.18	0.297	0.227	Chordwise scaling
ED 13	50.42	2.78	.297	.098	
ED 14	50.42	2.78	0.297	0.078	Chordwise extension (snag) on ED 13 strake
ED 15	50.42	2.78	.297	.076	
ED 16	50.42	5.63	0.297	0.325	Addition of side-edge/trailing-edge area to ED 13 strake
ED 17	50.42	4.64	.297	.246	
ED 18	50.42	3.63	.297	.166	
Strake III (ref. 9)	80.35	5.18	0.353	0.267	(b)

<sup>a</sup>Analytically designed strake from which empirical variations are made.<sup>b</sup>Not an empirical variation of the AD 24 strake.



Figure 1.- Photograph of vortex flow generated by highly swept maneuver strakes on the General Dynamics YF-16 lightweight fighter, from Aviation Week and Space Technology, June 16, 1975, p. 23. (Copyright Aviation Week and Space Technology, reprinted with permission.)



L-80-149

Figure 2.- Water-tunnel flow-field visualization of  $44^{\circ}$  leading-edge-sweep trapezoidal wing in forward position.  $\alpha = 20^{\circ}$ .

### "RELATED FLOW" ASSUMPTIONS

- ONLY CONCERNED WITH FLOW NEAR LE
- ONLY COT ( $\theta/2$ ) CHORD LOAD USED
- $\Delta C_p$  SPECIFIED SPANWISE
- SHARP LEADING-EDGE SIMULATION
- NO PHYSICAL OR INDUCED CAMBER ALLOWED

### OTHER ASSUMPTIONS

- TRIANGULAR SUCTION DISTRIBUTION-PRESCRIBED
- PERFORMANCE: ISOLATED STRAKE (R.F.)  $\rightarrow$  STRAKE-WING-BODY (3-D FLOW)

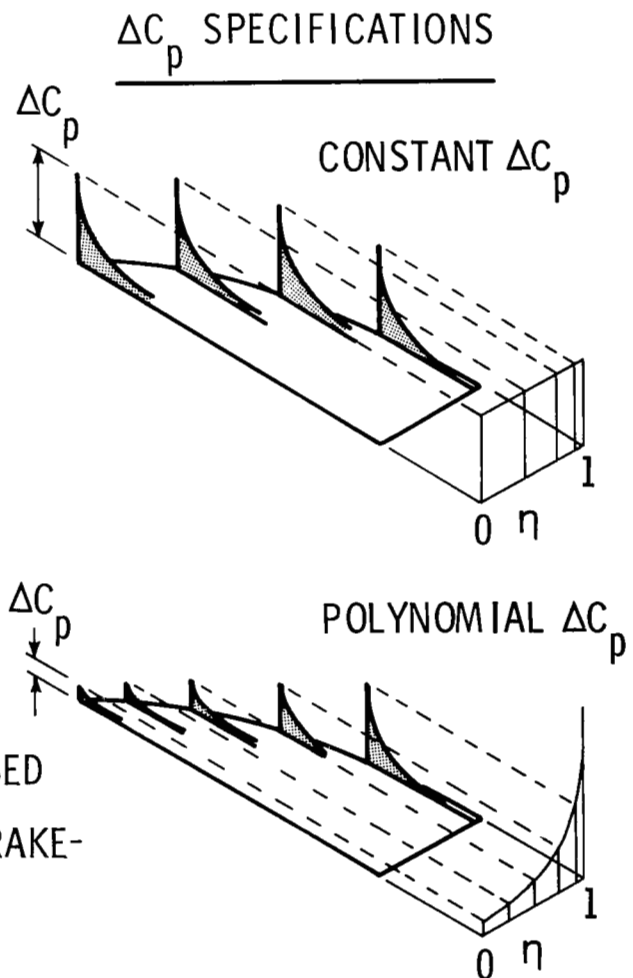


Figure 3.- Features of isolated strake design process.

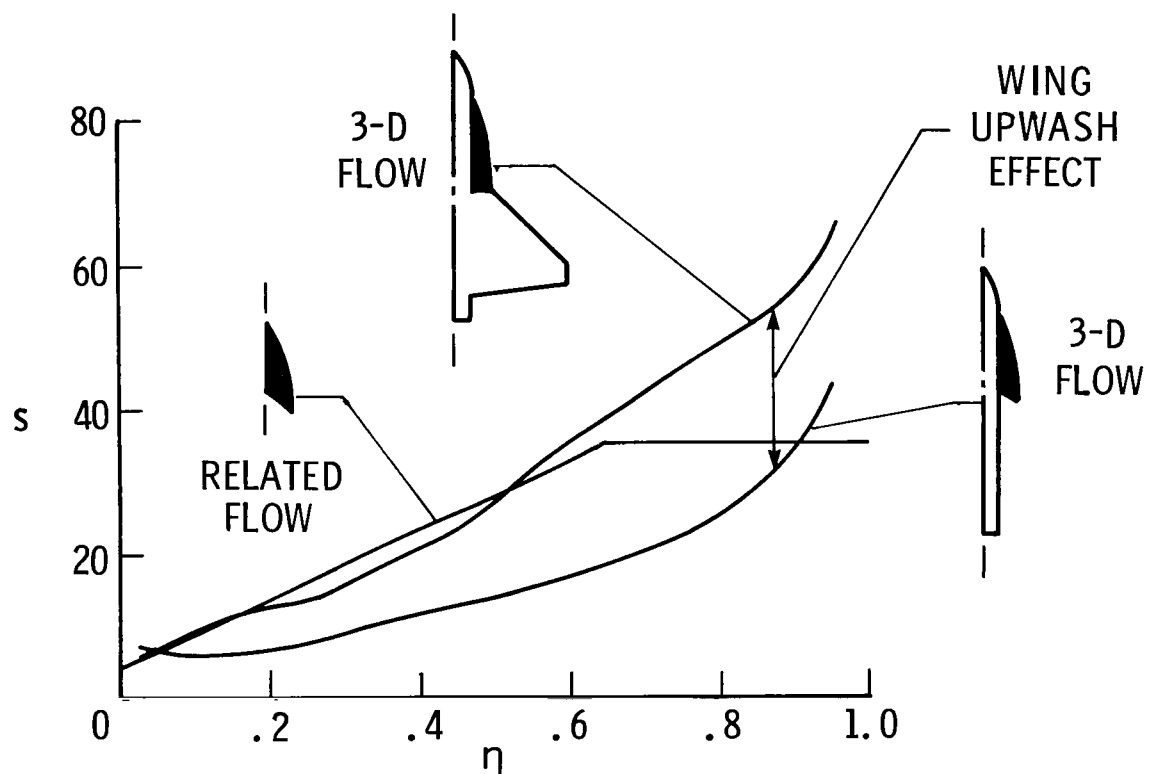
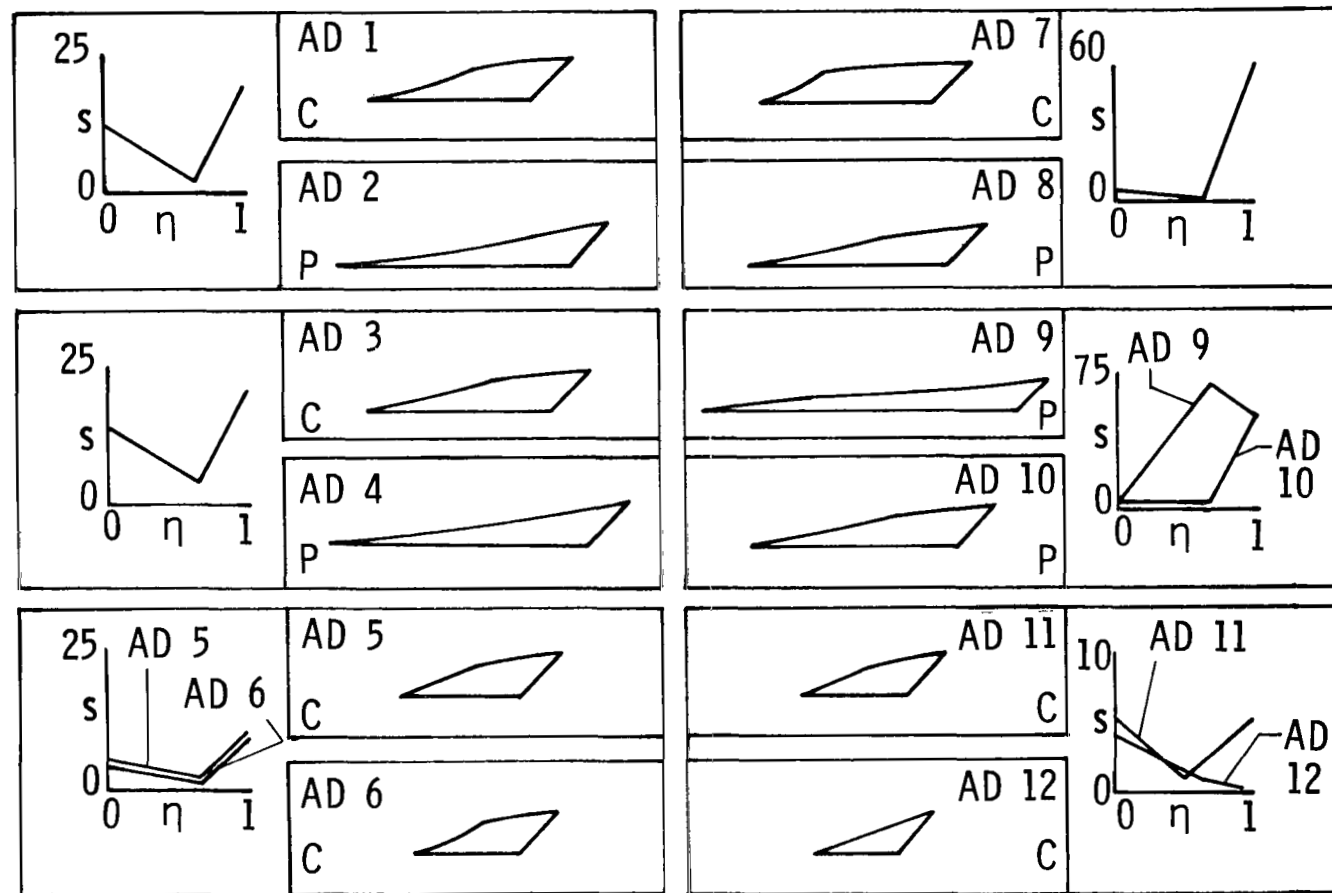


Figure 4.- Effect of flow-field and aerodynamic components on AD 23 strake suction distribution.



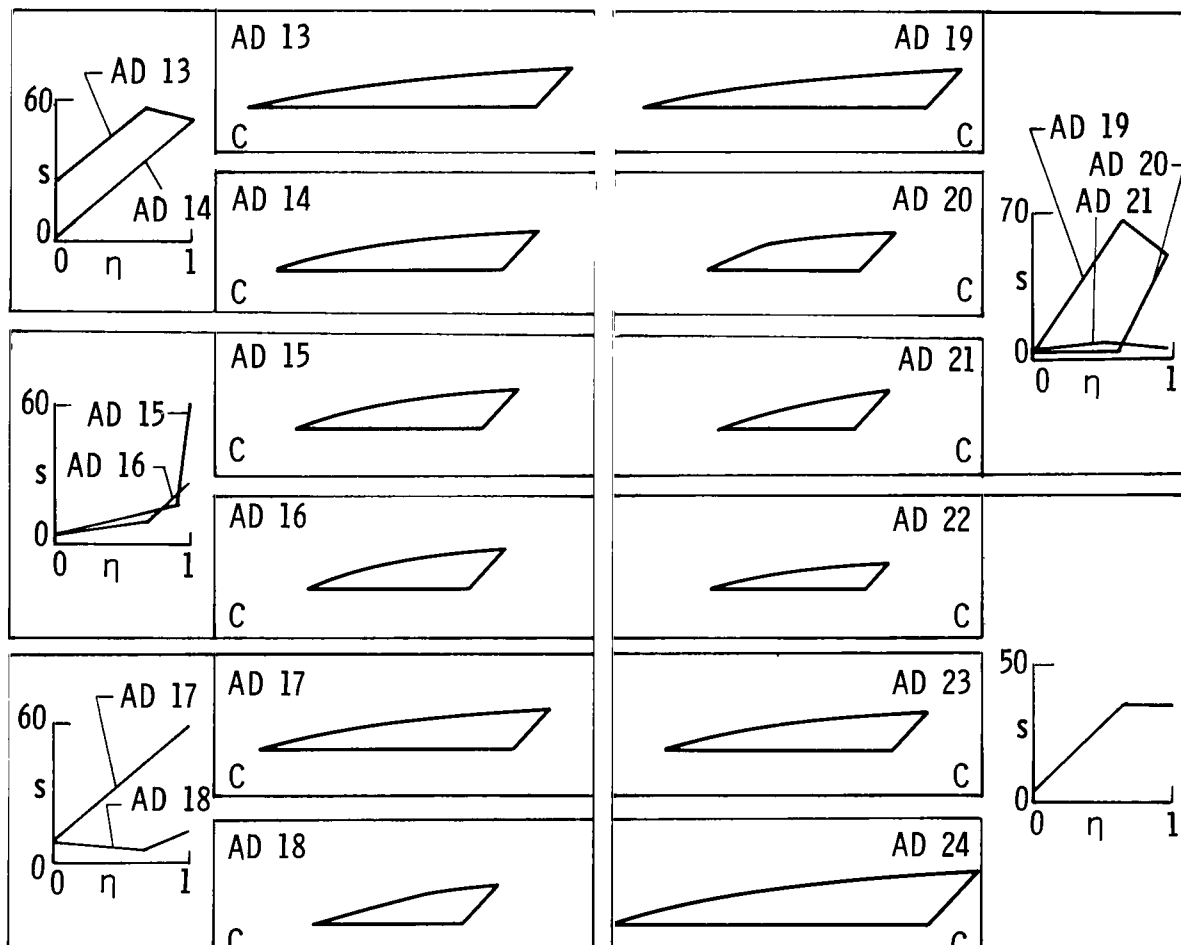
C - CONSTANT  $\Delta C_p$

P - POLYNOMIAL  $\Delta C_p$

$$s = \frac{c_s c}{\alpha^2 (b/2)}_s$$

(a) Analytical, reflexive group.

Figure 5.- Analytically and empirically designed strakes.

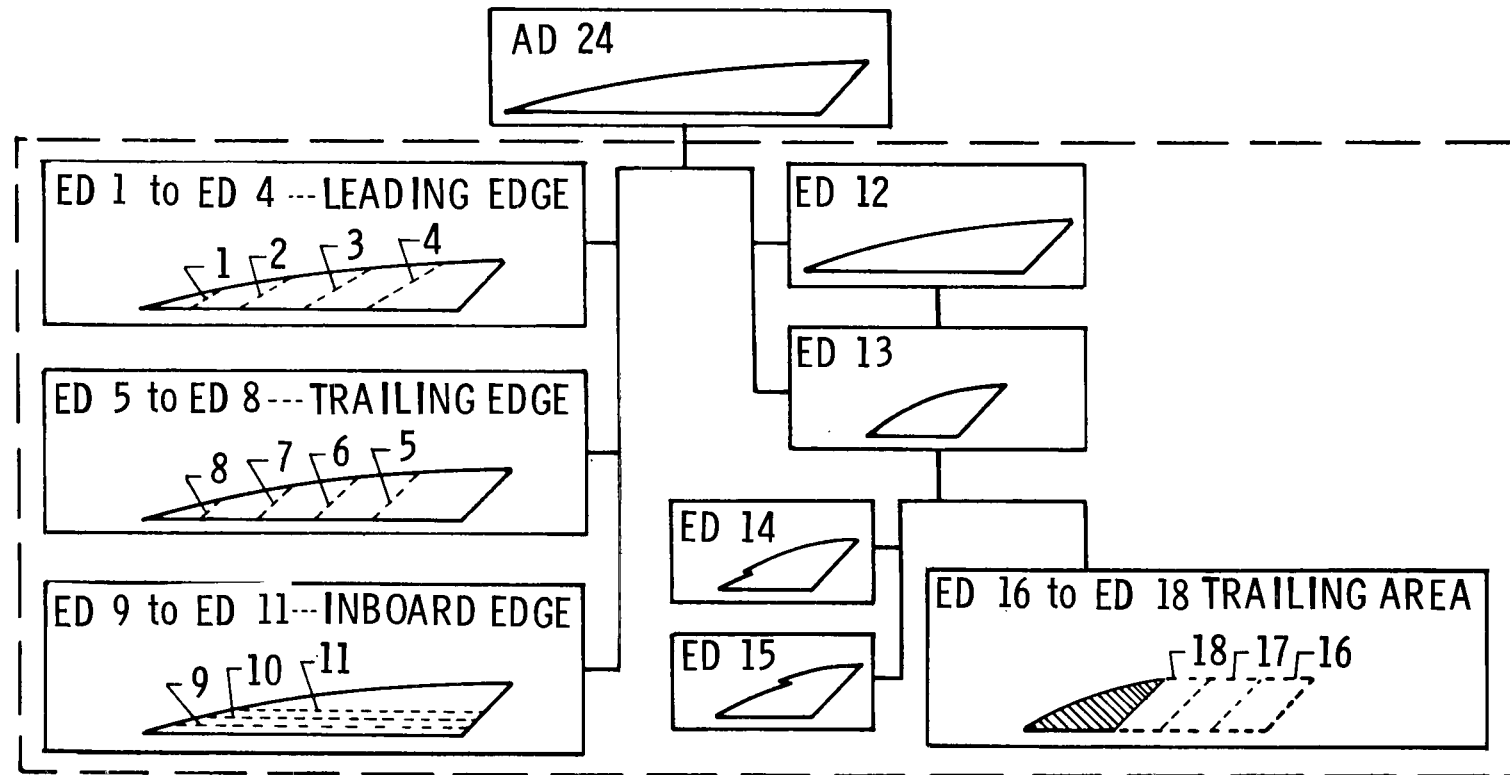


C - CONSTANT  $\Delta C_p$

$$s = \frac{c_c}{\alpha^2 (b/2)} \quad \boxed{\text{EMPIRICAL DESIGNS}}$$

(b) Analytical, gothic group.

Figure 5.- Continued.



(c) Empirical group.

Figure 5.- Concluded.

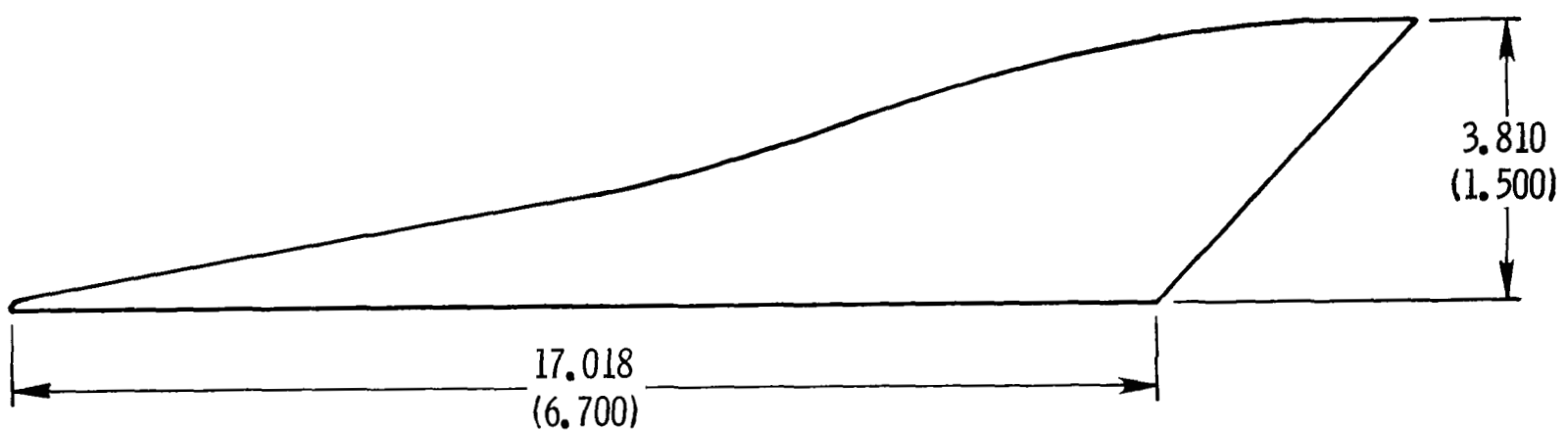


Figure 6.- Strake III of reference 9. Dimensions are in cm (in.).

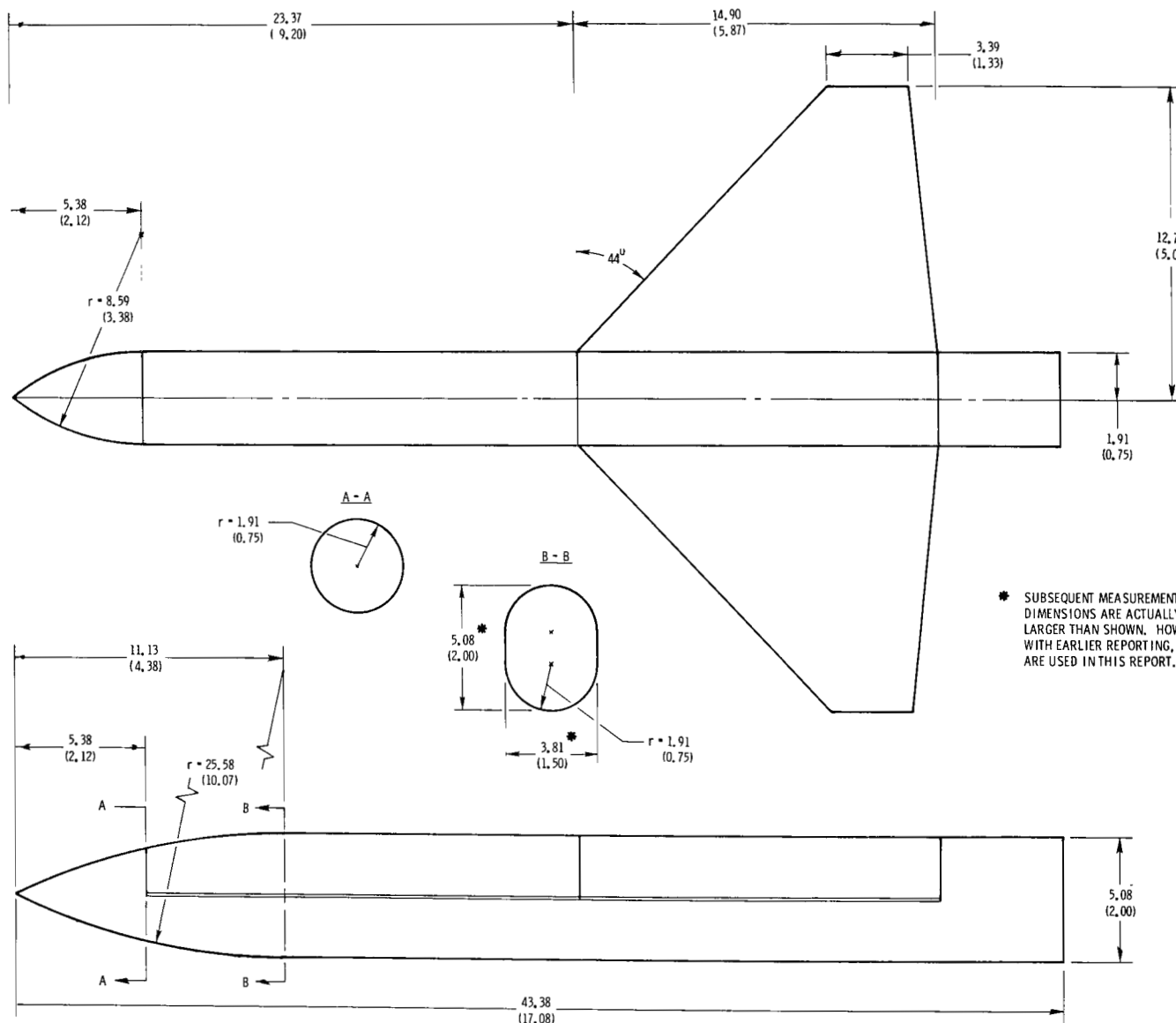
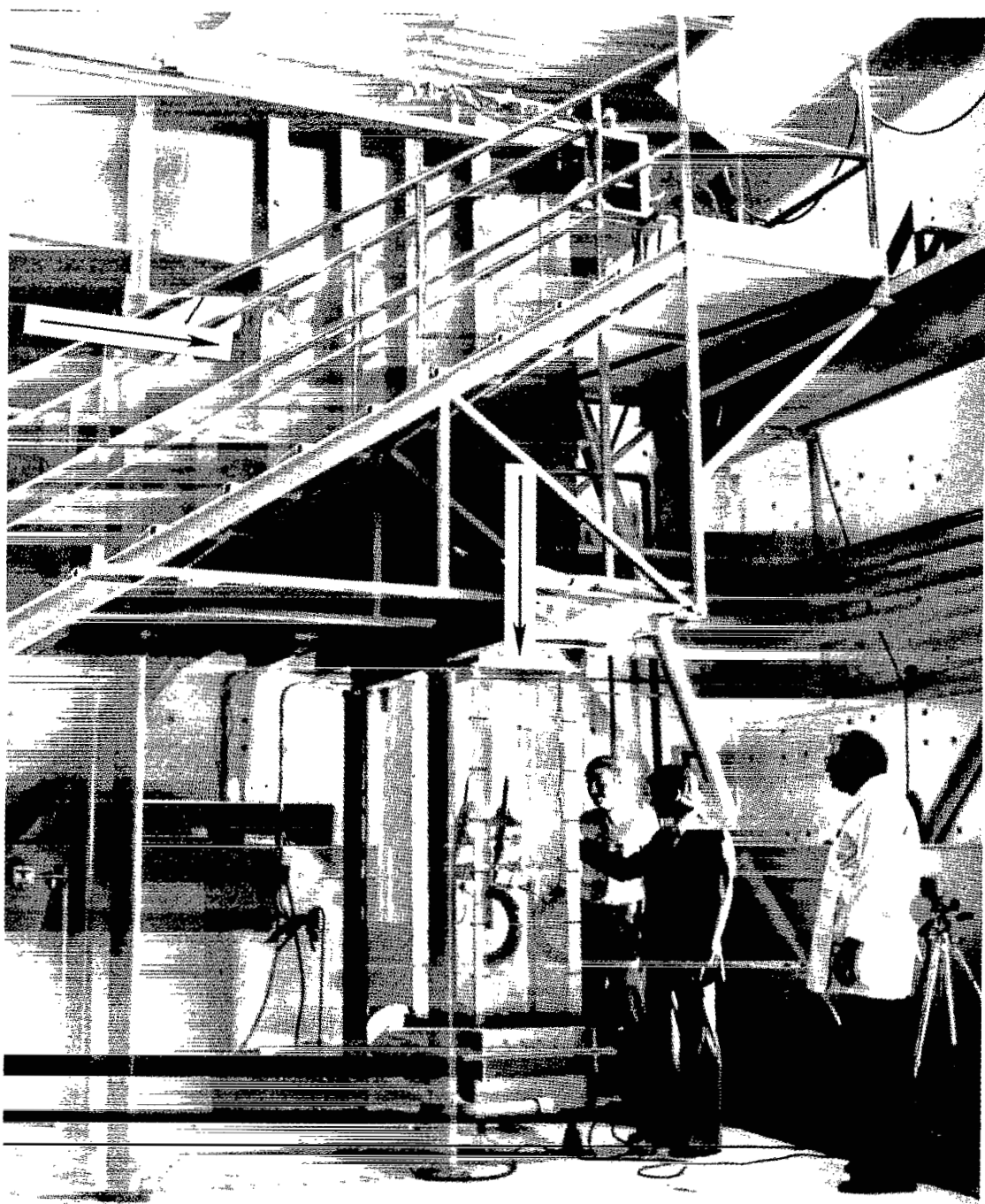


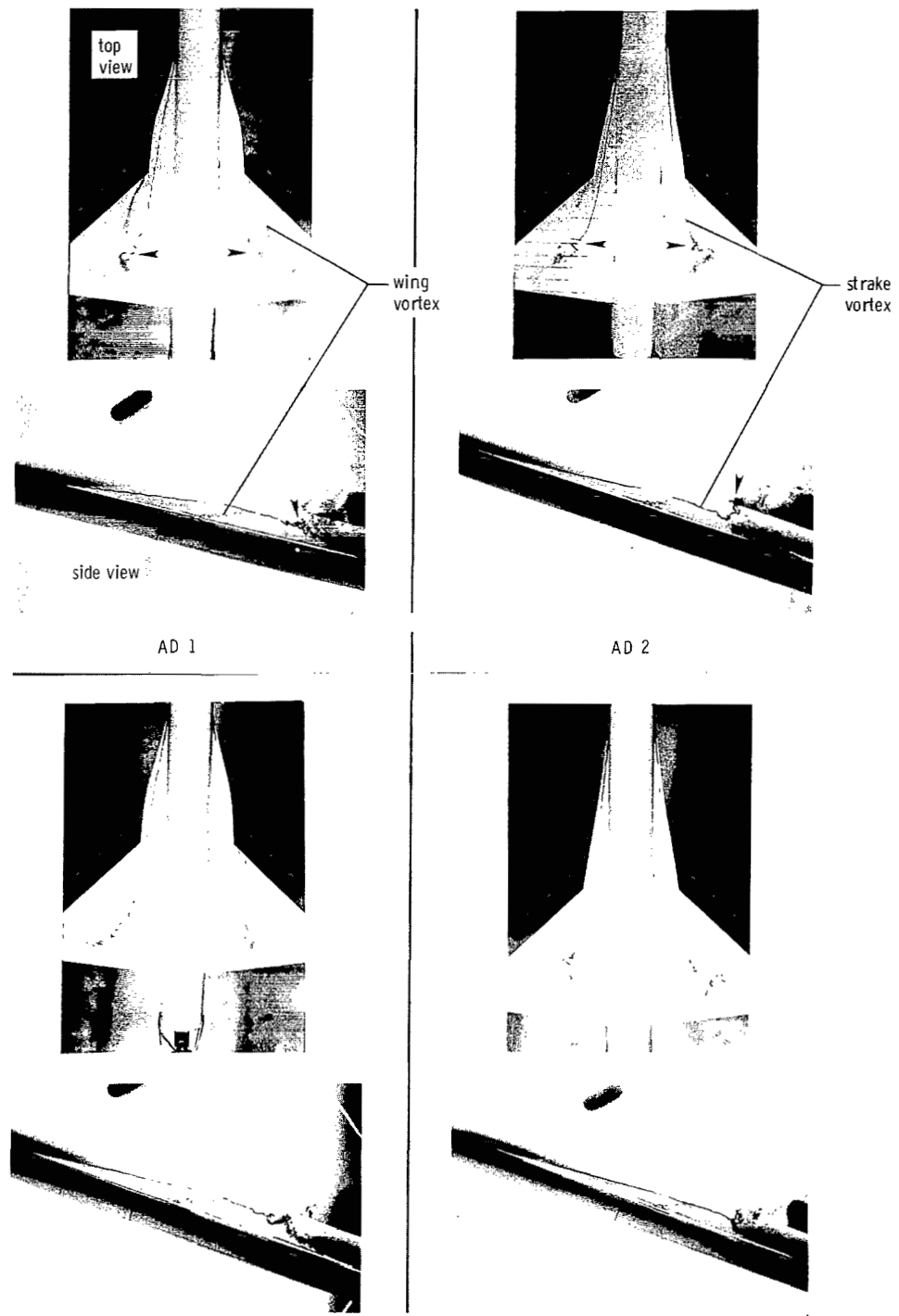
Figure 7.- Drawing of water-tunnel wing-fuselage model with wing in forward position. Aft wing position is 2.21 cm (0.87 in.) rearward. Dimensions are in cm (in.) unless otherwise noted.



L-80-150

Figure 8.- Northrop 16- by 24-inch Diagnostic Water Tunnel.

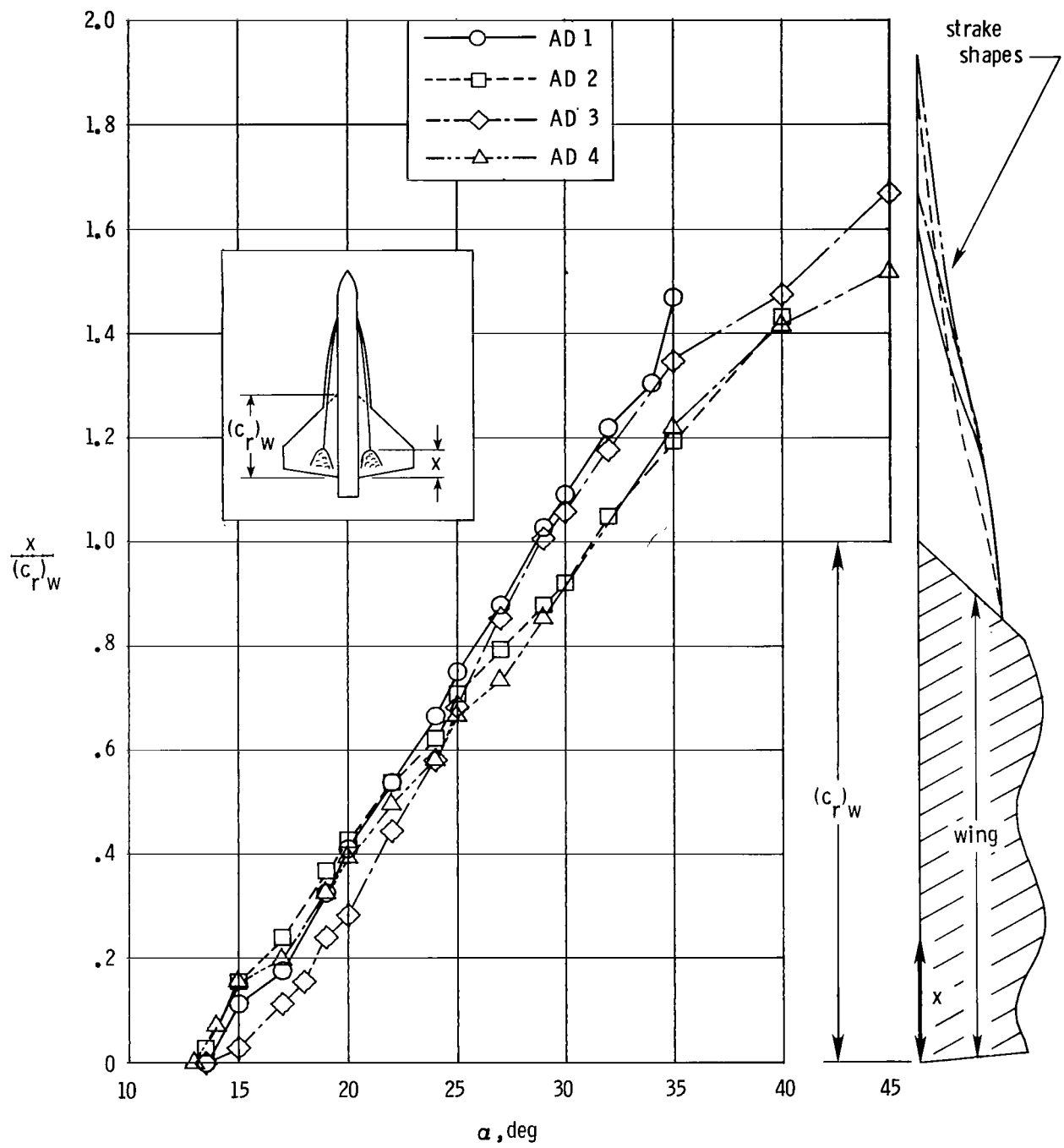
→ denotes vortex breakdown



(a) Strake and wing vortex patterns at  $\alpha = 20^\circ$ .

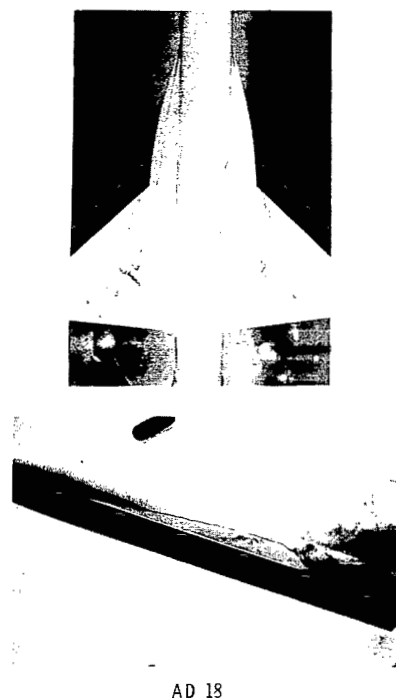
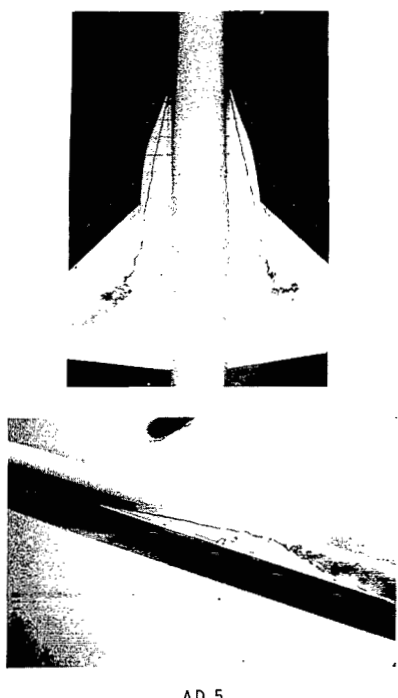
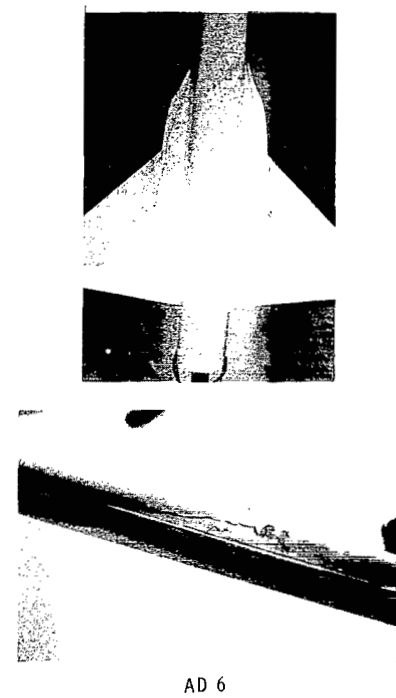
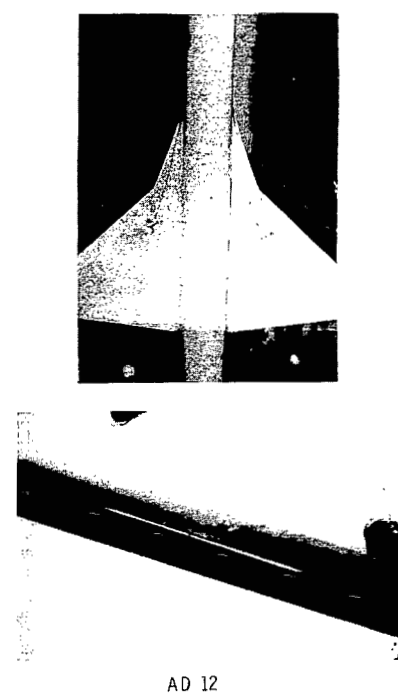
L-80-151

Figure 9.- Water-tunnel photographs and strake vortex breakdown characteristics for strakes analytically designed, group 8.



(b) Strake vortex breakdown position.

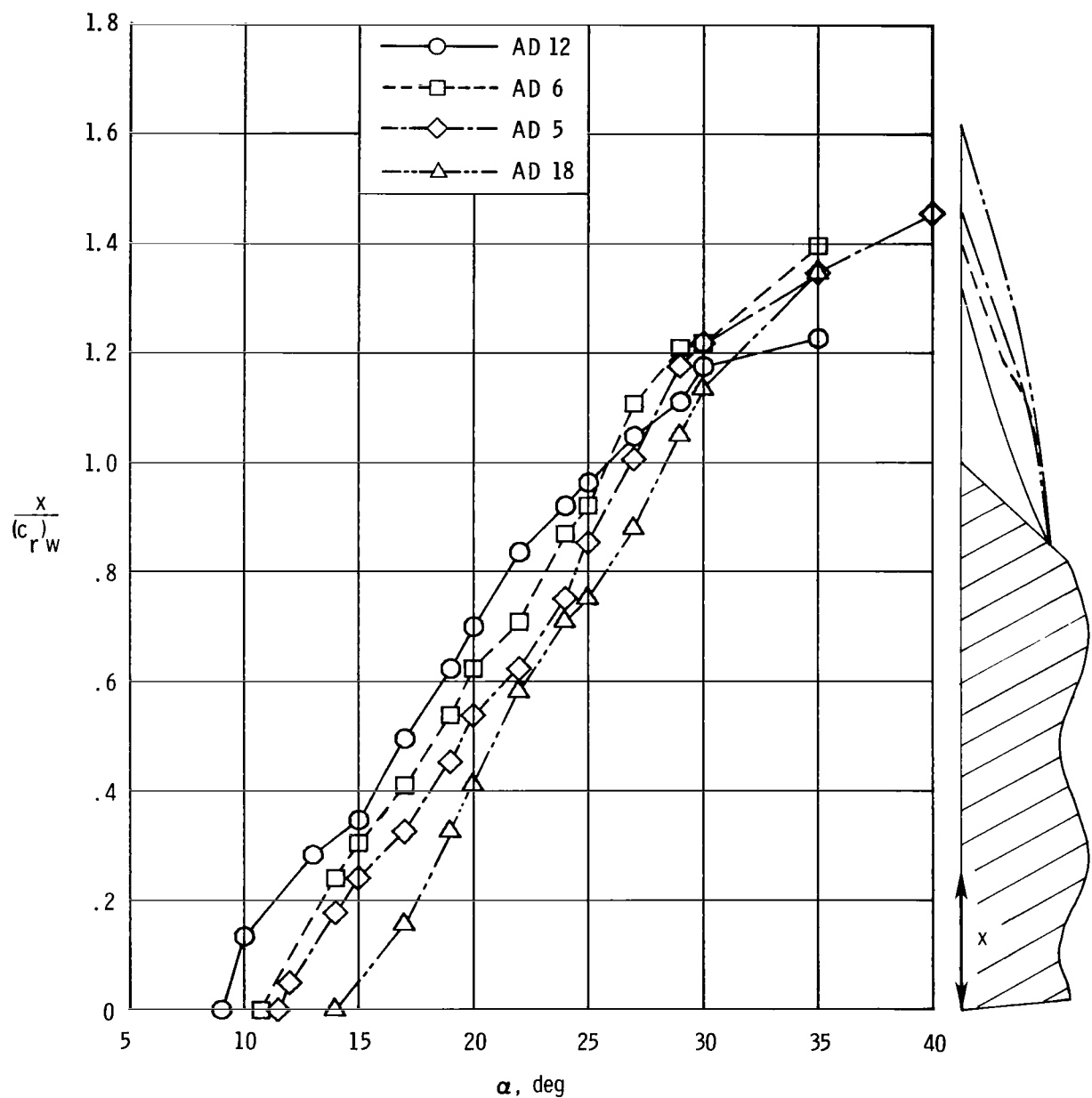
Figure 9.- Concluded.



L-80-152

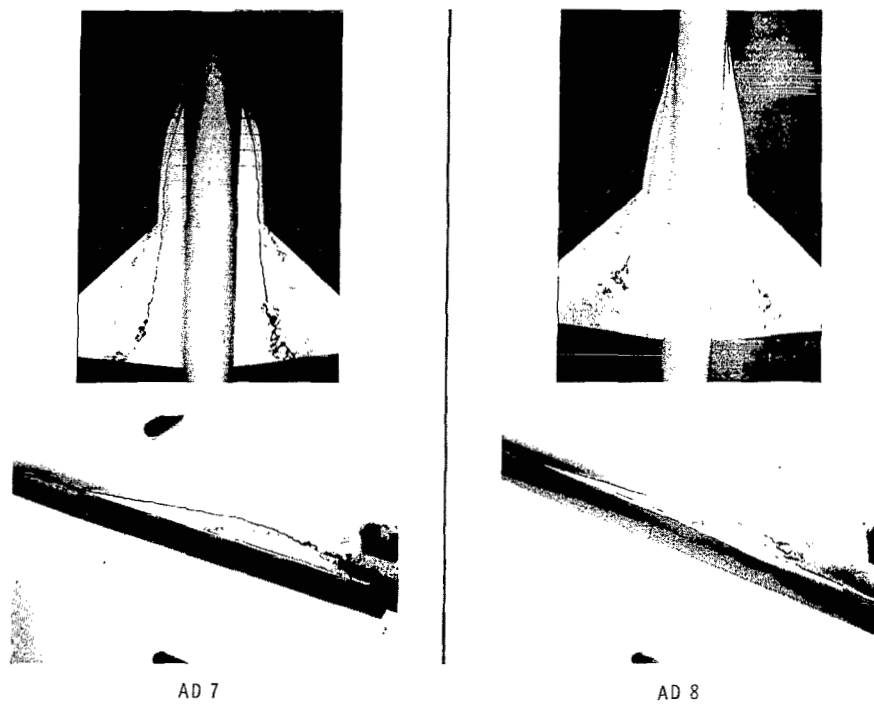
(a) Strake and wing vortex patterns at  $\alpha = 20^\circ$ .

Figure 10.- Water-tunnel photographs and strake vortex breakdown characteristics for strakes analytically designed, group 10.



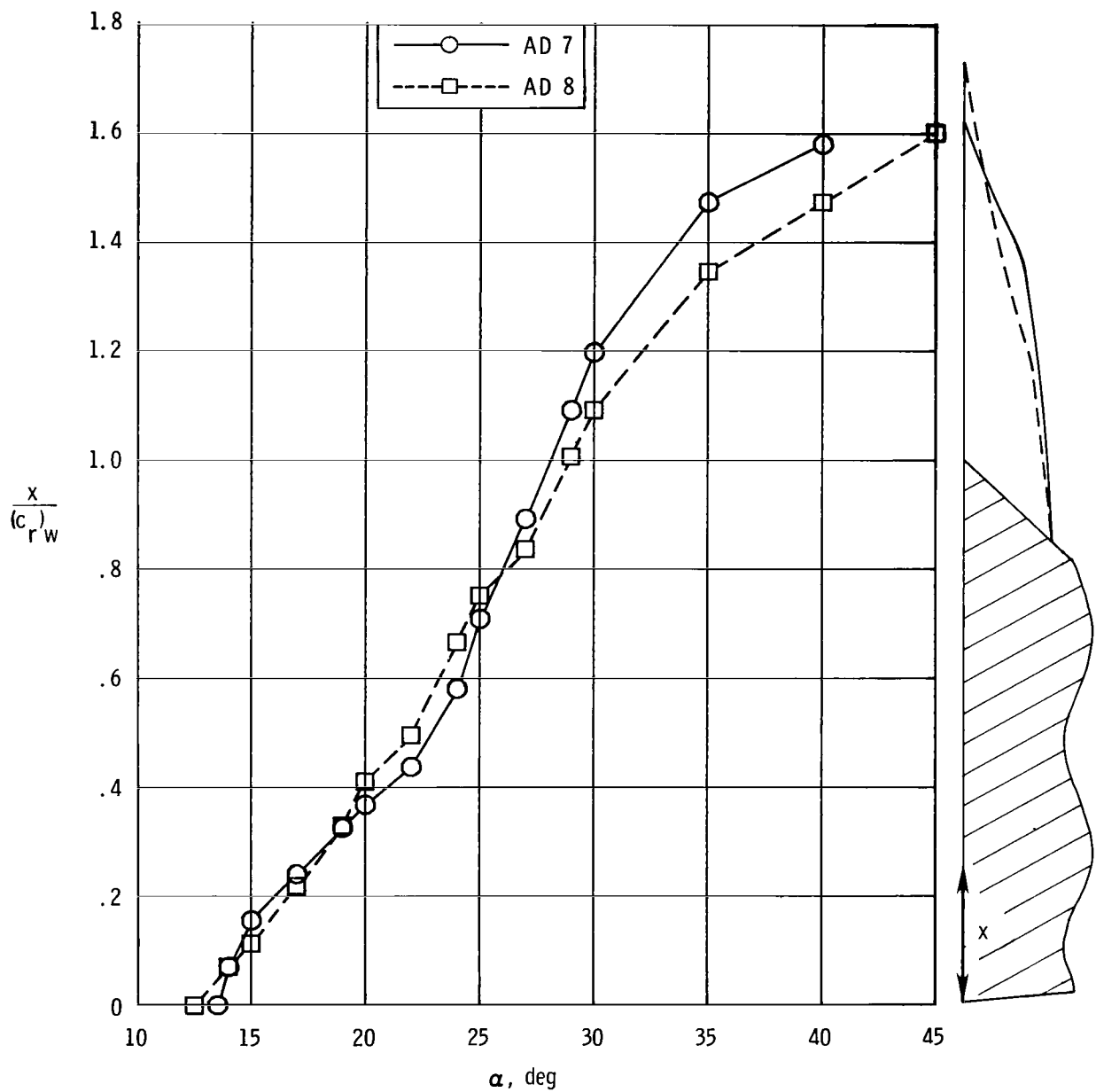
(b) Strake vortex breakdown position.

Figure 10.- Concluded.



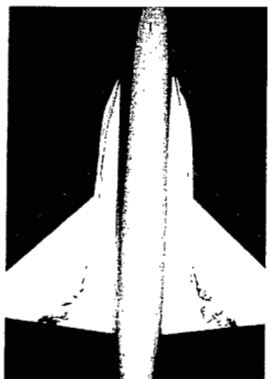
(a) Strake and wing vortex patterns at  $\alpha = 20^\circ$ .

Figure 11.- Water-tunnel photographs and strake vortex breakdown characteristics for strakes analytically designed, group 11.



(b) Strake vortex breakdown position.

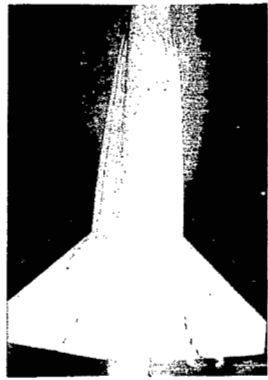
Figure 11.- Concluded.



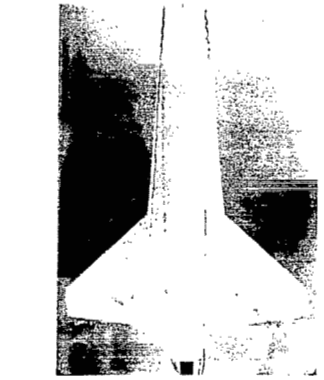
AD 20



AD 10



AD 19

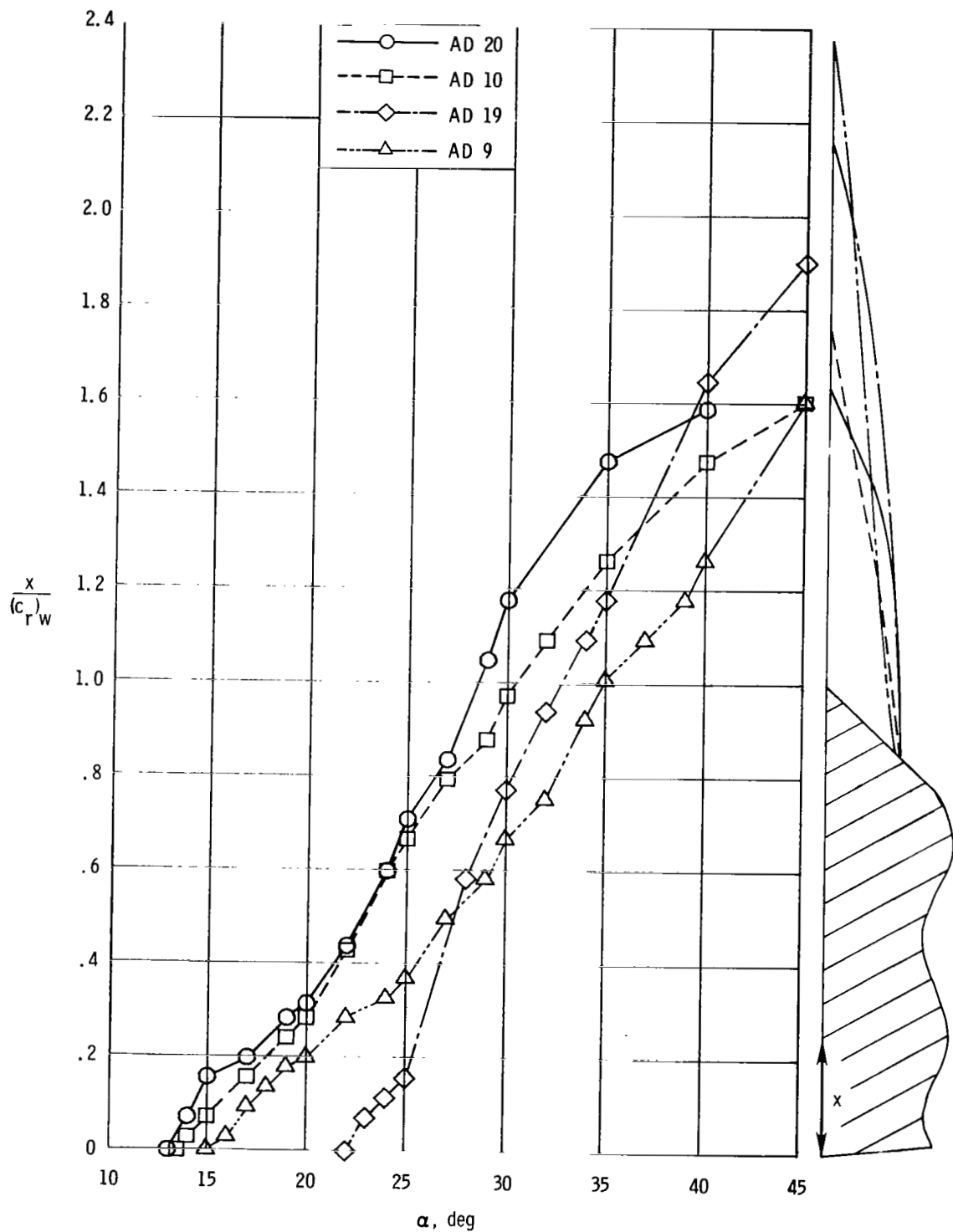


AD 9

L-80-154

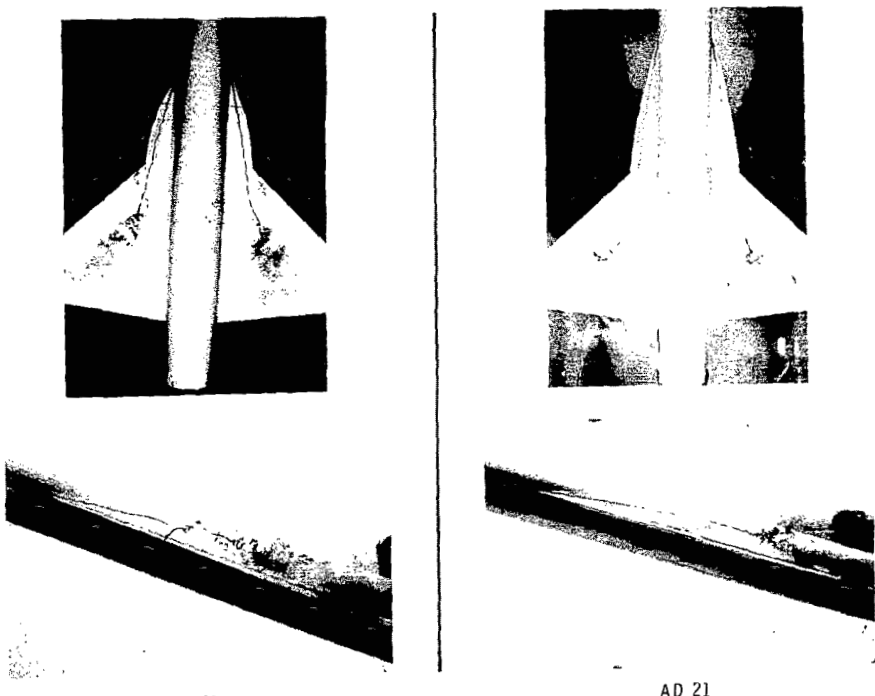
(a) Strake and wing vortex patterns at  $\alpha = 20^\circ$ .

Figure 12.- Water-tunnel photographs and strake vortex breakdown characteristics for strakes analytically designed, group 12.



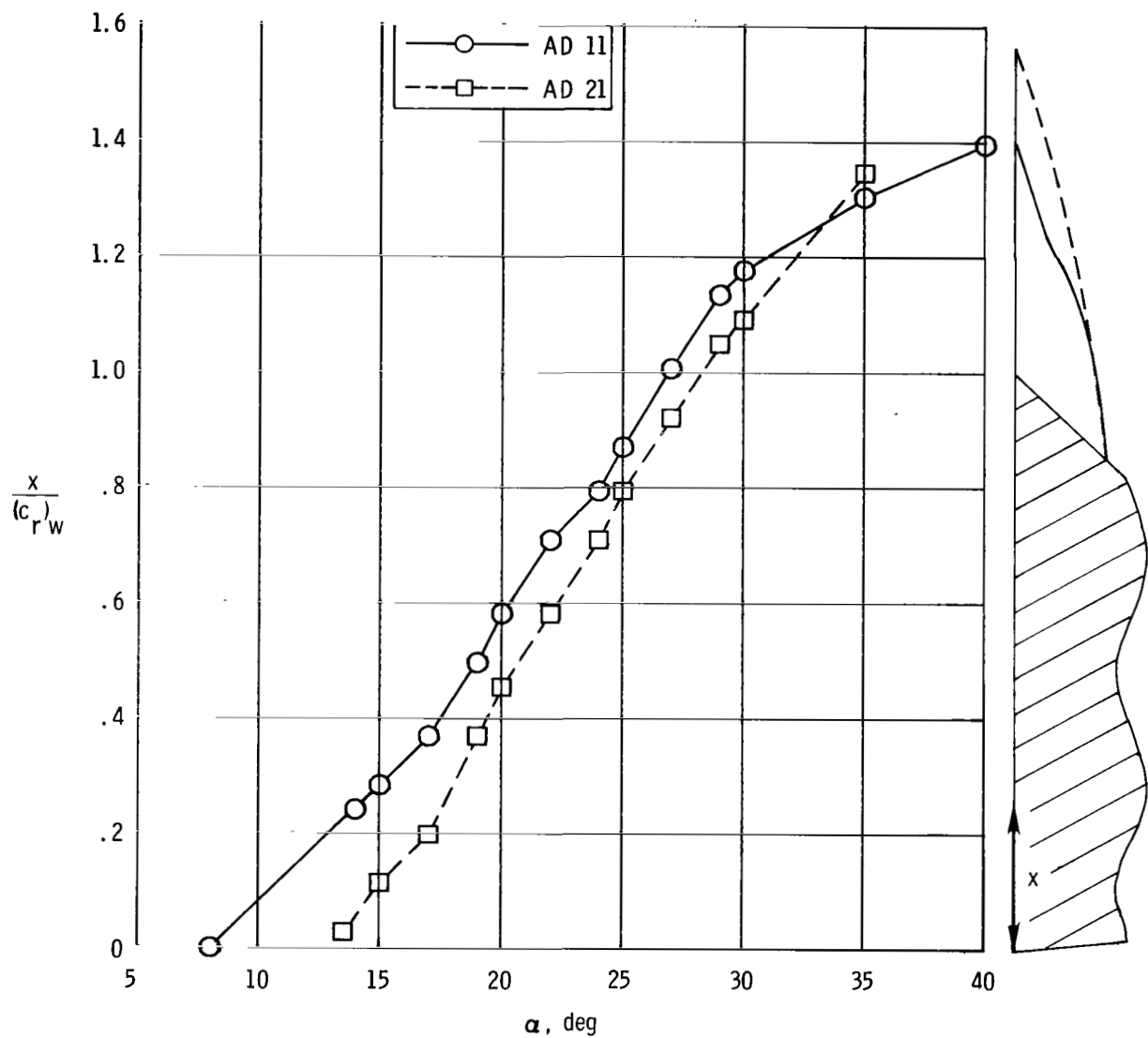
(b) Strake vortex breakdown position.

Figure 12.- Concluded.



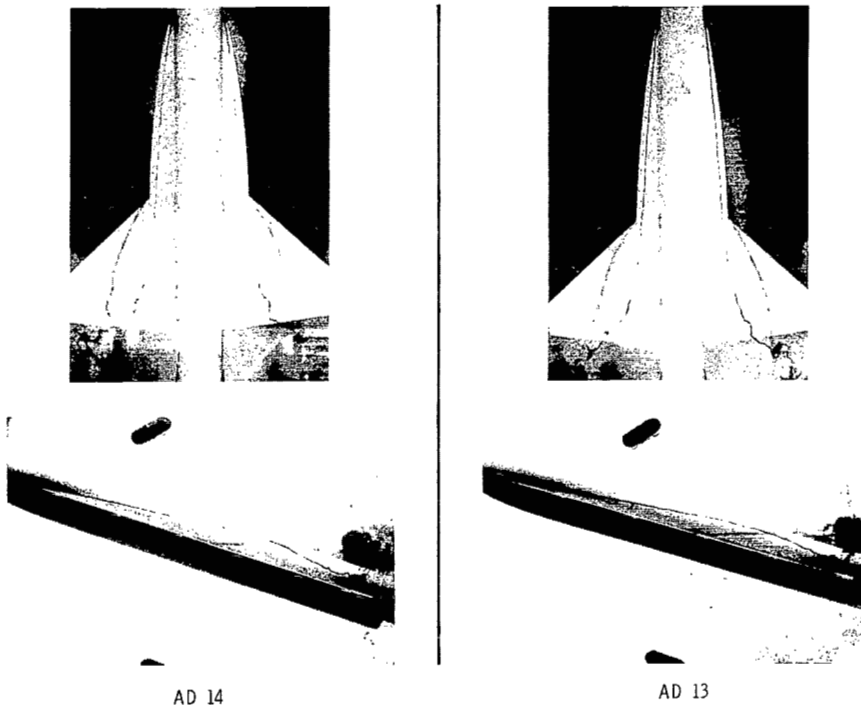
(a) Strake and wing vortex patterns at  $\alpha = 20^\circ$ .

Figure 13.- Water-tunnel photographs and strake vortex breakdown characteristics for strakes analytically designed, group 13.



(b) Strake vortex breakdown position.

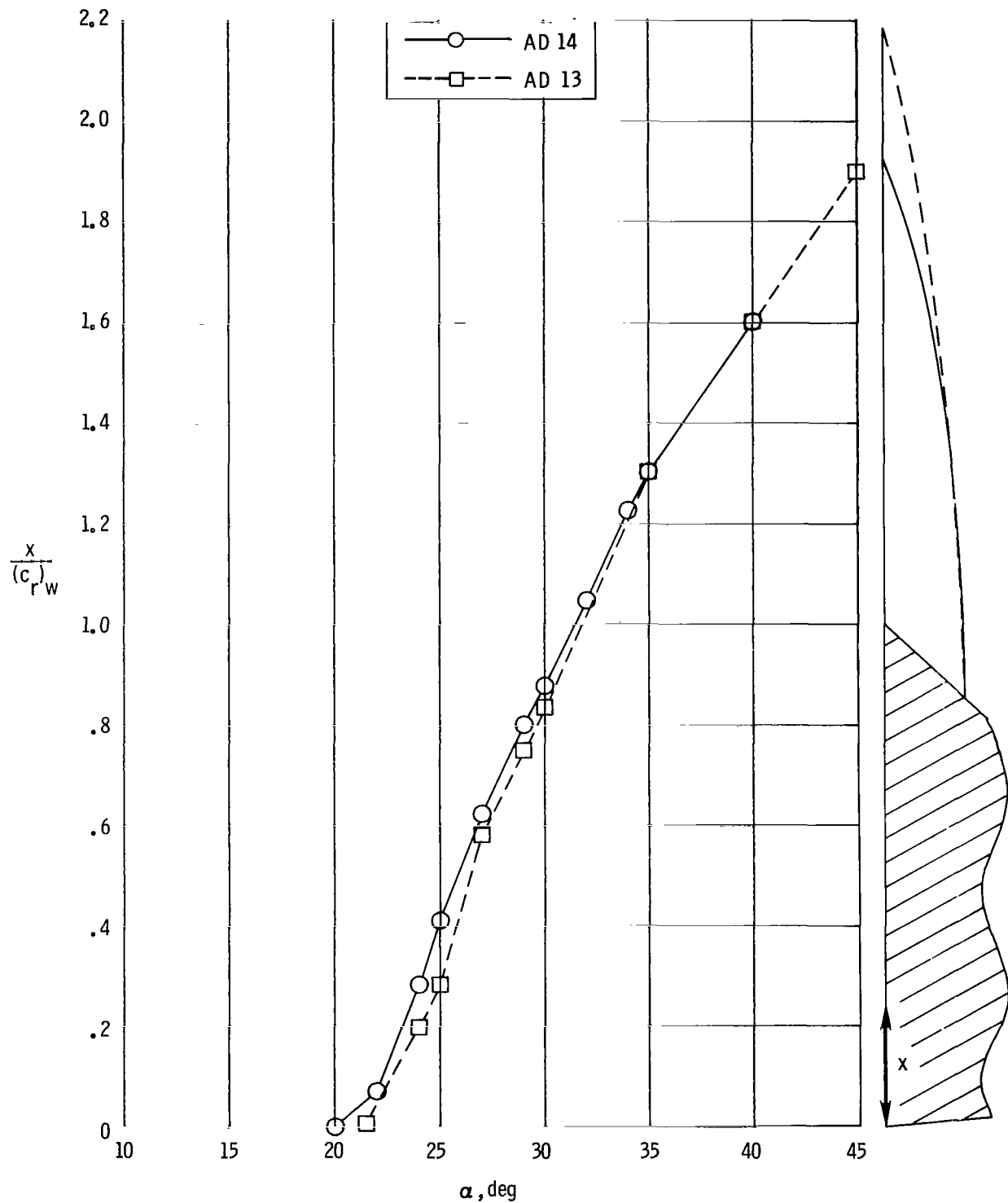
Figure 13.- Concluded.



L-80-156

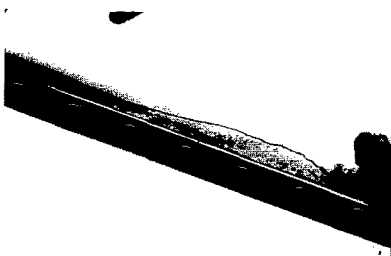
(a) Strake and wing vortex patterns at  $\alpha = 20^\circ$ .

Figure 14.- Water-tunnel photographs and strake vortex breakdown characteristics for strakes analytically designed, group 3.

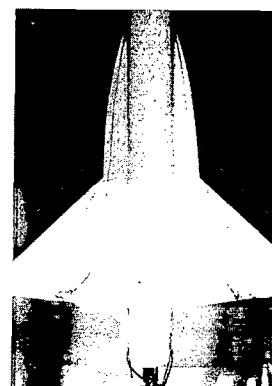


(b) Strake vortex breakdown position.

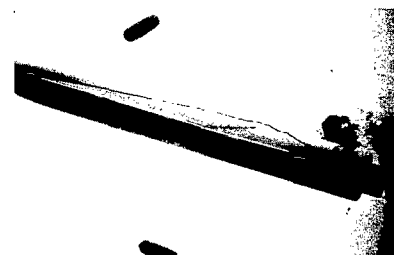
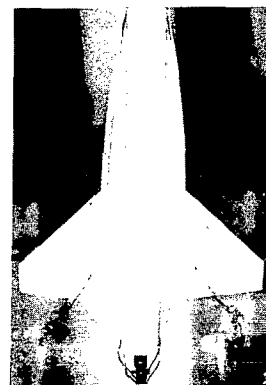
Figure 14.- Concluded.



AD 16



AD 15

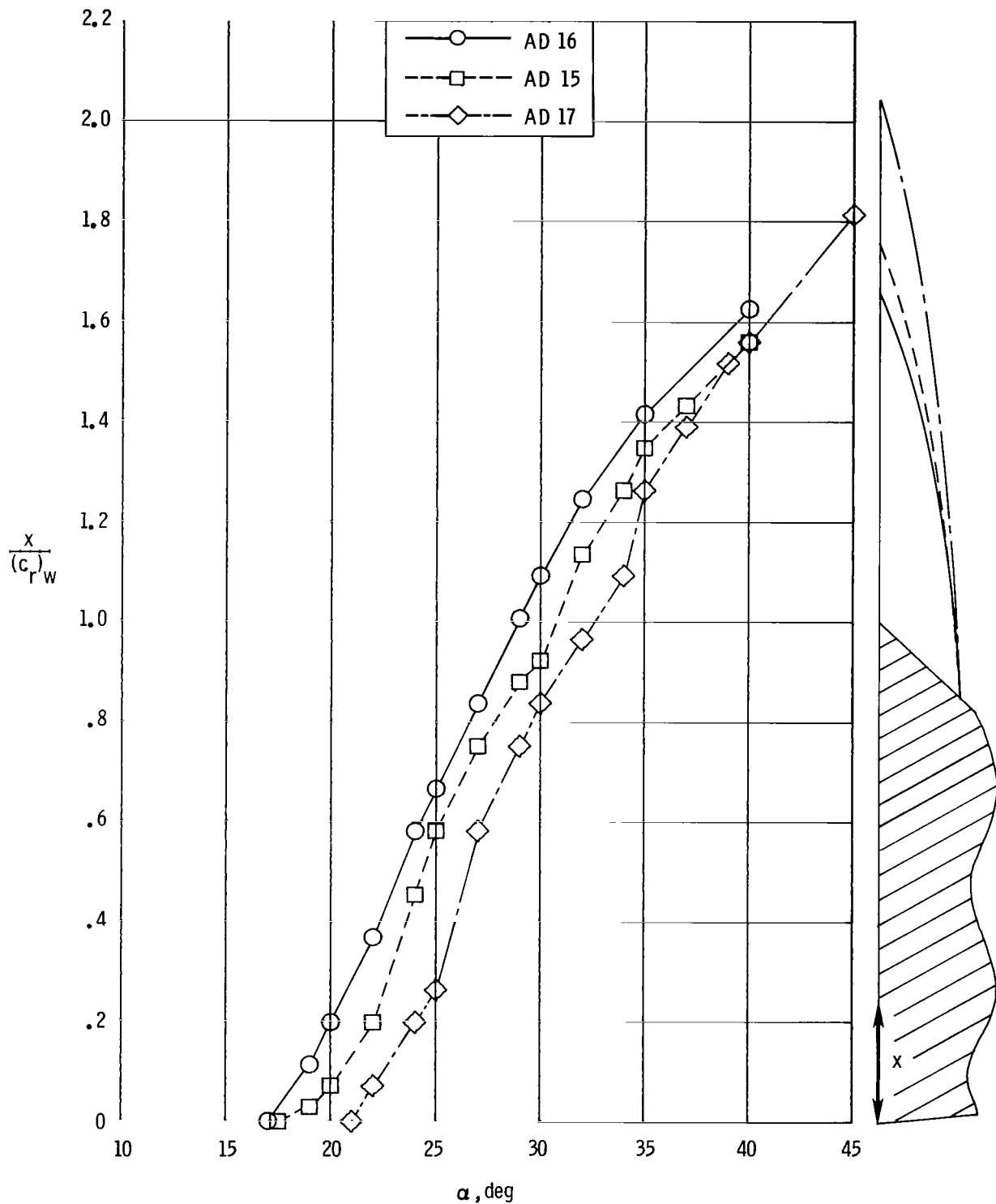


AD 17

L-80-157

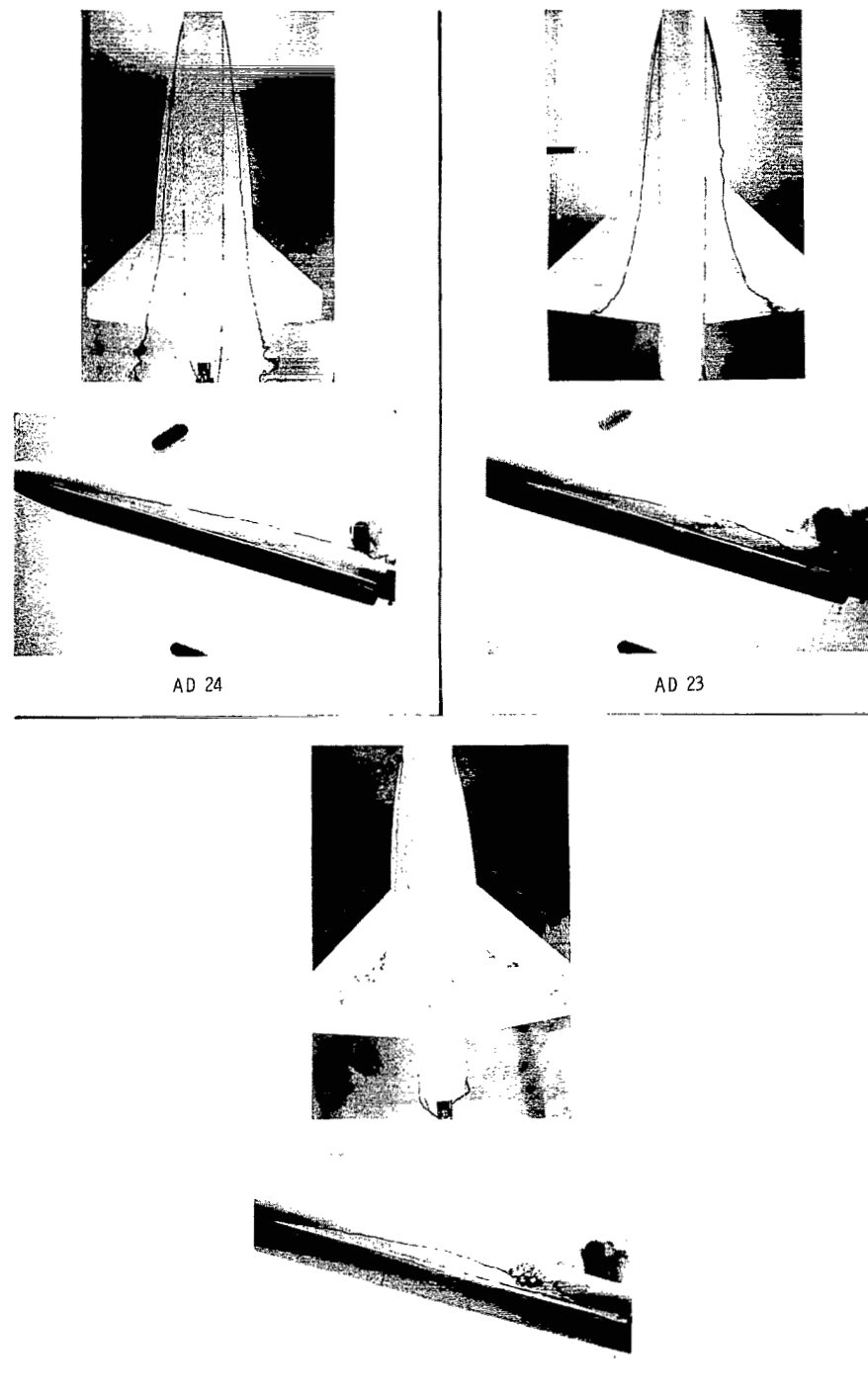
(a) Strake and wing vortex patterns at  $\alpha = 20^\circ$ .

Figure 15.- Water-tunnel photographs and strake vortex breakdown characteristics for strakes analytically designed, groups 4, 5, and 6.



(b) Strake vortex breakdown position.

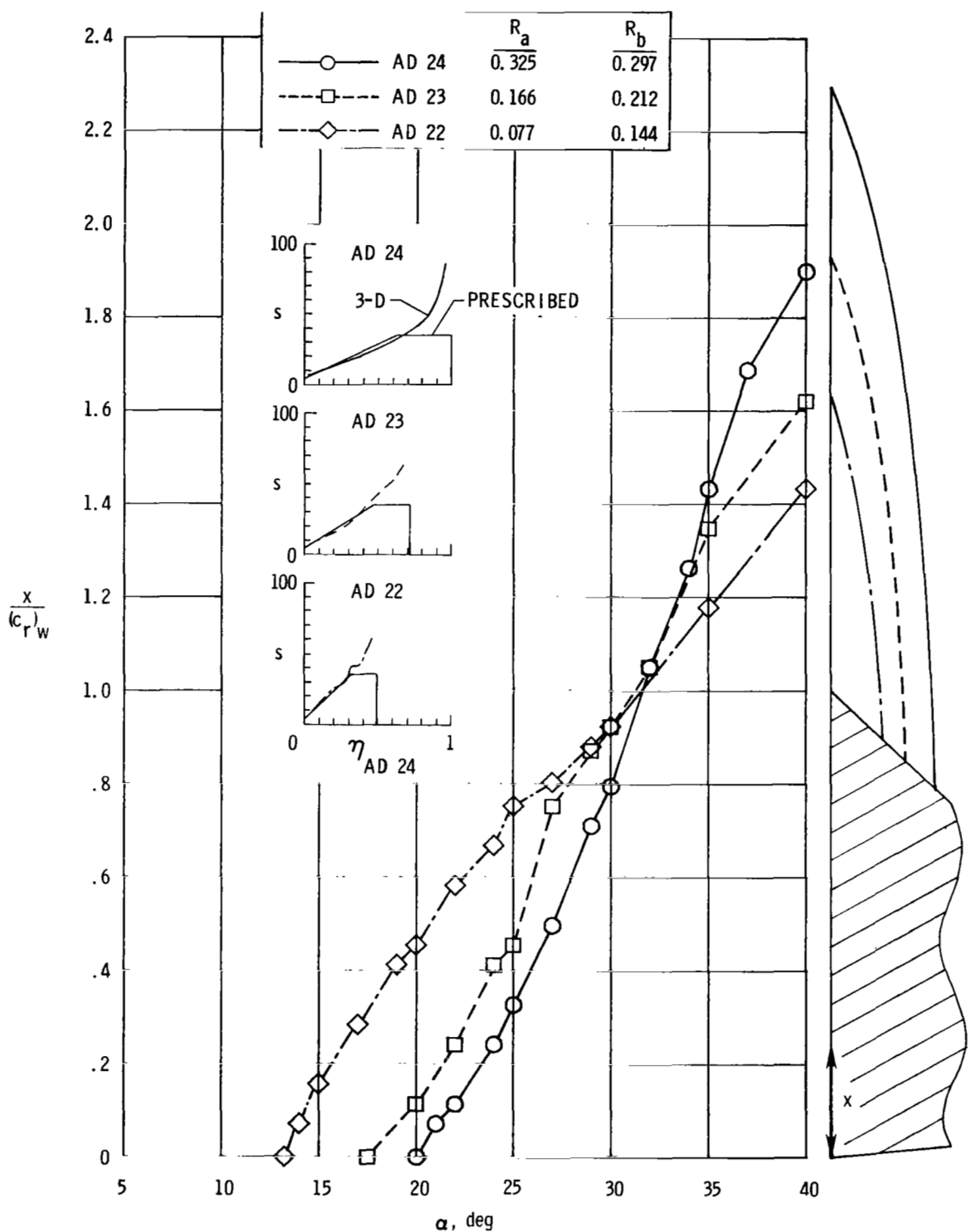
Figure 15.- Concluded.



(a) Strake and wing vortex patterns at  $\alpha = 20^\circ$ .

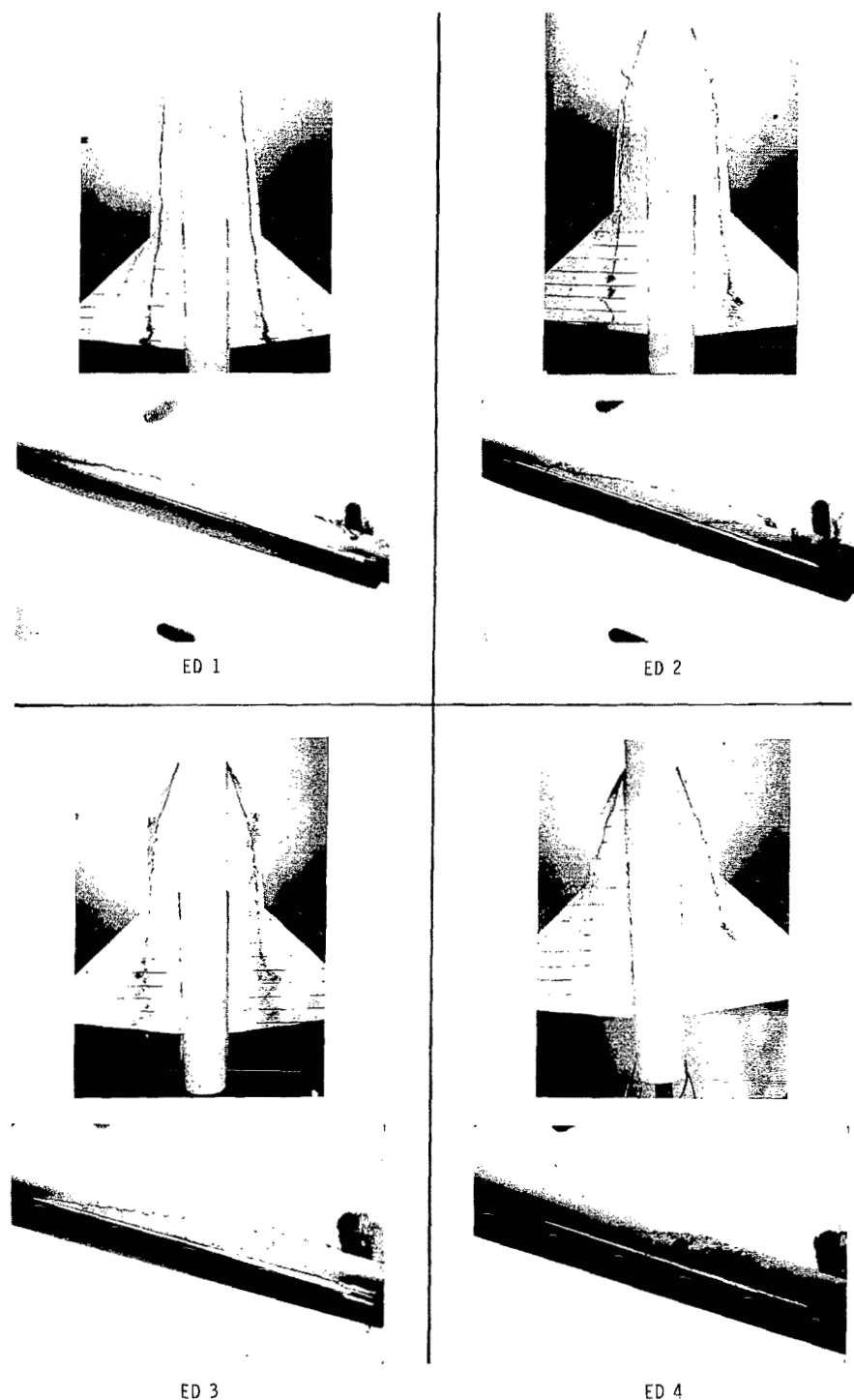
L-80-158

Figure 16.- Water-tunnel photographs and strake vortex breakdown characteristics of area scaled strakes, based on original suction distribution.



(b) Strake vortex breakdown position and suction distribution.

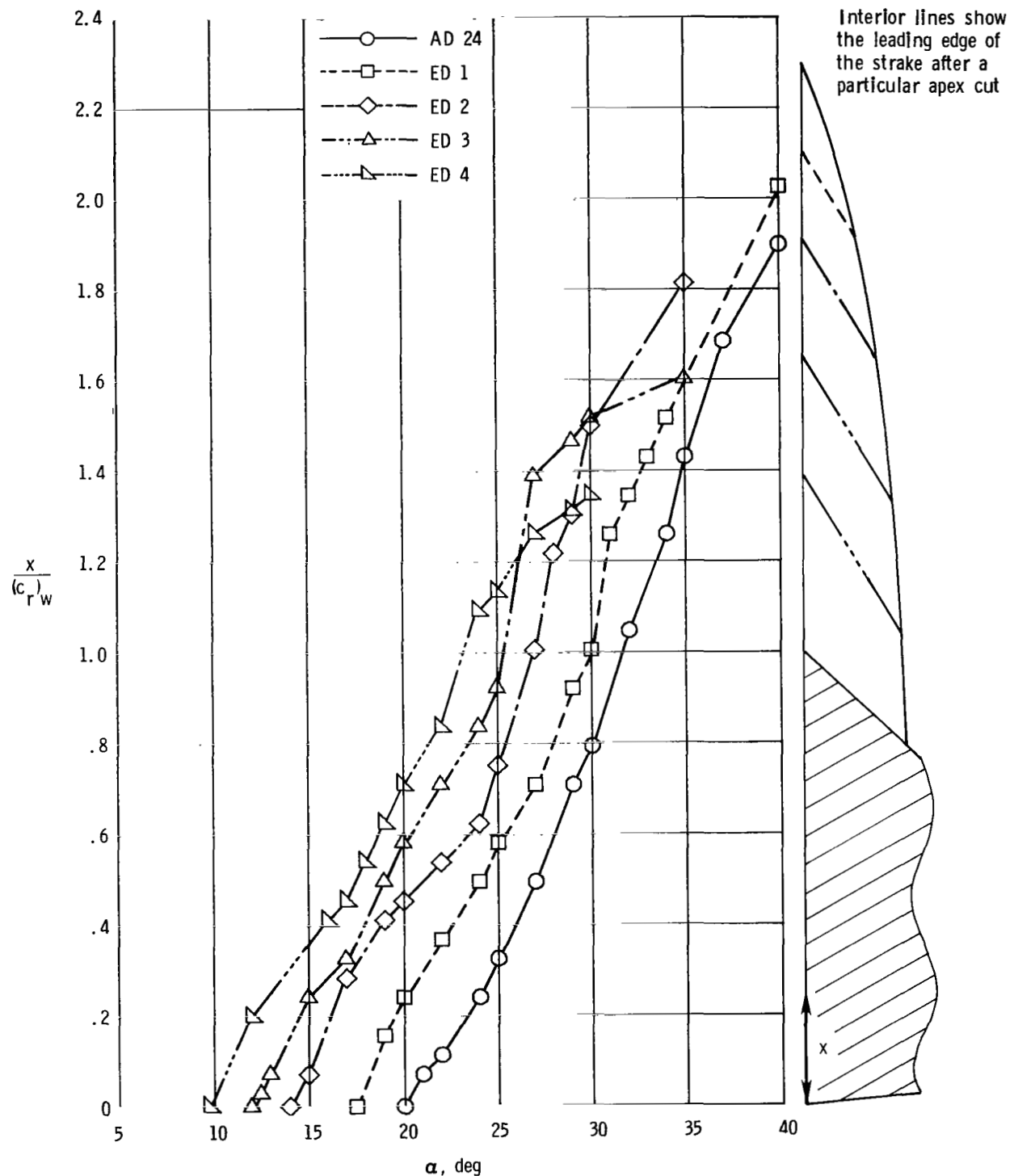
Figure 16.- Concluded.



L-80-159

(a) Strake and wing vortex patterns at  $\alpha = 20^\circ$ .

Figure 17.- Water-tunnel photographs and strake vortex breakdown characteristics of apex-cut strakes.

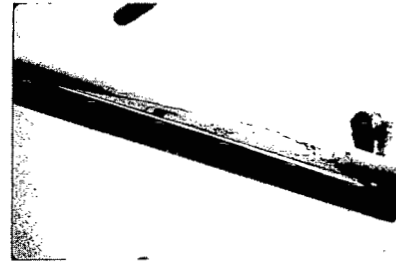


(b) Strake vortex breakdown position.

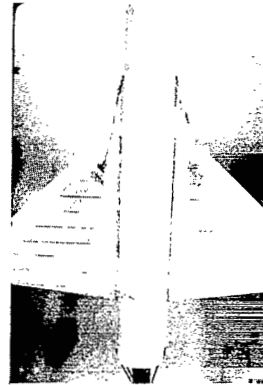
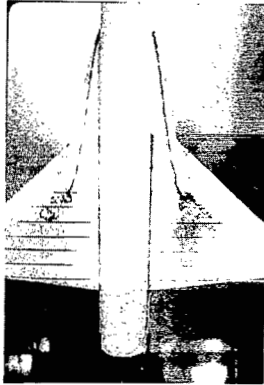
Figure 17.- Concluded.



ED 5



ED 6



ED 7

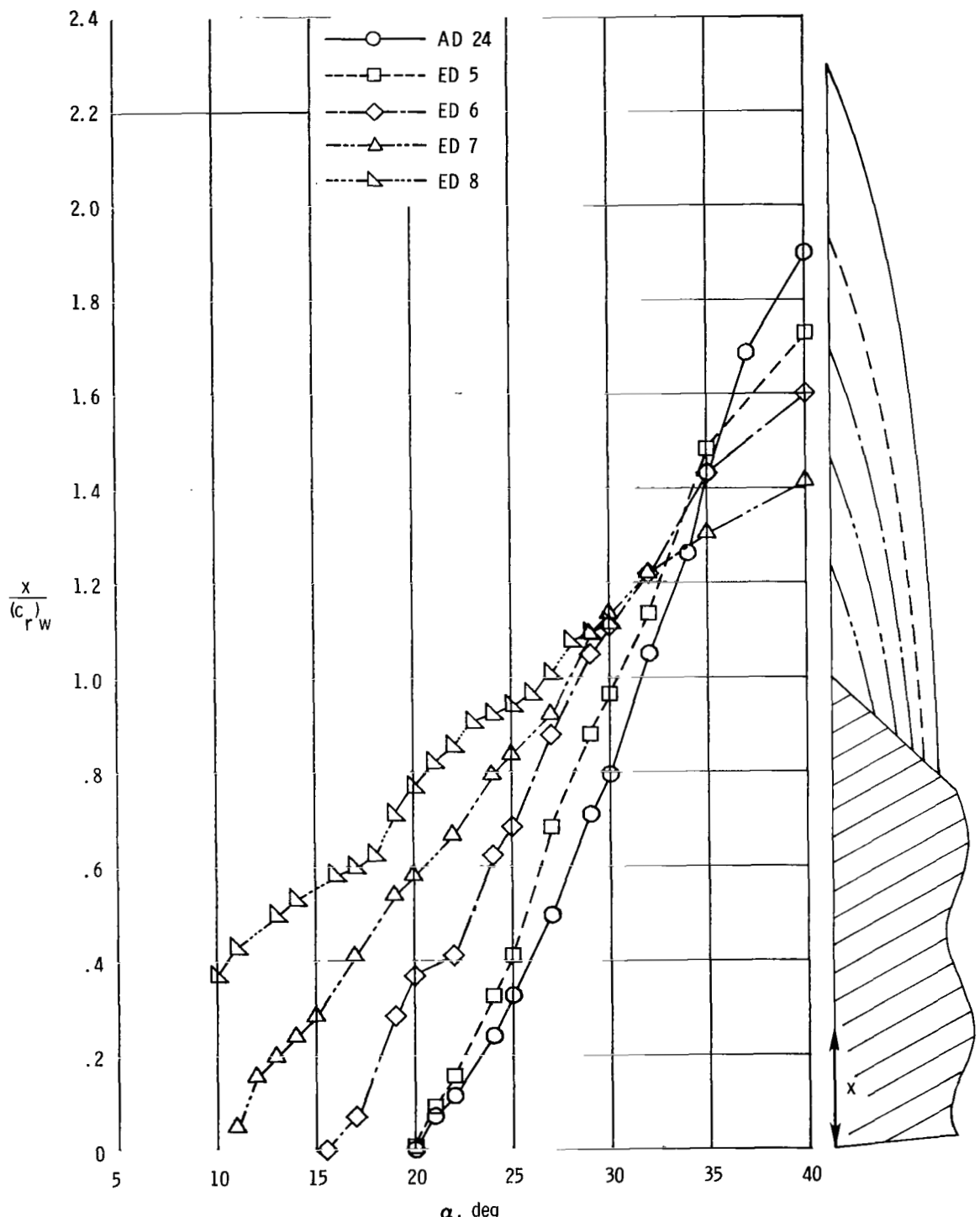


ED 8

L-80-160

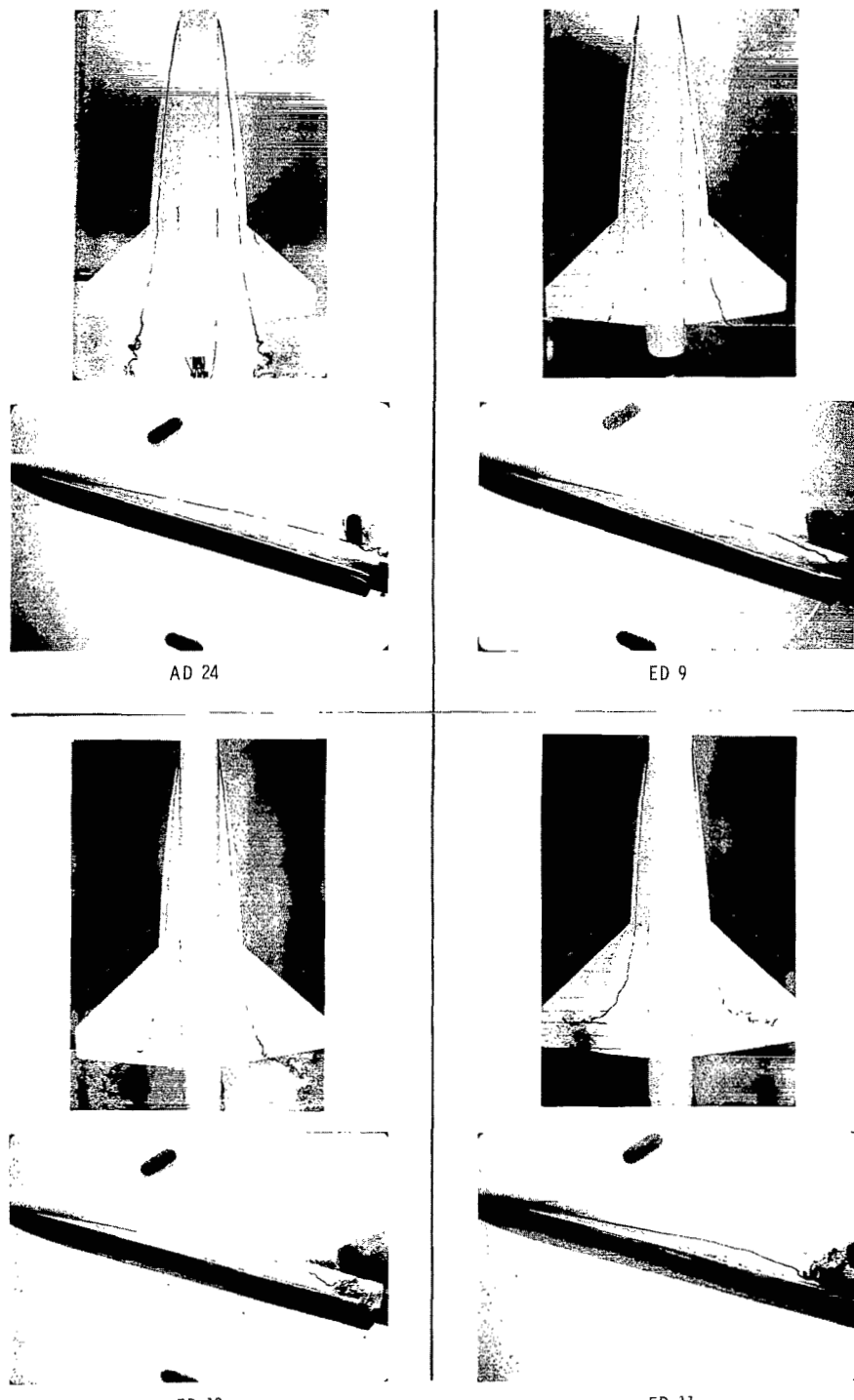
(a) Strake and wing vortex patterns at  $\alpha = 20^\circ$ .

Figure 18.- Water-tunnel photographs and strake vortex breakdown characteristics of trailing-edge cut strakes.



(b) Strake vortex breakdown position.

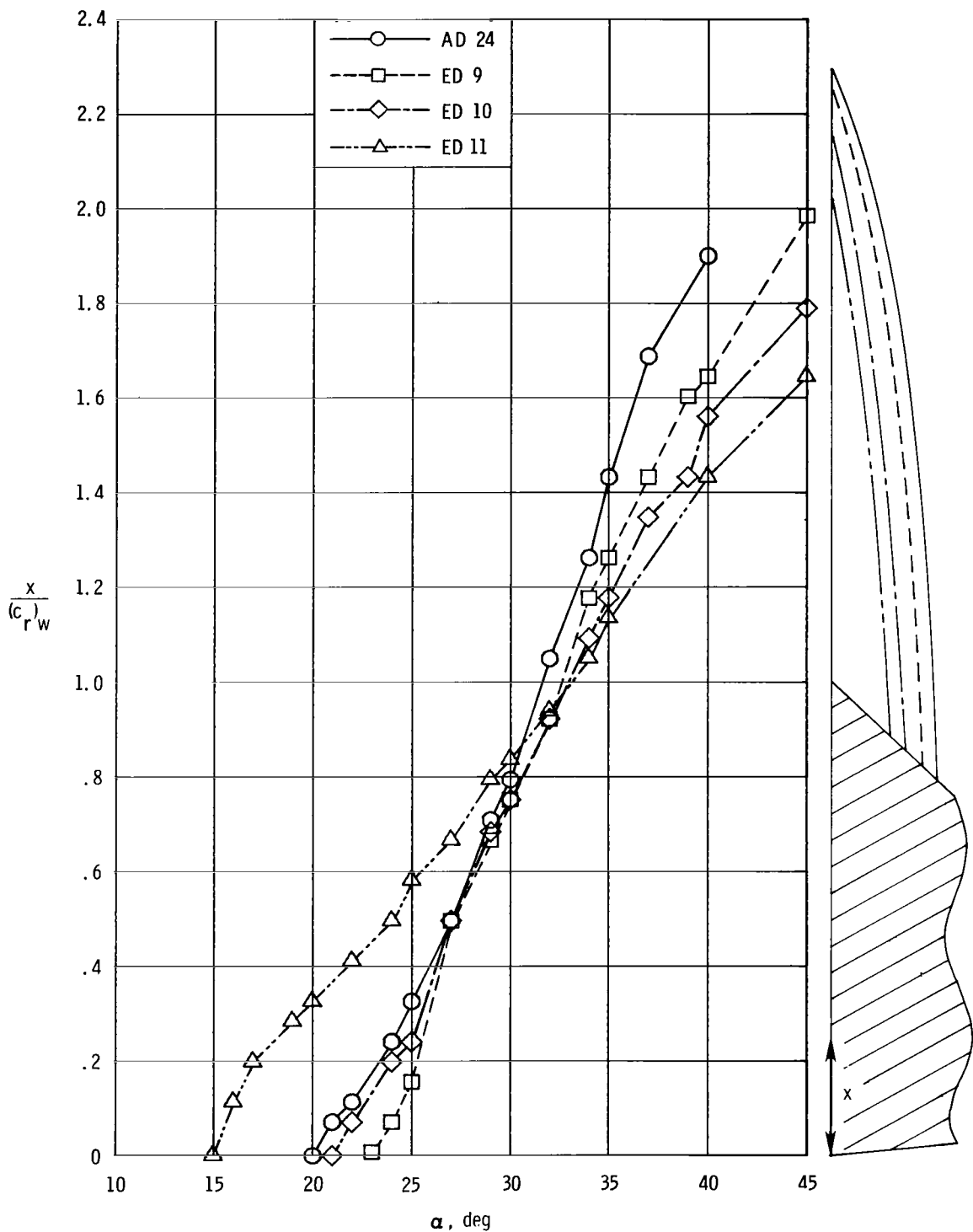
Figure 18.- Concluded.



L-80-161

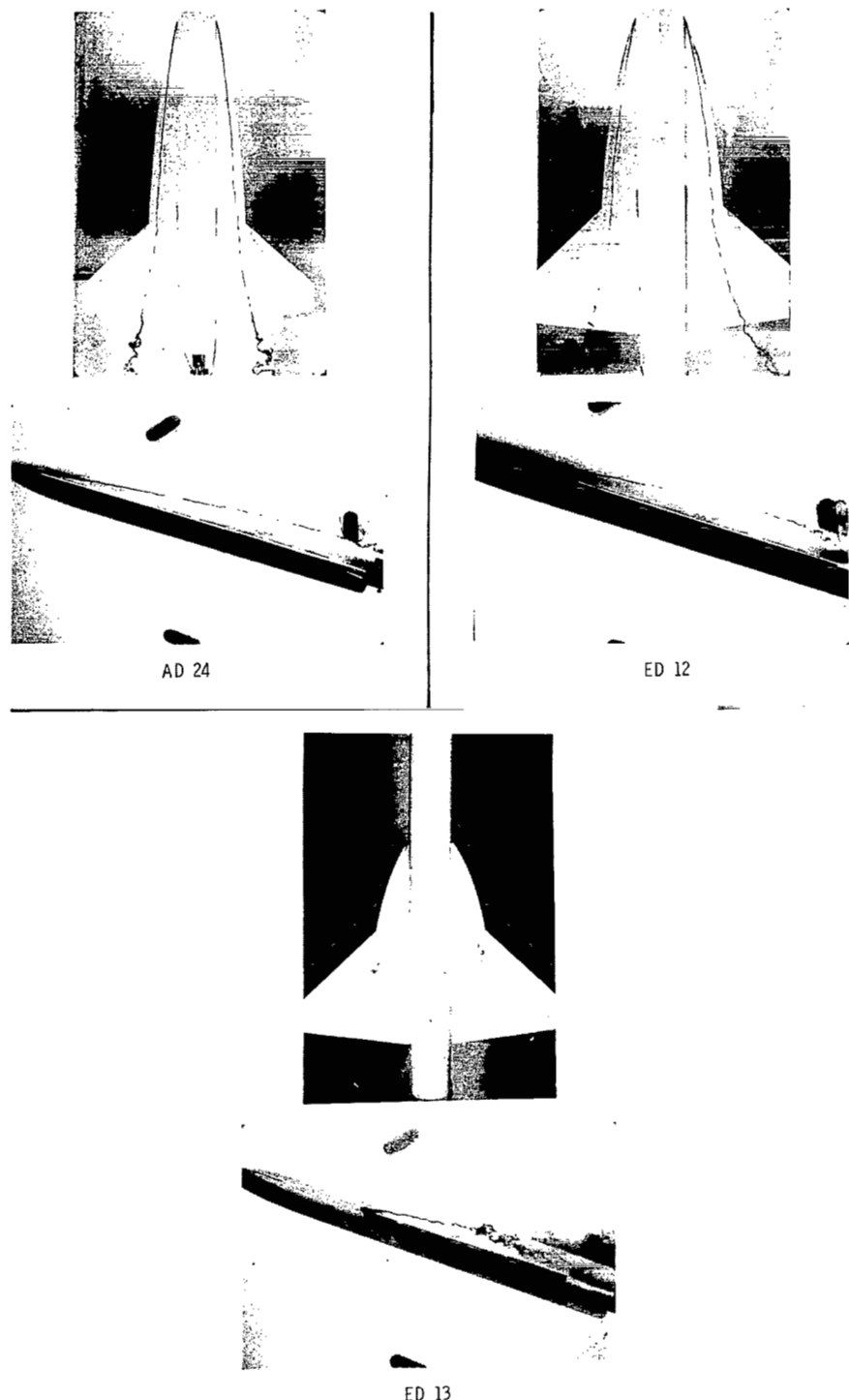
(a) Strake and wing vortex patterns at  $\alpha = 20^\circ$ .

Figure 19.- Water-tunnel photographs and strake vortex breakdown characteristics of spanwise cut strakes.



(b) Strake vortex breakdown position.

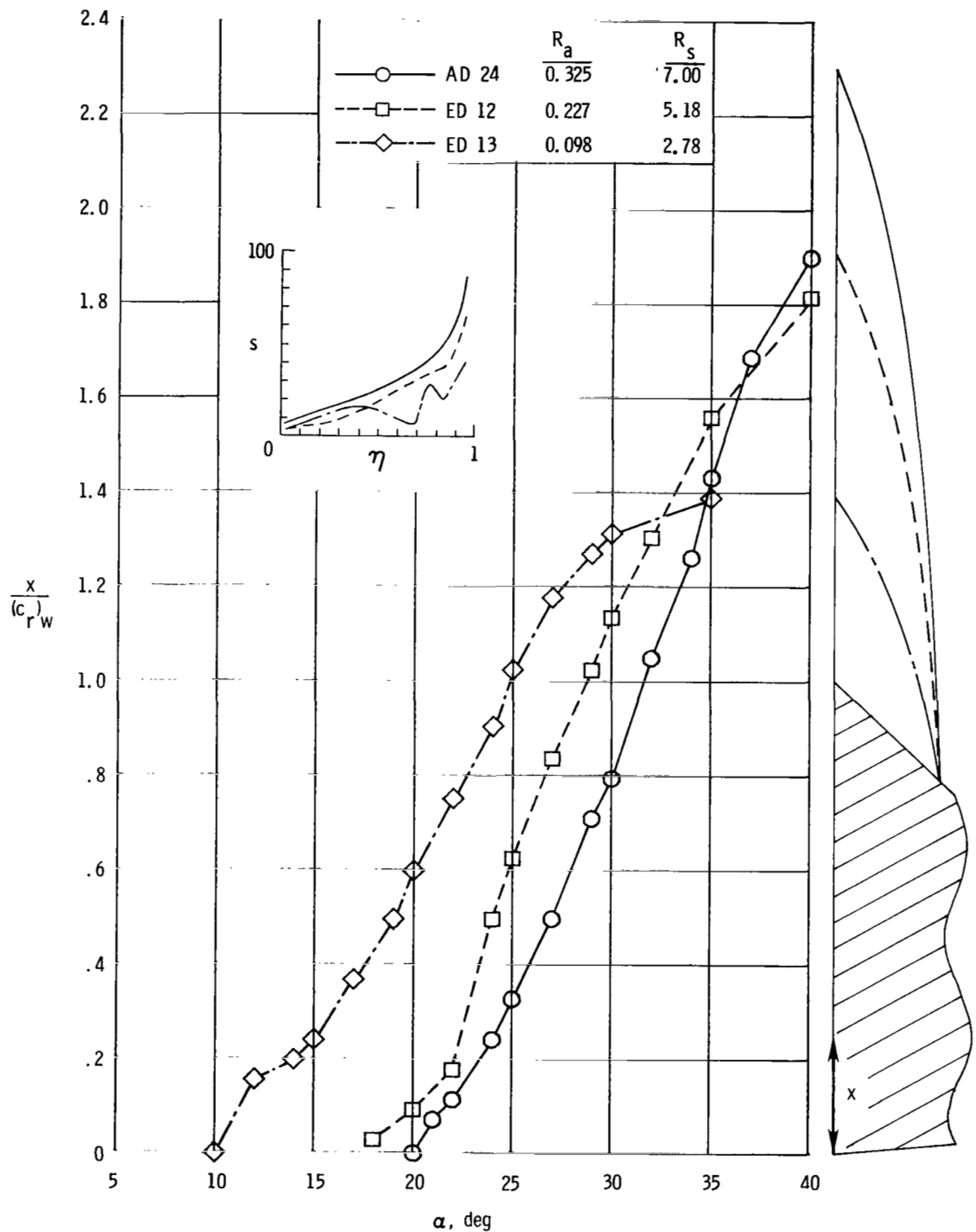
Figure 19.- Concluded.



L-80-162

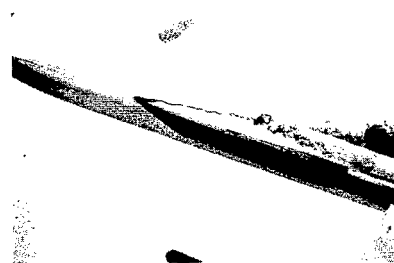
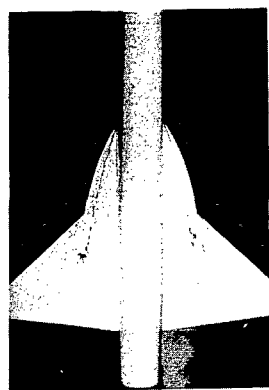
(a) Strake and wing vortex patterns at  $\alpha = 20^\circ$ .

Figure 20.- Water-tunnel photographs and strake vortex breakdown characteristics of chordwise scaled strakes.

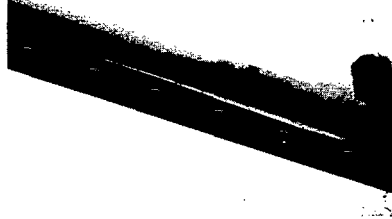
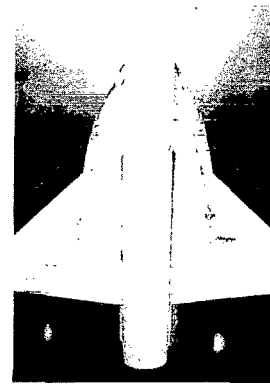
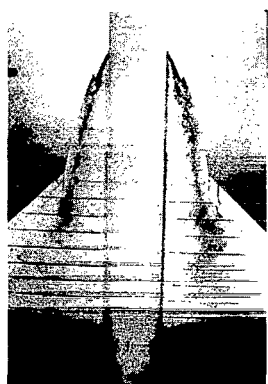


(b) Strake vortex breakdown position and suction distribution.

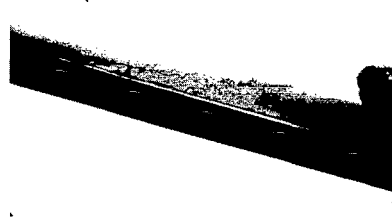
Figure 20.- Concluded.



ED 13



ED 14

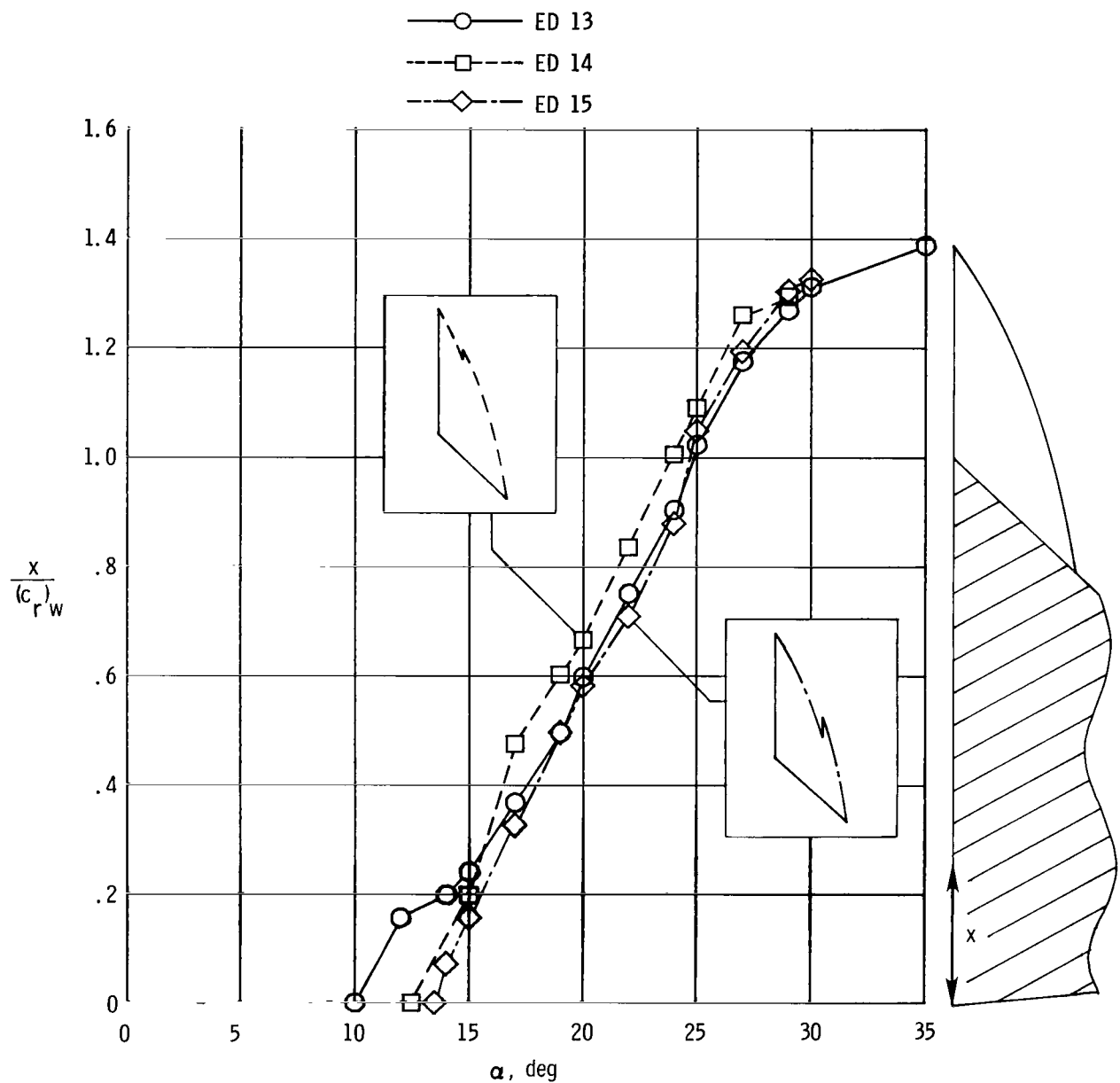


ED 15

L-80-163

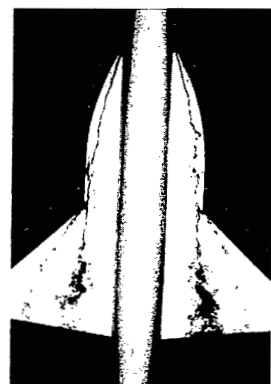
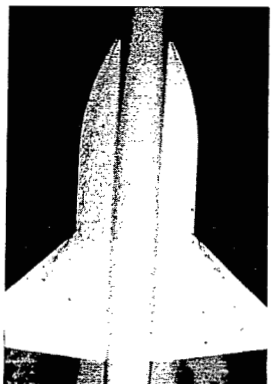
(a) Strake and wing vortex patterns at  $\alpha = 20^\circ$ .

Figure 21.- Water-tunnel photographs and strake vortex breakdown characteristics for snagged strakes.



(b) Strake vortex breakdown position.

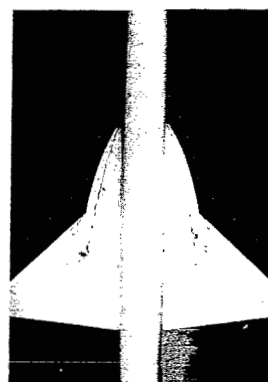
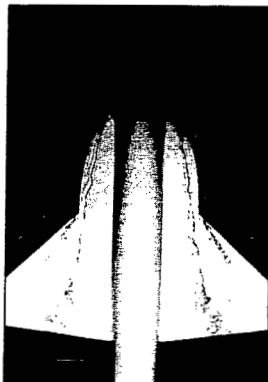
Figure 21.- Concluded.



ED 16



ED 17



ED 18

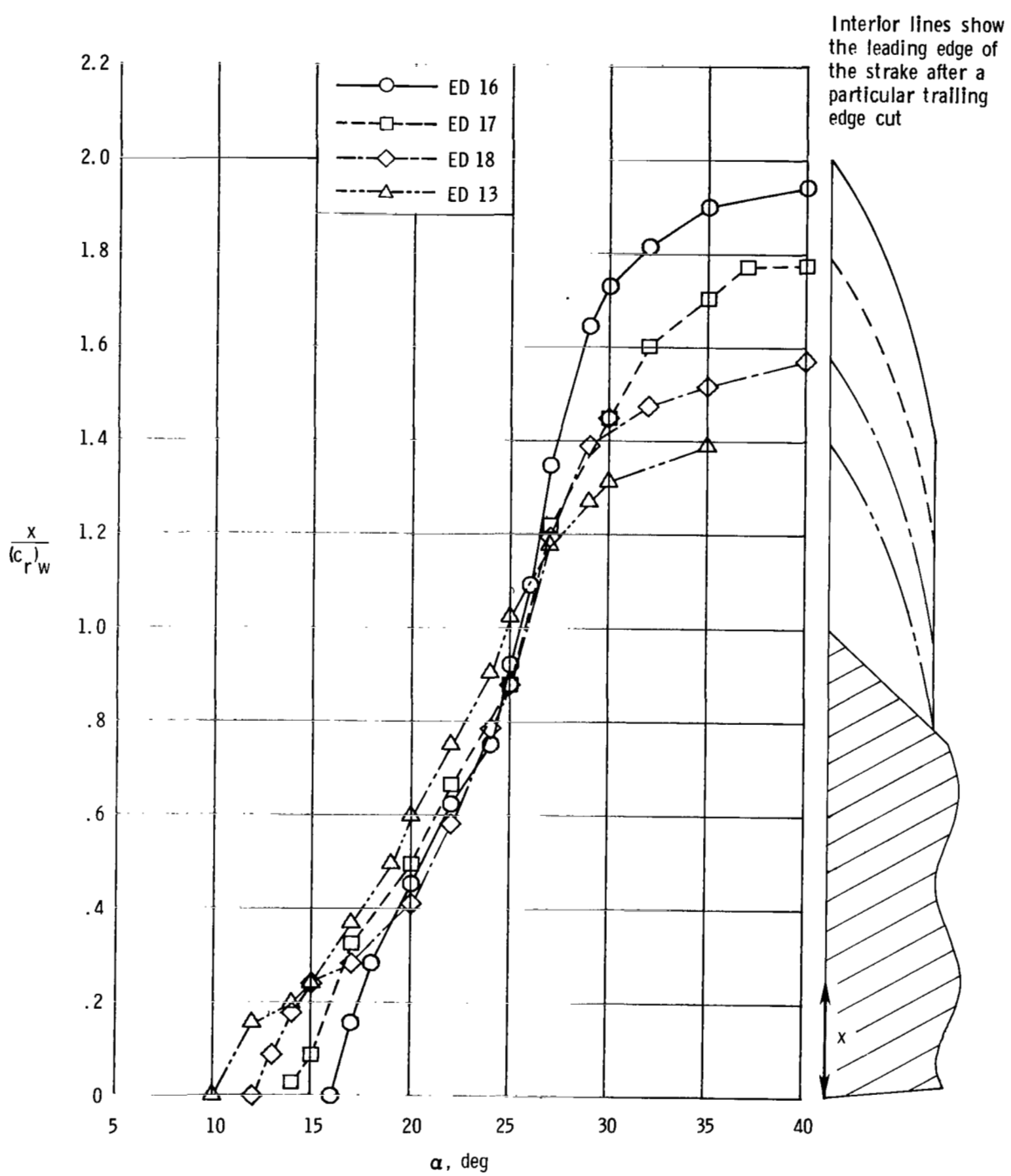


ED 13

L-80-164

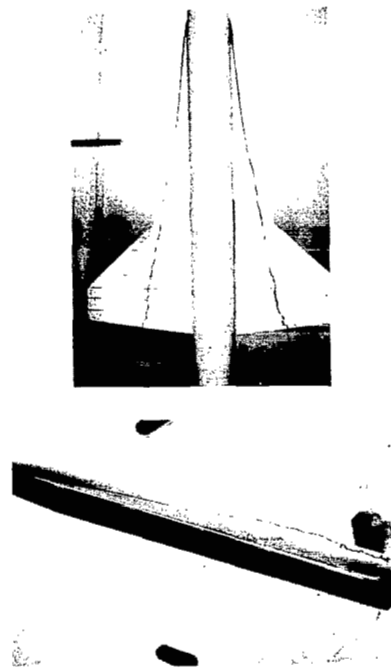
(a) Strake and wing vortex patterns at  $\alpha = 20^\circ$ .

Figure 22.- Water-tunnel photographs and strake vortex breakdown characteristics for side-edge strakes.



(b) Strake vortex breakdown position.

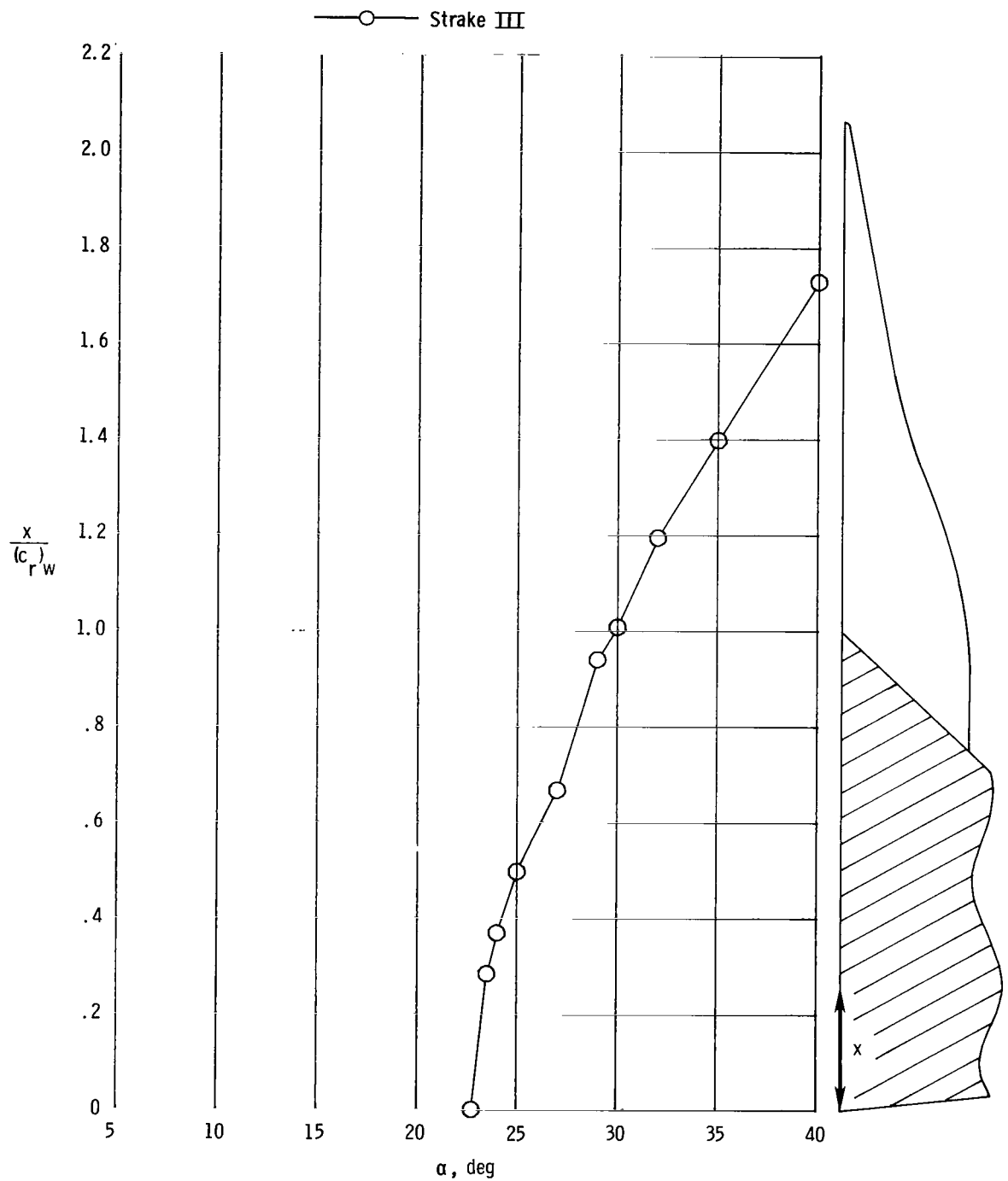
Figure 22.- Concluded.



L-80-165

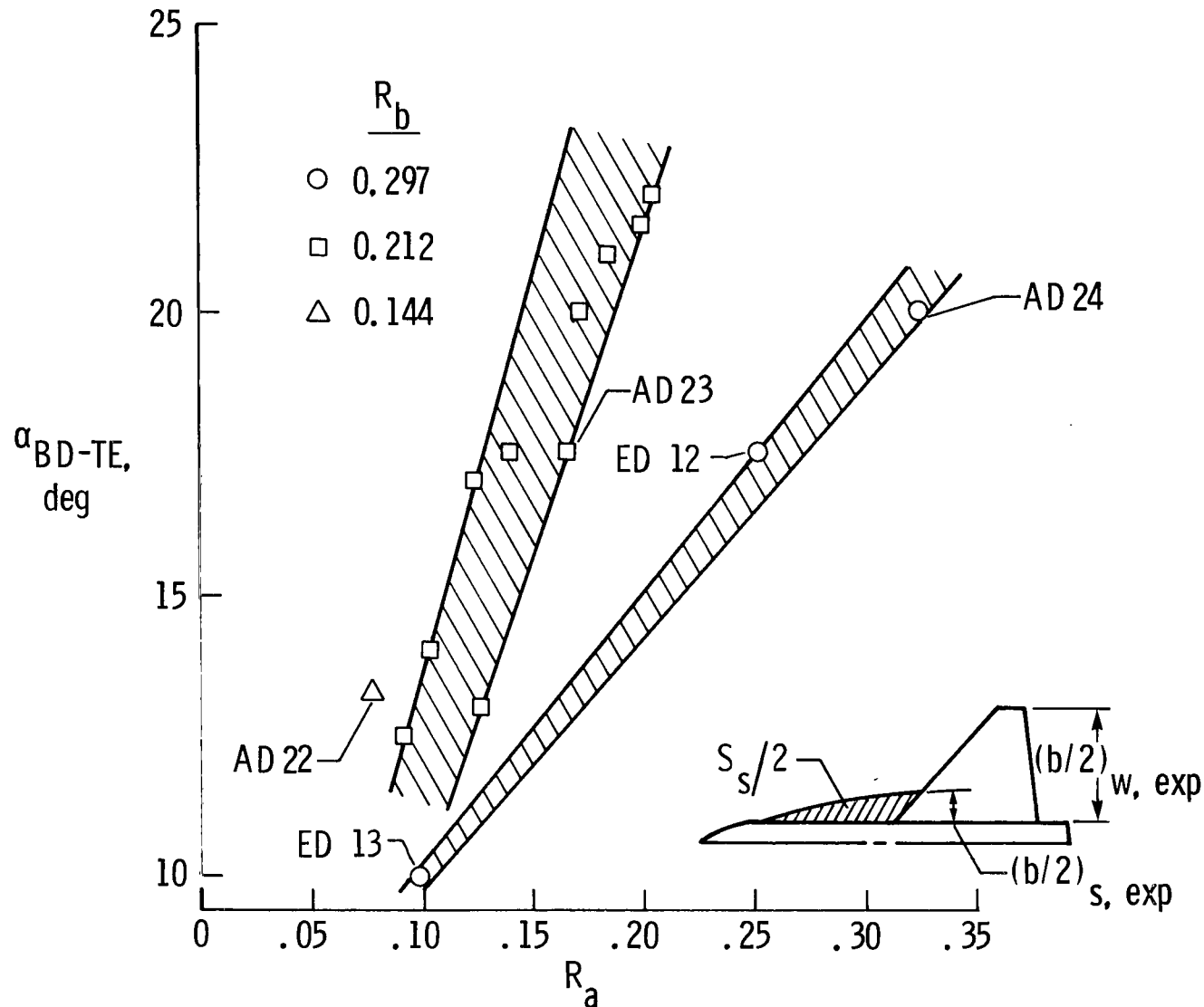
(a) Strake and wing vortex patterns at  $\alpha = 20^\circ$ .

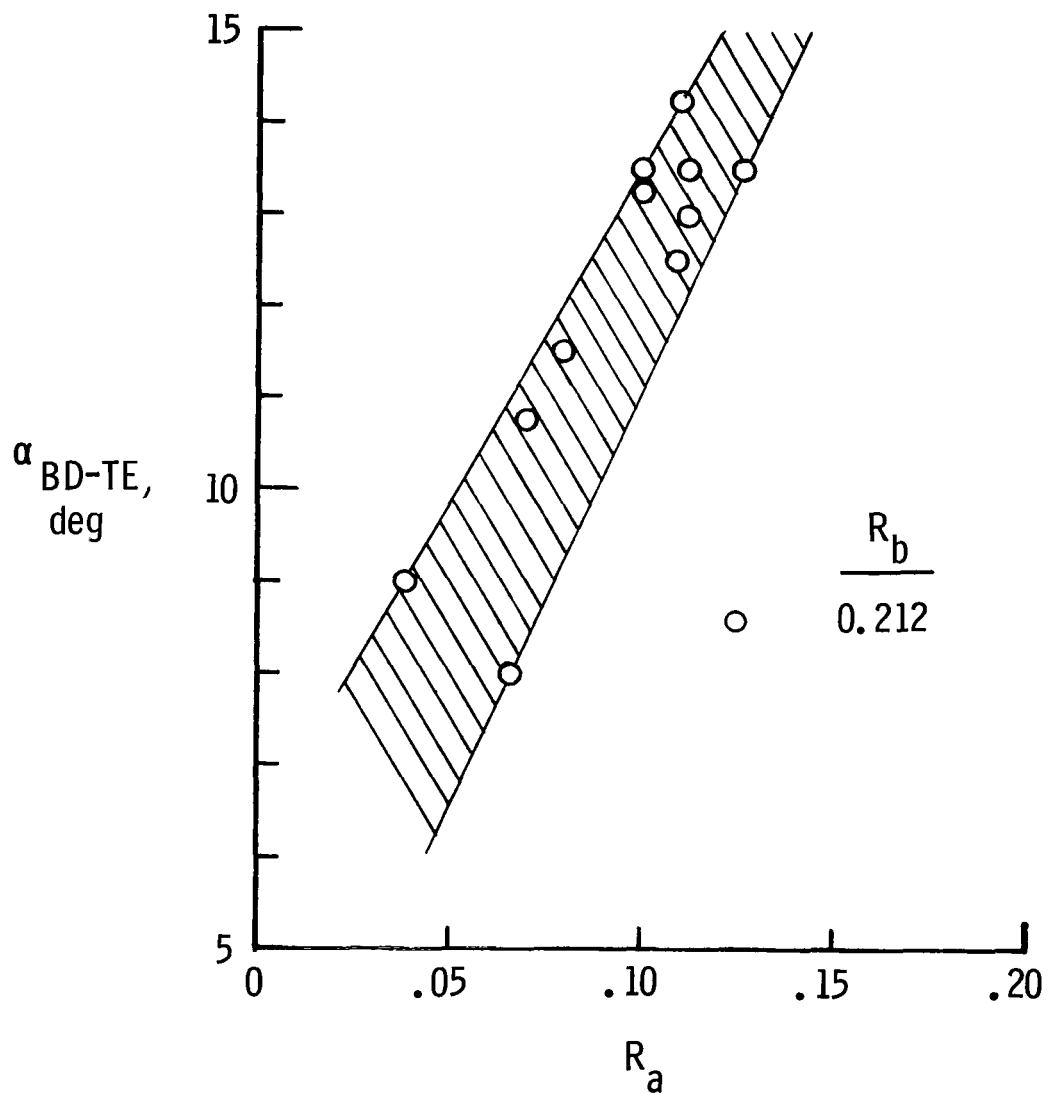
Figure 23.- Water-tunnel photographs and strake vortex breakdown characteristics for Strake III of reference 9.



(b) Strake vortex breakdown position.

Figure 23.- Concluded.

(a)  $R_b$  effect for gothic strakes.Figure 24.- Variation of  $\alpha_{BD-TE}$  with  $R_a$ .



(b) Reflexive strakes.

Figure 24.- Concluded.

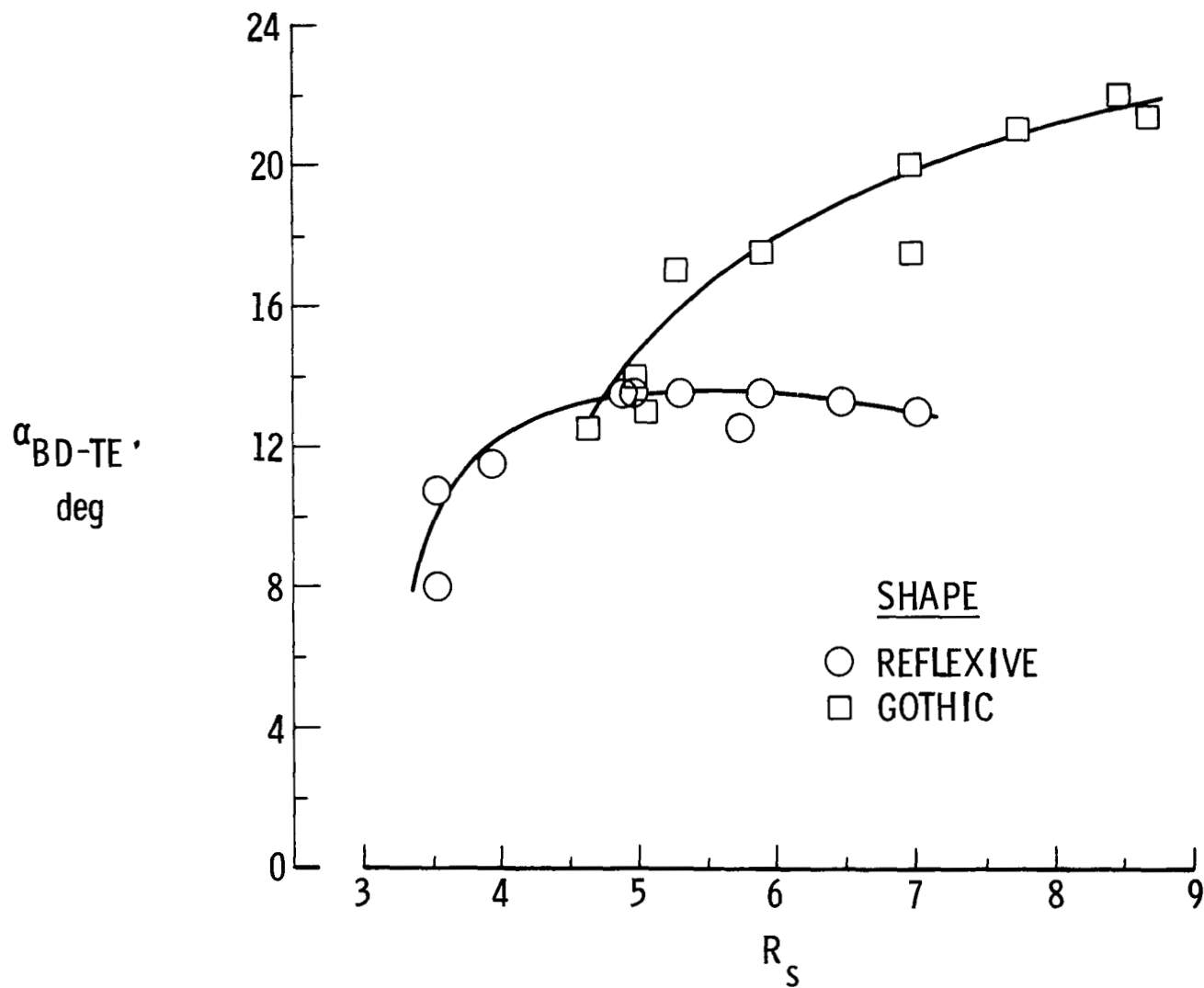
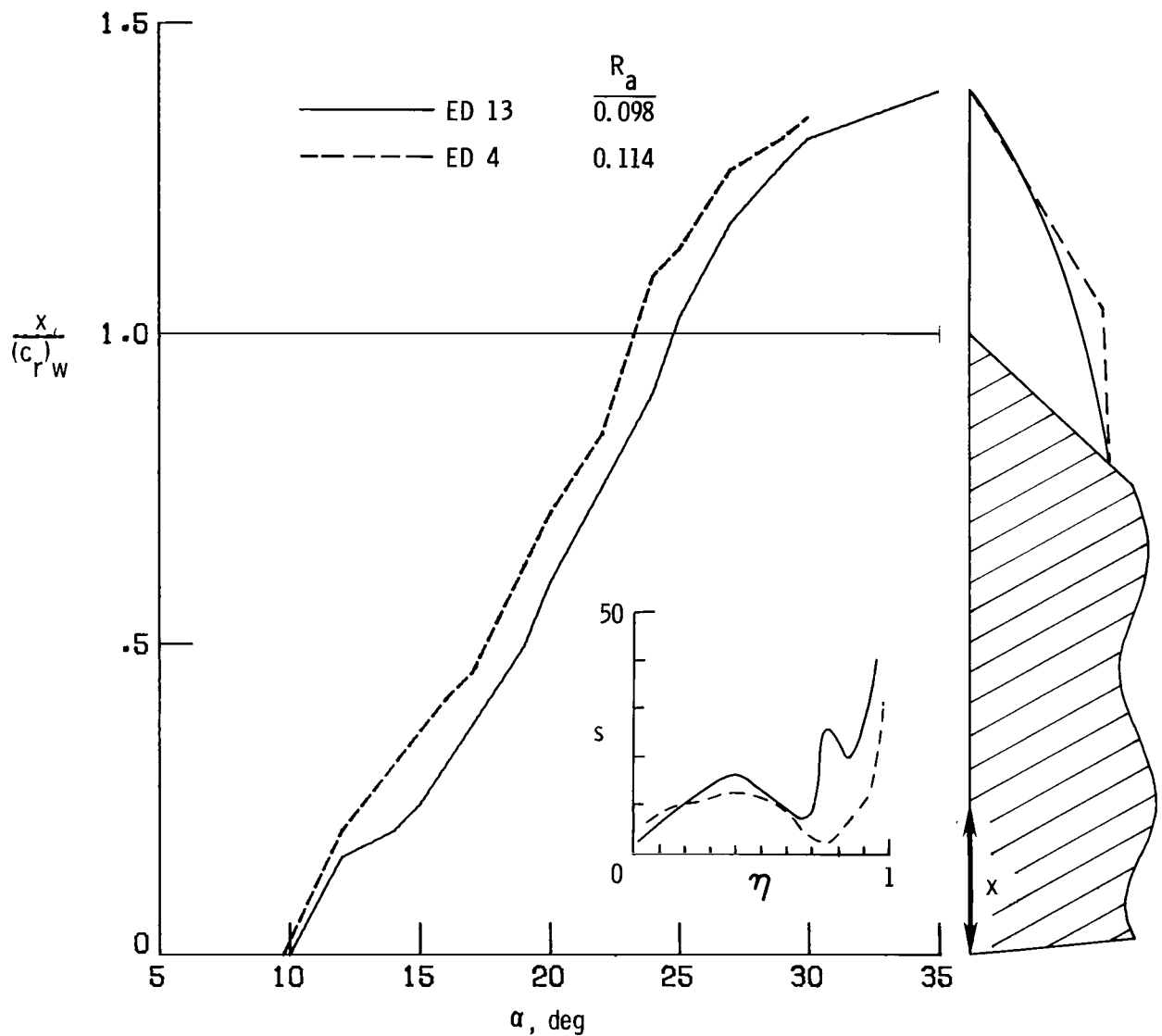
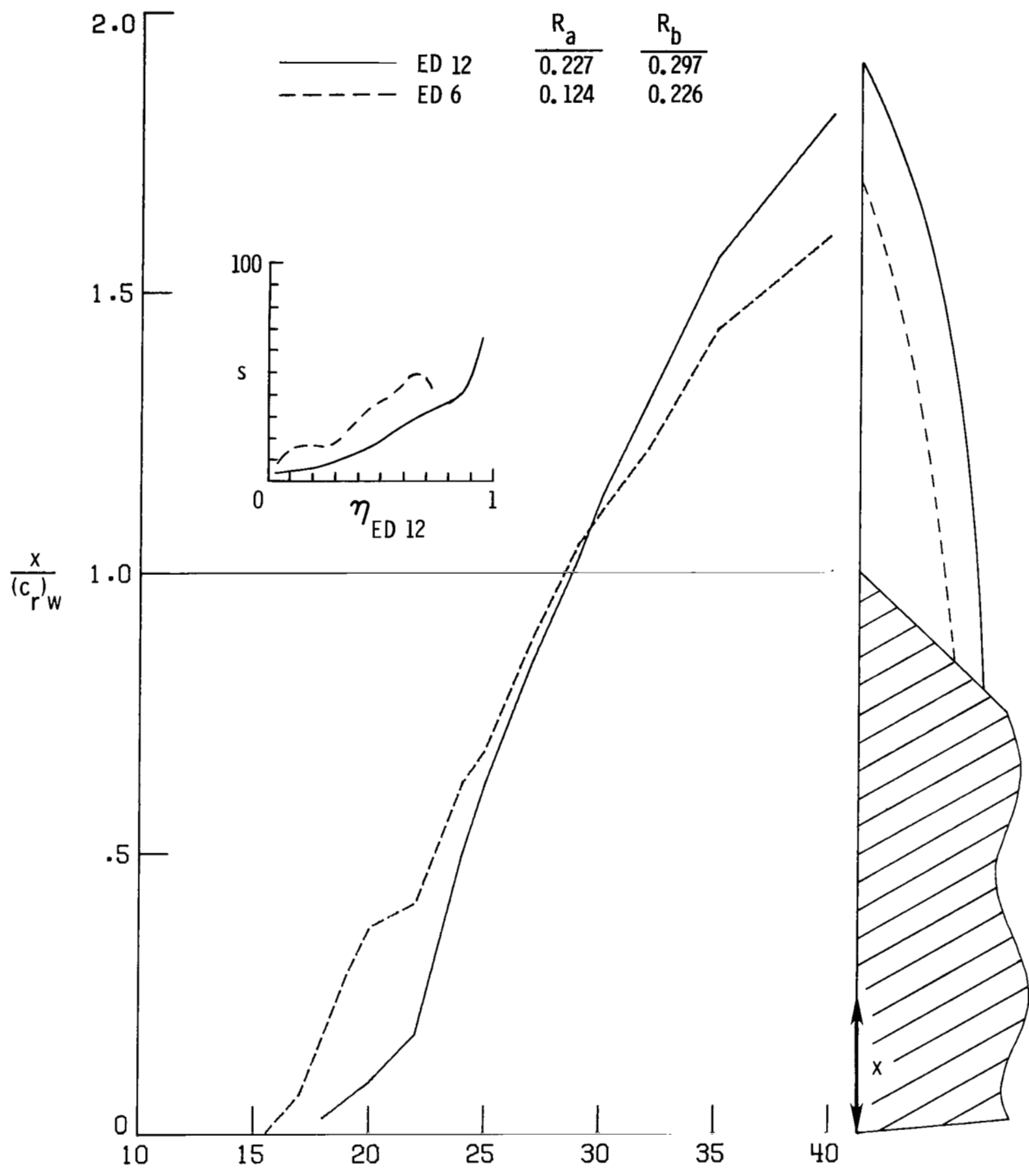


Figure 25.- Effect of strake shape on  $\alpha_{BD-TE}$  versus  $R_s$ .  $R_b = 0.212$ .



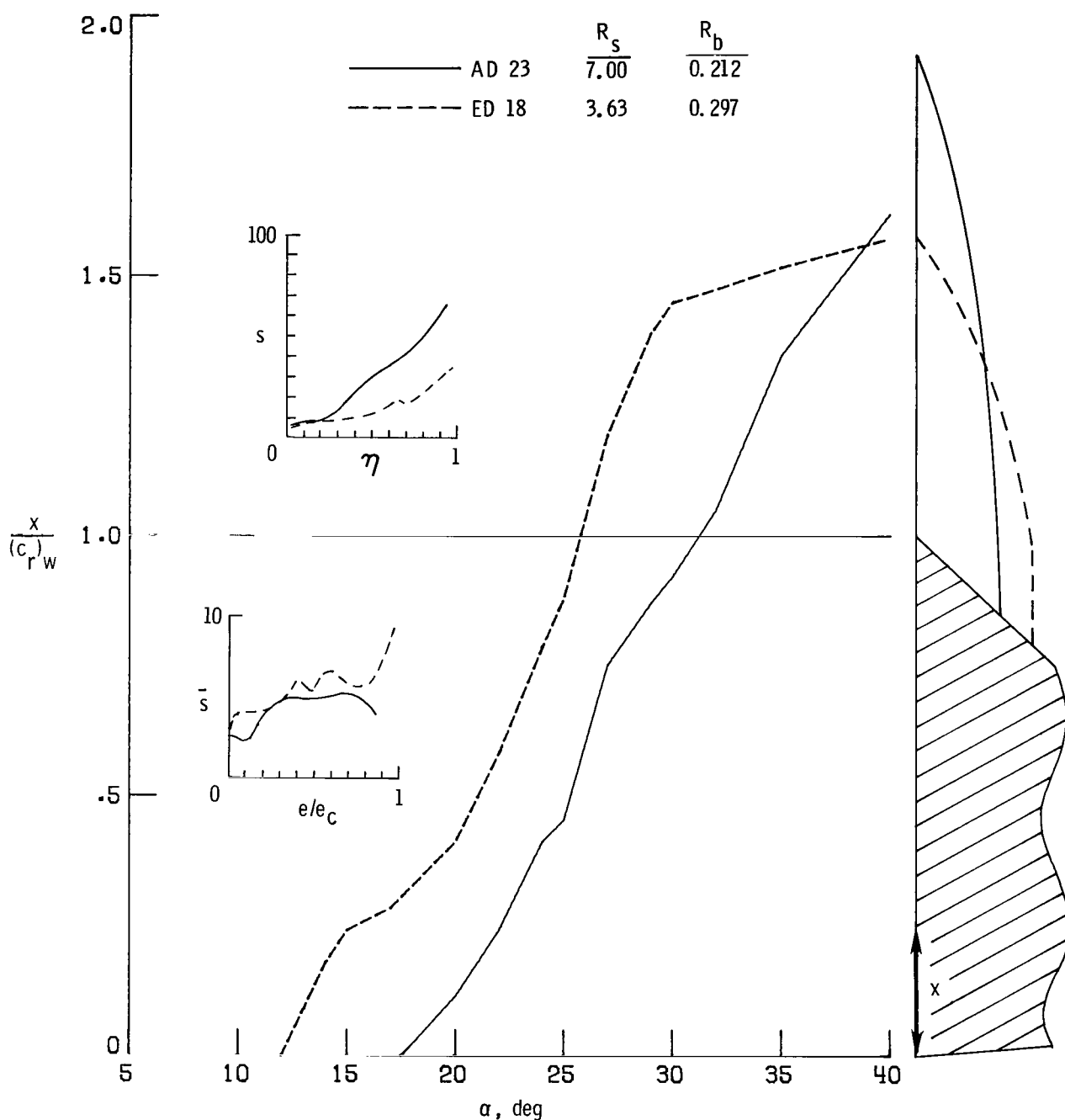
(a)  $R_s \approx 2.78$ .

Figure 26.- Effect of strake geometry on vortex breakdown and suction for fixed slenderness ratio.



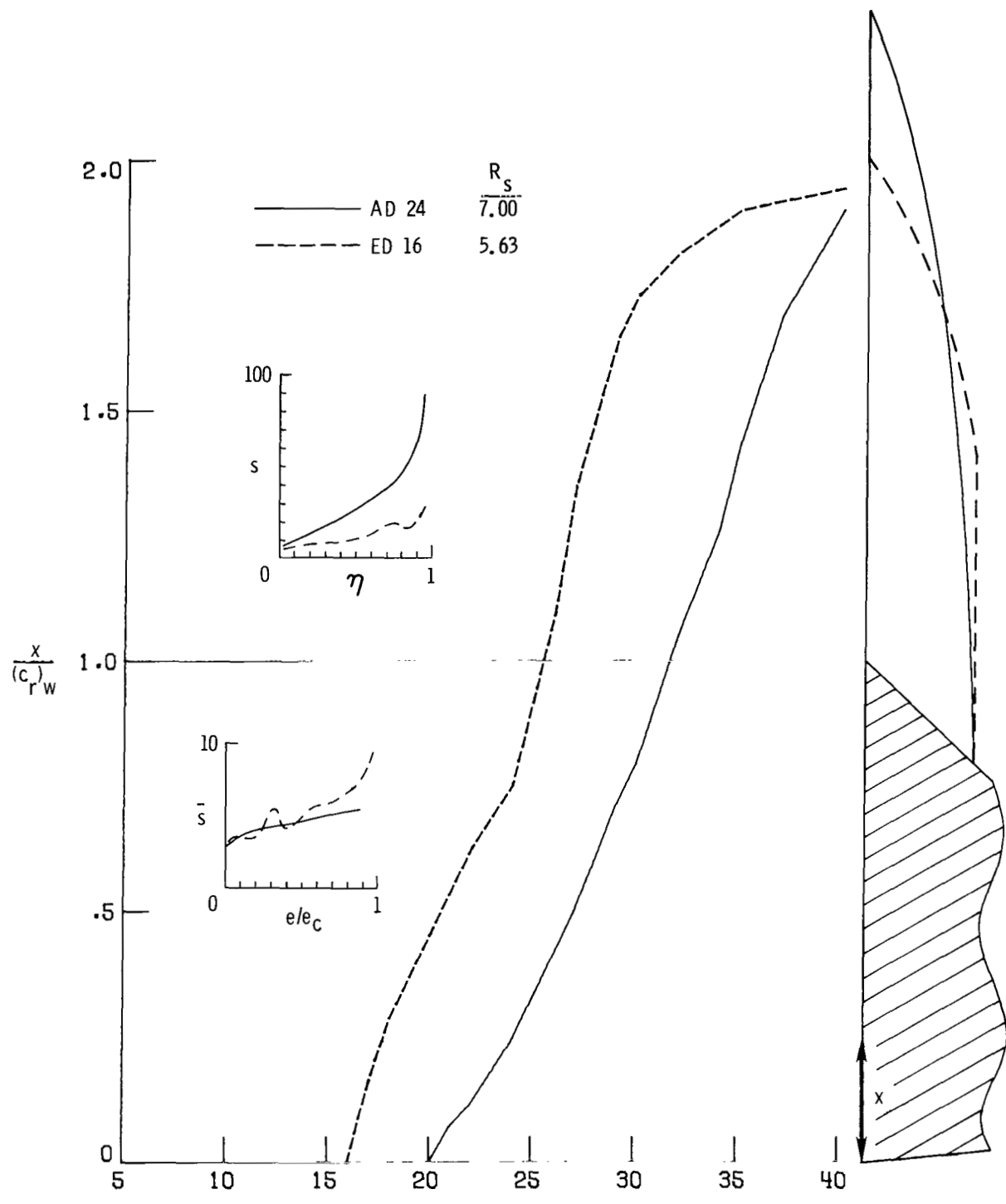
(b)  $R_s \approx 5.20.$

Figure 26.- Concluded.



(a)  $R_a = 0.166$ .

Figure 27.- Effect of strake geometry on vortex breakdown and suction for fixed area.



(b)  $R_a = 0.325$ .

Figure 27.- Concluded.

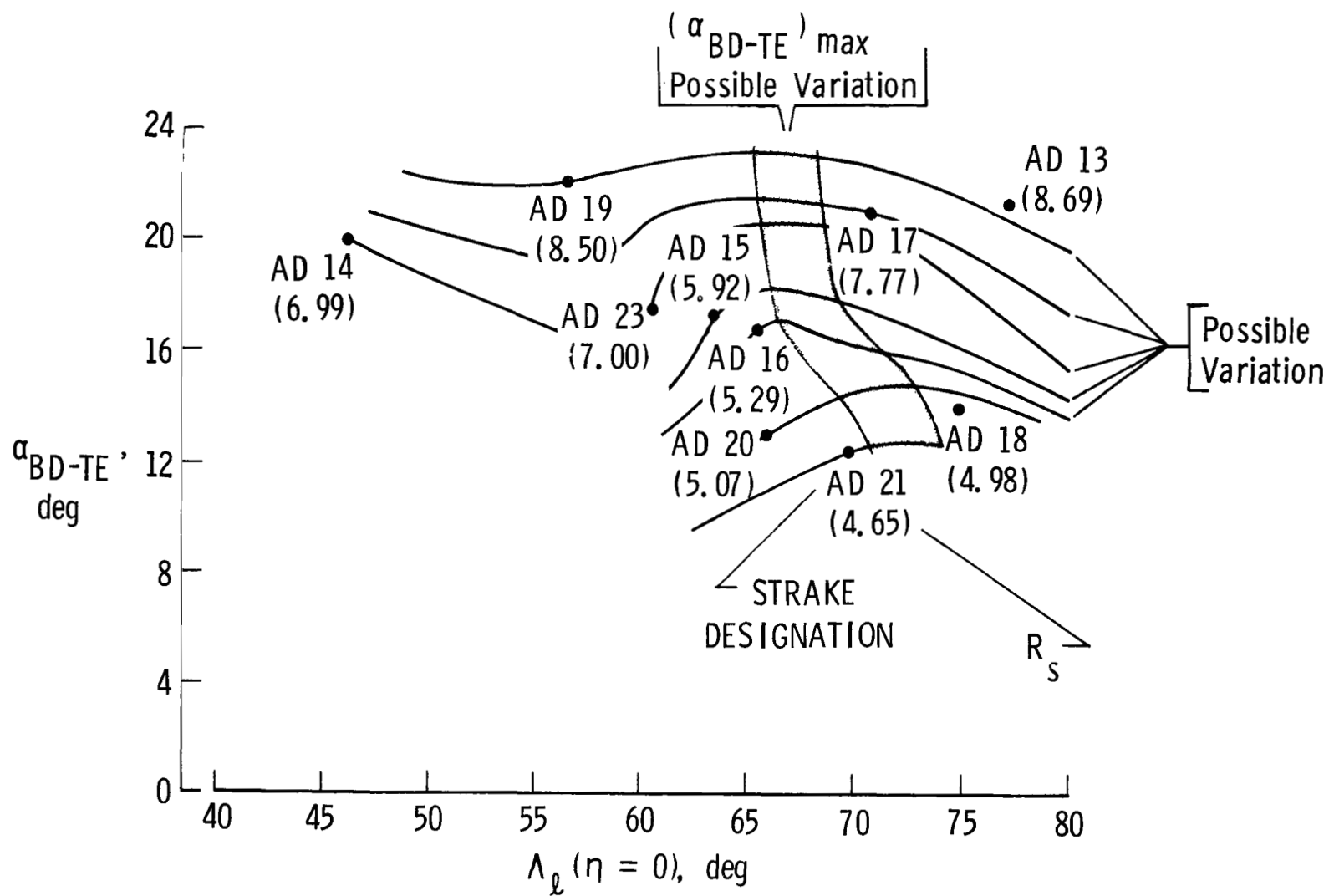


Figure 28.- Effect of  $R_s$  on  $\alpha_{BD-TE}$  versus  $\lambda_l(\eta=0)$  for gothic strakes.  $R_b = 0.212$ .

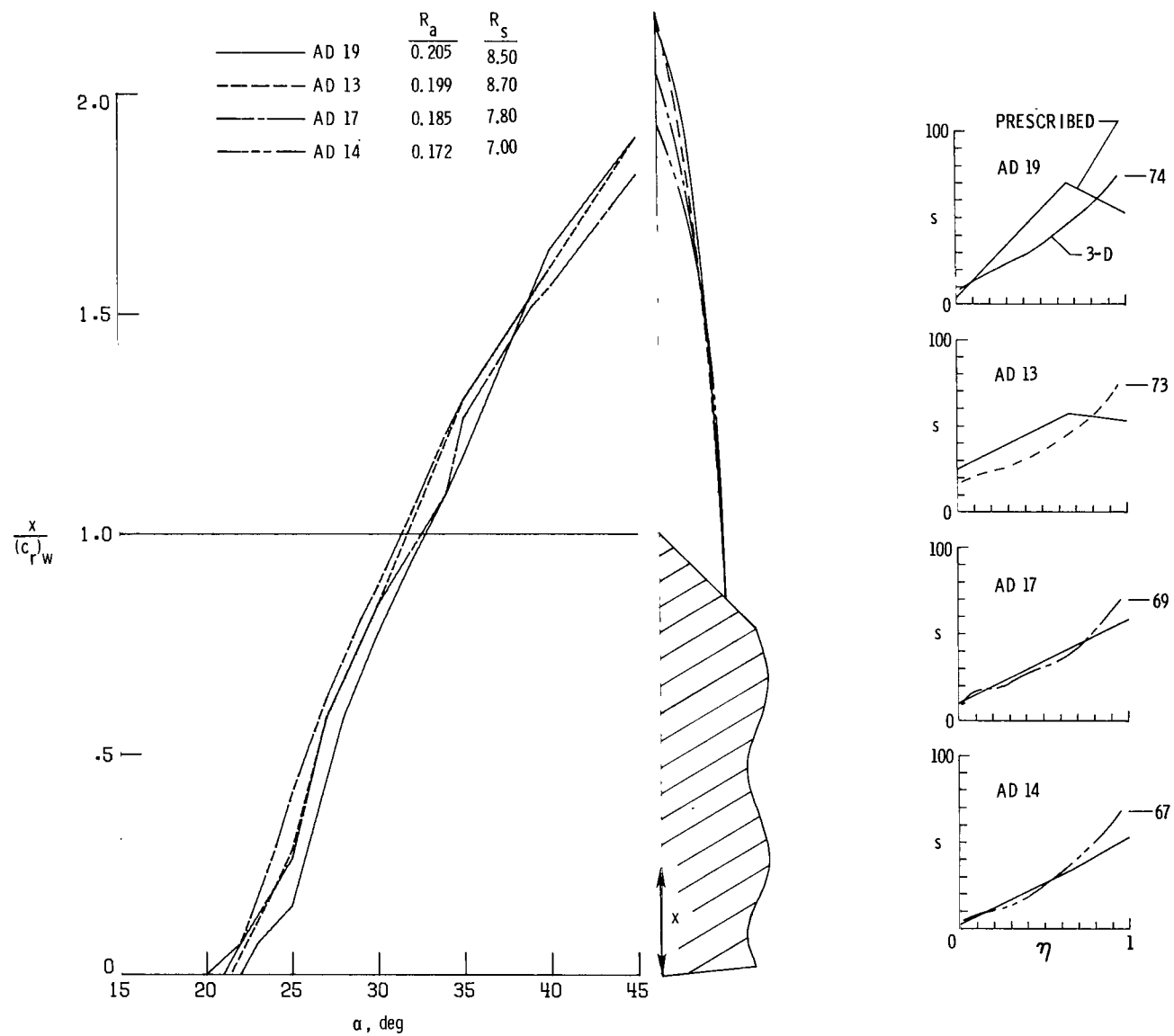


Figure 29.- Correlation of performance with suction.

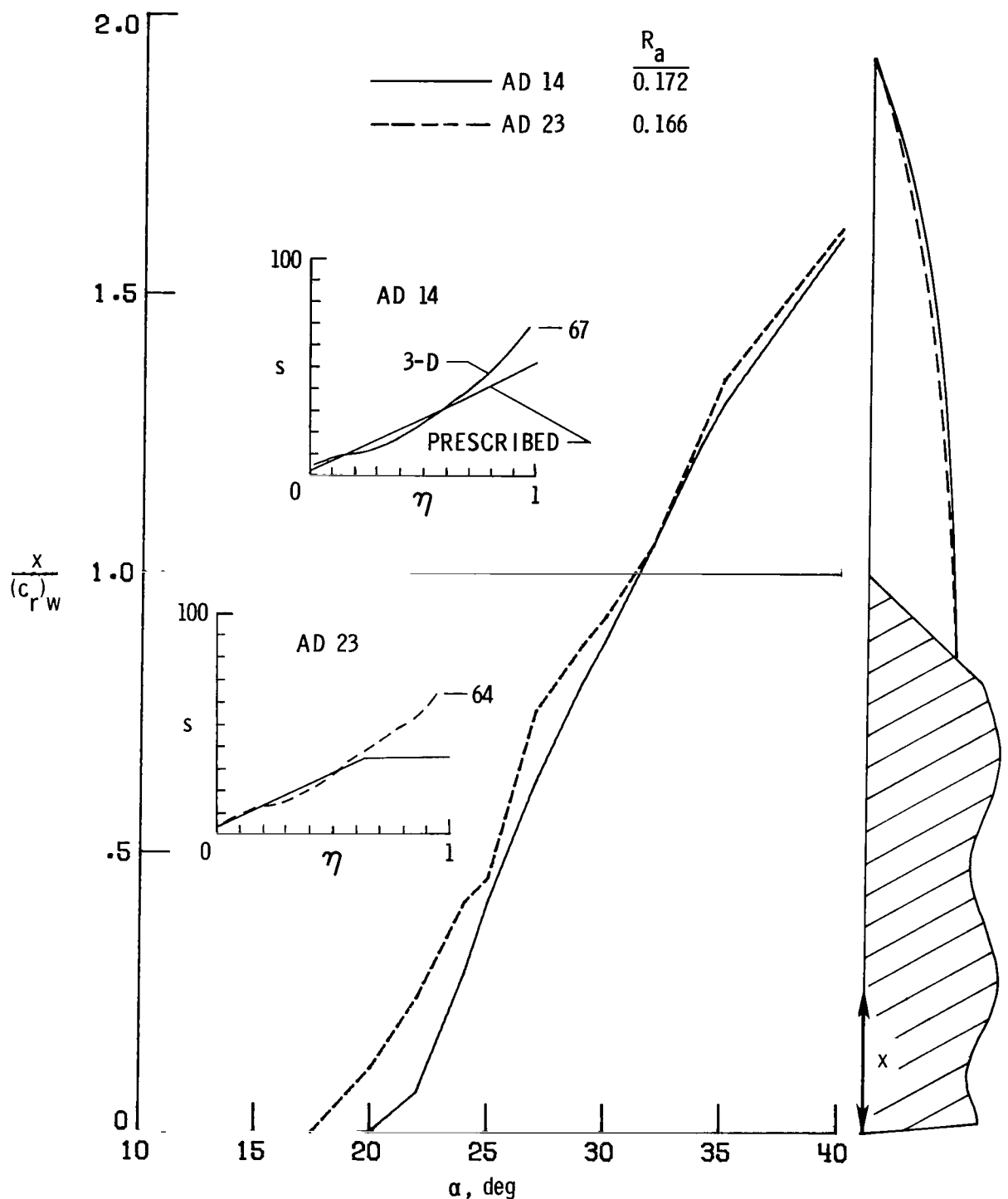


Figure 30.- Effect of small shape variation on vortex breakdown and suction.  
 $R_s = 7.00$ ;  $R_b = 0.212$ .

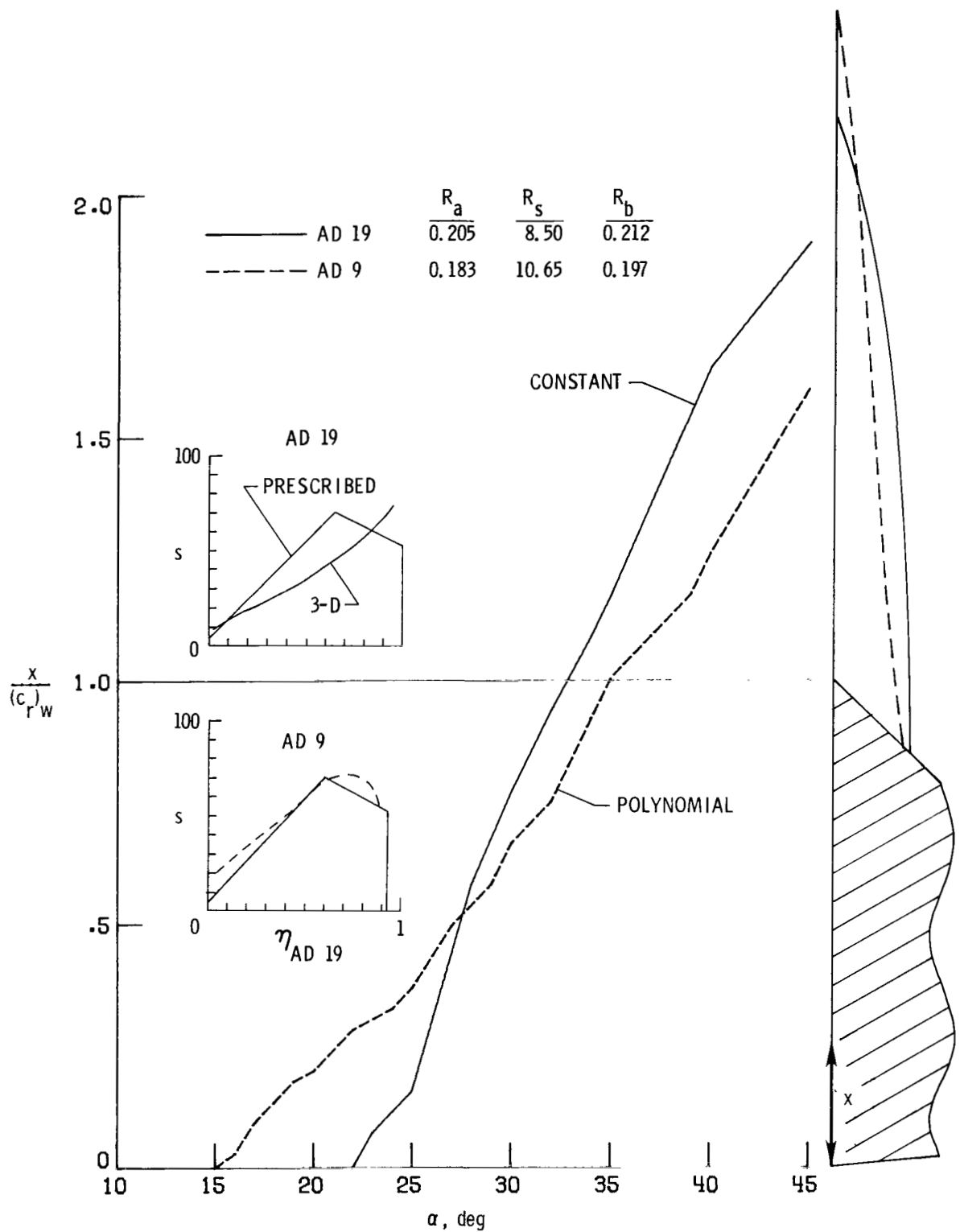
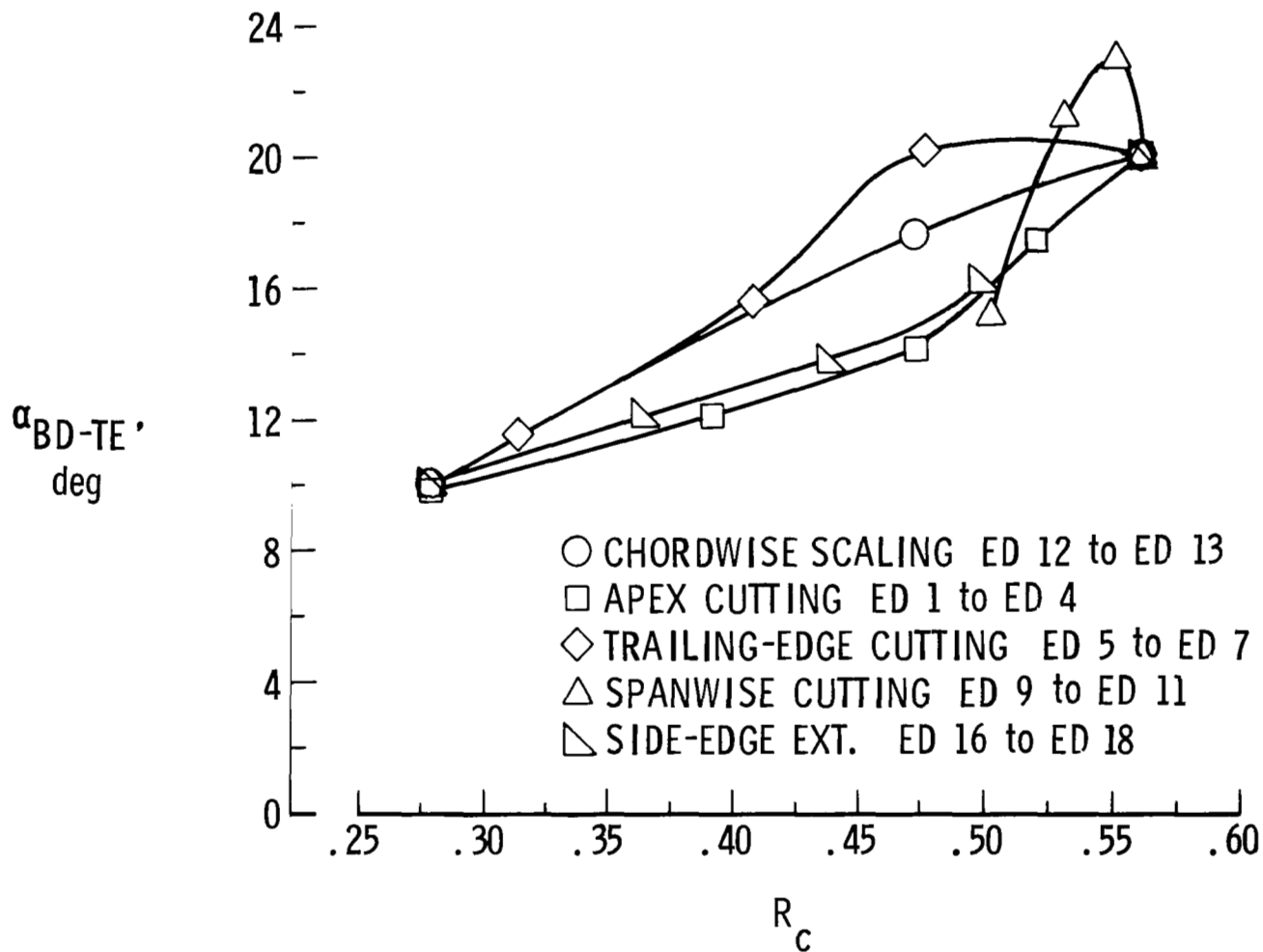
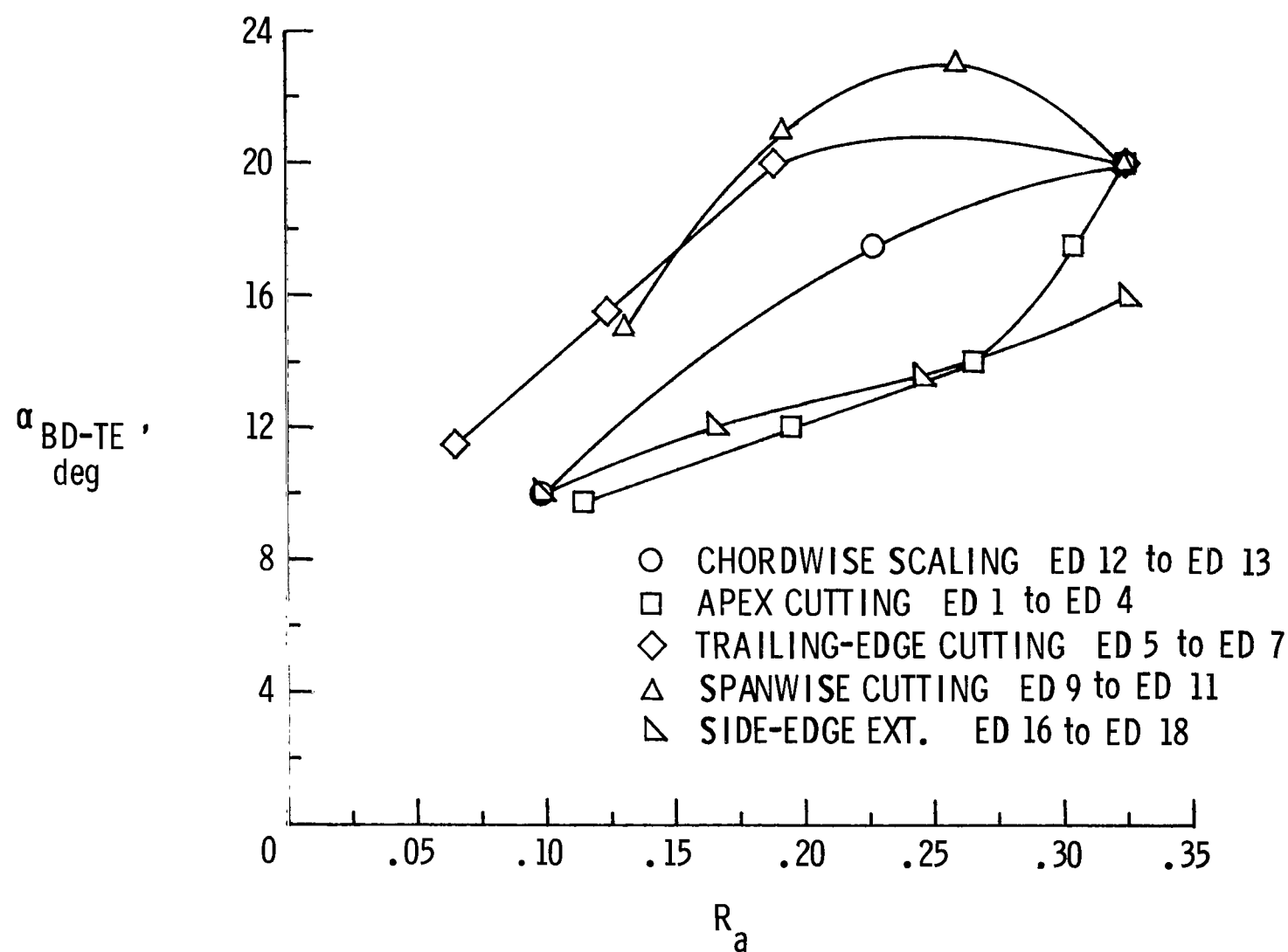


Figure 31.- Effect of pressure specification on vortex breakdown and suction.



(a) Variation in chord.

Figure 32.- Summary of trailing-edge breakdown angle for the various chord modification techniques.



(b) Variation in area.

Figure 32.- Concluded.

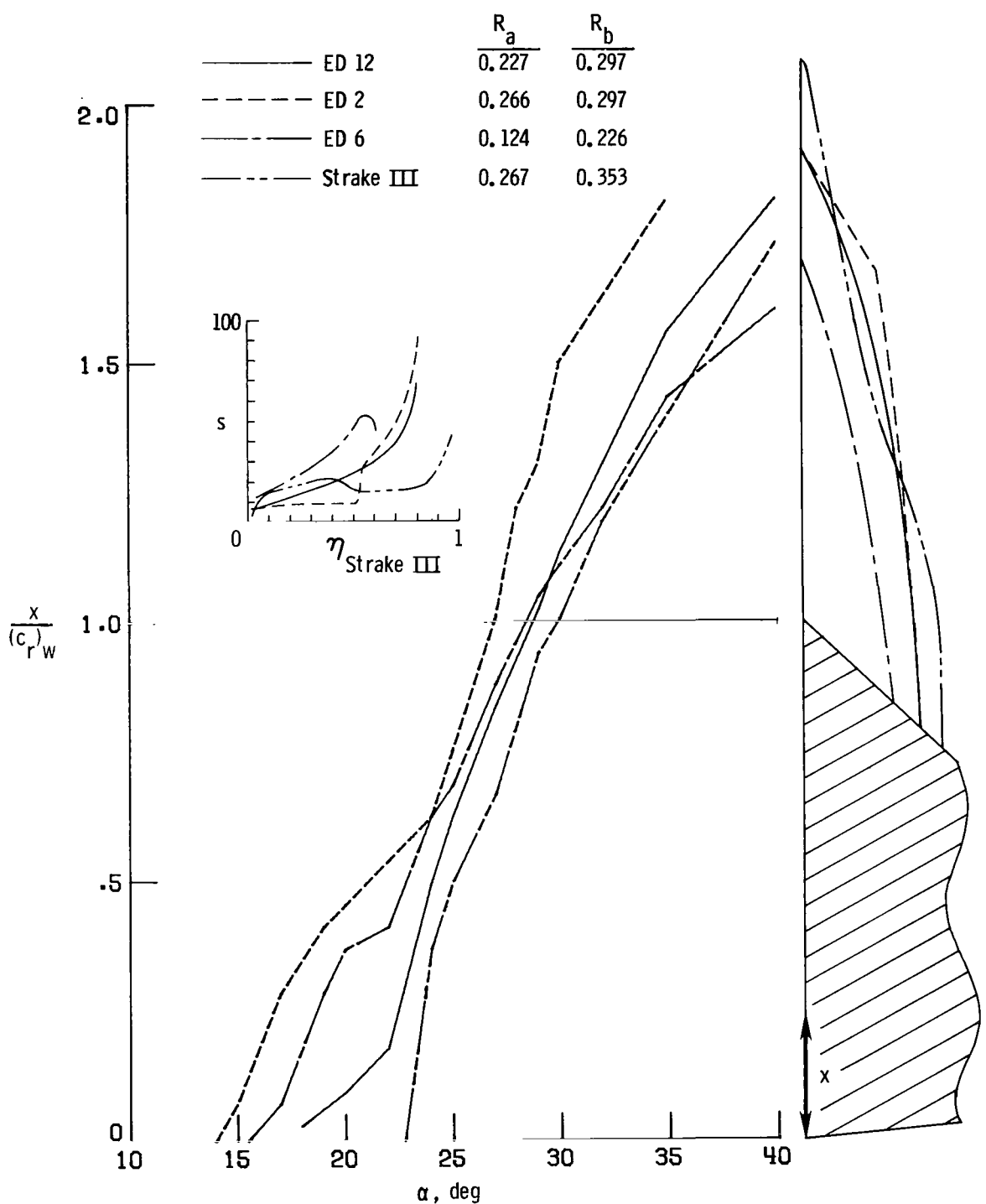


Figure 33.- Anomalies in the relationship between  $s_t$  and  $\alpha_{BD-TE}$  for strakes having  $R_s \approx 5.2$ .

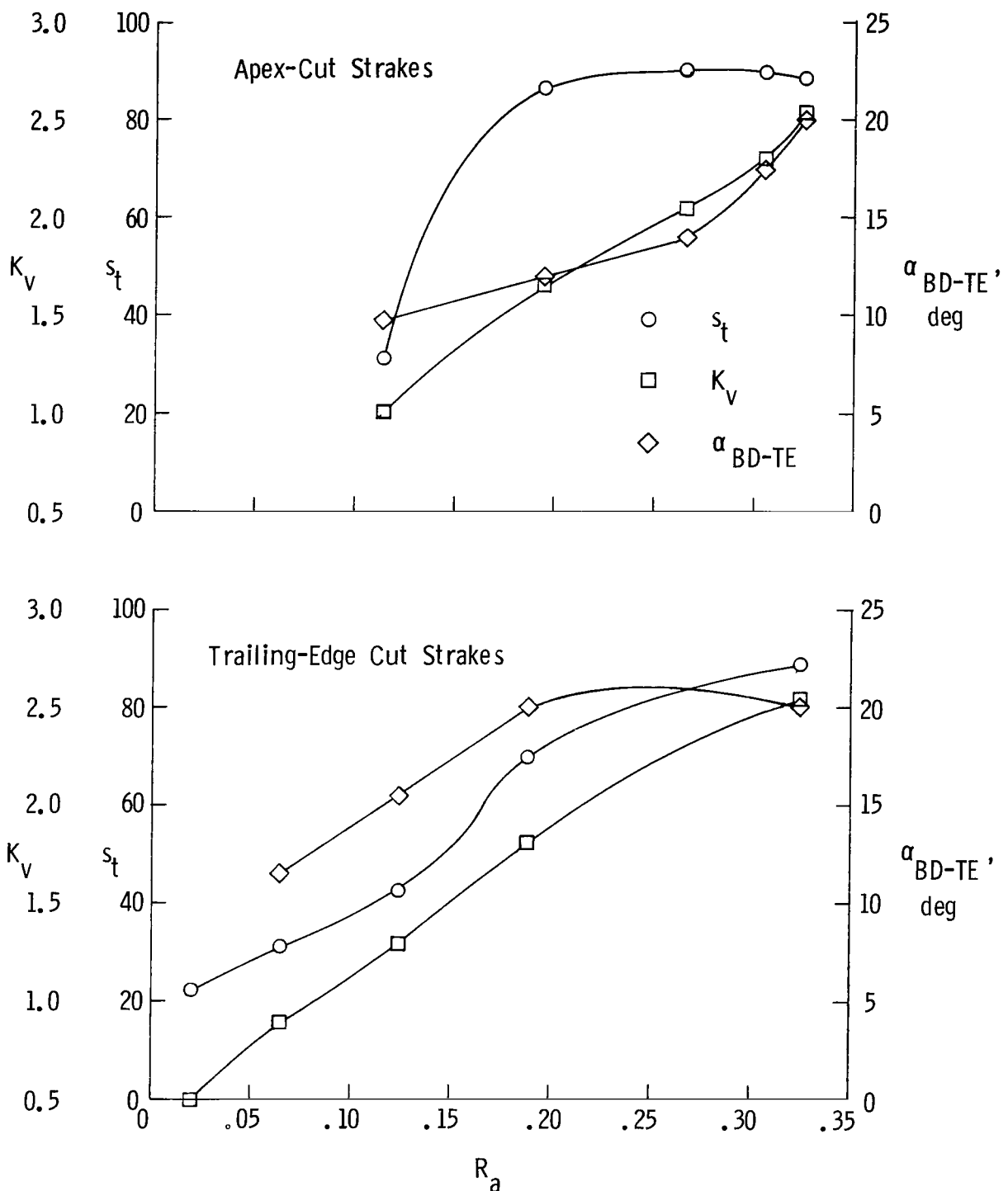


Figure 34.- Parameters associated with two chord modification techniques.

1. Report No. NASA TP-1676	2. Government Accession No.	3. Recipient's Catalog No.	
4. Title and Subtitle  WATER-TUNNEL AND ANALYTICAL INVESTIGATION OF THE EFFECT OF STRAKE DESIGN VARIABLES ON STRAKE VORTEX BREAKDOWN CHARACTERISTICS		5. Report Date August 1980	
7. Author(s)  Neal T. Frink and John E. Lamar		6. Performing Organization Code	
9. Performing Organization Name and Address  NASA Langley Research Center Hampton, VA 23665		8. Performing Organization Report No. L-13254	
12. Sponsoring Agency Name and Address  National Aeronautics and Space Administration Washington, DC 20546		10. Work Unit No. 505-06-53-01	
15. Supplementary Notes		11. Contract or Grant No.	
16. Abstract  A systematic water-tunnel study was made to determine the vortex breakdown characteristics of 43 strakes, more than half of which were generated from a new analytical strake design method. The strakes were mounted on a 1/2-scale model of a Langley Research Center general research fighter fuselage model with a 44° leading-edge-sweep trapezoidal wing. The analytically designed strake shapes provided examples of the effects of the primary design parameters (size, span, and slenderness) on vortex breakdown characteristics. These effects were analyzed in relation to the respective strake leading-edge suction distributions. Included are examples of the effects of detailed strake planform shaping. It was concluded that, consistent with the design criterion, those strakes with leading-edge suction distributions which increase more rapidly near, and have a higher value at, the spanwise tip of the strake produce a more stable vortex.		13. Type of Report and Period Covered Technical Paper	
17. Key Words (Suggested by Author(s))  Strake Water tunnel Vortex breakdown Leading-edge suction distribution Analytical design		18. Distribution Statement  Unclassified - Unlimited  Subject Category 02	
19. Security Classif. (of this report) Unclassified	20. Security Classif. (of this page) Unclassified	21. No. of Pages 90	22. Price A04

National Aeronautics and  
Space Administration

Washington, D.C.  
20546

Official Business  
Penalty for Private Use, \$300

THIRD-CLASS BULK RATE

Postage and Fees Paid  
National Aeronautics and  
Space Administration  
NASA-451



1 1 1U,A, 071180 S00903DS  
DEPT OF THE AIR FORCE  
AF WEAPONS LABORATORY  
ATTN: TECHNICAL LIBRARY (SUL)  
KIRTLAND AFB NM 87117

NASA

POSTMASTER: If Undeliverable (Section 158  
Postal Manual) Do Not Return

---